RECTANGULAR WAVEGUIDE MODE CONVERTERS FOR CREATING MONOPULSE RADIATION PATTERNS

A THESIS SUBMITTED TO
THE GRADUATE SCHOOL OF NATURAL AND APPLIED SCIENCES
OF
MIDDLE EAST TECHNICAL UNIVERSITY

BY

ONURHAN DUMAN

IN PARTIAL FULFILLMENT OF THE REQUIREMENTS
FOR
THE DEGREE OF MASTER OF SCIENCE
IN
ELECTRICAL AND ELECTRONICS ENGINEERING

MARCH 2018

Approval of the thesis:

RECTANGULAR WAVEGUIDE MODE CONVERTERS FOR CREATING MONOPULSE RADIATION PATTERNS

submitted by **ONURHAN DUMAN** in partial fulfillment of the requirements for the degree of **Master Science in Electrical and Electronics Engineering Department, Middle East Technical University** by,

Prof. Dr. Halil Kalıpçılar
Dean, Graduate School of **Natural and Applied Sciences** ____________

Prof. Dr. Tolga Çiloğlu
Head of Department, **Electrical and Electronics Engineering** ____________

Prof. Dr. Gülbin Dural Ünver
Supervisor, **Electrical and Electronics Eng. Dept., METU** ____________

Examining Committee Members:

Prof. Dr. Sencer Koç
Electrical and Electronics Eng. Dept, METU ____________

Prof. Dr. Gülbin Dural Ünver
Electrical and Electronics Eng. Dept, METU ____________

Prof. Dr. Şimşek Demir
Electrical and Electronics Eng. Dept, METU ____________

Prof. Dr. Özlem Aydın Çivi
Electrical and Electronics Eng. Dept, METU ____________

Prof. Dr. Birsen Saka
Electrical and Electronics Eng. Dept., Hacettepe University ____________

Date: **12/03/2018**

I hereby declare that all information in this document has been obtained and presented in accordance with academic rules and ethical conduct. I also declare that, as required by these rules and conduct, I have fully cited and referenced all material and results that are not original to this work.

Name, Last Name: ONURHAN DUMAN

Signature :

ABSTRACT

RECTANGULAR WAVEGUIDE MODE CONVERTERS FOR CREATING MONOPULSE RADIATION PATTERNS

Duman, Onurhan

M.S., Department of Electrical and Electronics Engineering

Supervisor : Prof. Dr. Gülbin Dural Ünver

March 2018, 152 pages

For waveguide structures, there is an alternative way of creating three monopulse radiation patterns by using mode converters and radiating different waveguide modes (not only TE_{10} mode) for creating different monopulse radiation patterns. In the literature, different radiating modes are offered depending on waveguide shape. For rectangular waveguide, one suggestion is to radiate TE_{10} mode for the creation of sum channel radiation pattern, to radiate TE_{20} mode for the creation of azimuth difference radiation pattern and to radiate the combination of TE_{11} and TM_{11} modes for the creation of elevation difference radiation pattern. In our work, three different rectangular waveguide mode conversion techniques (discrete stepped mode converter, bend mode converter, corner mode converter) are investigated for converting fundamental TE_{10} mode to these required modes. For each mode conversion technique, all fundamental mode converters are designed. One of these designed mode converters is manufactured by using 3D printer and it is painted with conductive silver paint to make it conductive. Obtained radiation pattern and S parameter measurement results indicates that design and manufacturing techniques used in this thesis produce good results since these measurement results are in very good agreement with simulation results.

Keywords: Rectangular Waveguides, Monopulse Radar, Monopulse Radiation Patterns, Mode Converters, 3D Printer Manufacture

ÖZ

TEK DARBE IŞIMA ÖRÜNTÜLERİ YARATMAK İÇİN DİKDÖRTGEN DALGA KILAVUZU MOD ÇEVİRİCİLER

Duman, Onurhan

Yüksek Lisans, Elektrik ve Elektronik Mühendisliği Bölümü

Tez Yöneticisi : Prof. Dr. Gülbin Dural Ünver

Mart 2018, 152 sayfa

Dalga kılavuzu altyapısına sahip tek darbe radarları için 3 tek darbe ışıma örüntüsünü oluşturmak alternatif bir yöntem mevcuttur. Bu yöntemde mod çeviriciler kullanılmakta ve temel mod olan TE_{10} modu dışında başka modları da yayın yaparak bu üç tek darbe kanalı ışıma örüntüleri yaratılmaktadır. Literatürde dalga kılavuzu yapısına bağlı olarak farklı modlar yayın yapması için önerilmiştir. Dikdörtgen dalga altyapısı için, yapılan önerilerden biri toplam kanalı ışıma örüntüsünü yaratmak için TE_{10} modunun yayın yapılması, yanca fark kanalı ışıma örüntüsünü yaratmak için TE_{20} modunun yayın yapılması ve yükseliş fark kanalı ışıma örüntüsünü yaratmak için TE_{11} ve TM_{11} mod kombinasyonunun yayın yapılmasıdır. Bizim çalışmamızda, temel mod olan TE_{10} modunu bu modlara çevirmek için üç farklı dikdörtgen dalga kılavuzu mod çevirme tekniği (kesintili adımlı mod çevirici, bükülmüş mod çevirici, köşe mod çevirici) incelenmiştir. Her mod çevirme tekniği için, tüm gerekli mod çeviriciler tasarlanmıştır. Tasarlanan mod çeviricilerden biri 3 boyutlu yazıcı kullanılarak üretilmiş, daha sonra iletken olması için iletken gümüş boya ile boyanmıştır. Elde edilen ışıma örüntüsü ve S parametresi ölçüm sonuçları analiz sonuçlarıyla çok benzer olduğundan bu tezde kullanılan tasarım ve üretim tekniğini doğrulamıştır.

Anahtar Kelimeler: Dikdörtgen Dalga Kılavuzu, Tek Darbe Radarı, Tek Darbe Radarı Işıma Örüntüleri, 3 Boyutlu Yazıcı Üretimi

To my dearest family

ACKNOWLEDGMENTS

First of all, I would like to thank my thesis advisor Prof. Dr. Gülbin Dural Ünver for her help, comments, remarks and guidance. None of this would have been possible without her.

I would like to thank Alper Ünal, Mehmet Altuntaş, Süleyman Melikşah Yayan for their guidance, inspiring ideas at the beginning of this thesis, and for their review at the end of this thesis.

I would like to thank Ahmet Burak Aktaş for making 3D printer fabrication for one of the designs given in this thesis. Without him, I could not manufacture my design.

I am also grateful to my family and İdil Arıker, love of my life, for their endless support and encouragement throughout my life and during the writing process of this thesis.

I would like to thank all my friends for their understanding and support during this thesis.

Finally, I would like to acknowledge the support of ASELSAN Inc. during this thesis.

TABLE OF CONTENTS

LIST OF TABLES

TABLES

LIST OF FIGURES

FIGURES

CHAPTER 1

INTRODUCTION

Monopulse radars are one of the most popular tracking radars which have been used since 1940s, [1]- [2]. In the older conventional conical scanning radars, radar antenna is rotated in the region of interest (conical scan region). The target is estimated by the position of the largest echo [3]. Before monopulse radars, there were other signal channel scanning techniques other than conical scanning radars, namely linear (planar) scanning and sequential switch beams [4]. Their target finding method was similar to the target finding method of conical scan radars. Processing time for a single channel scanning radar takes longer time as compared to a monopulse radar and the resolution of single channel scanning radar is not very good in comparison either. On the other hand, monopulse radars are multi-channel radars. Its name comes its working principle. From only single pulse, target location is learned by comparing the signals received from two or more simultaneous antenna beam channels [5]. They are superior to single channel scanning radars in terms of accuracy of target location estimation [5].

Although there are several types of monopulse radars, [2], [4], [5], in this thesis, amplitude sum-and difference monopulse radars (which is generally used) are considered. From now on this type of monopulse radars (and antennas) will be simply referred as monopulse radars (and antennas).

1.1. Conventional Monopulse Feeds and Typical Patterns

The conventional monopulse radars have two or three channels depending on the application. If all information about target (distance, velocity, angle in azimuth plane, angle in elevation plane) is required, three channel monopulse feeds are used. If one of the azimuth angle and elevation angle is unnecessary, two channel monopulse feeds are used.

The monopulse feeds consist of three main parts: Array of antennas which will be feed differently to create sum and difference radiation patterns, feeding network (usually called comparator) to feed these array elements, and the RF part for processing of the different channel signals. An example three channel feed system is shown in Figure 1.1 [6].

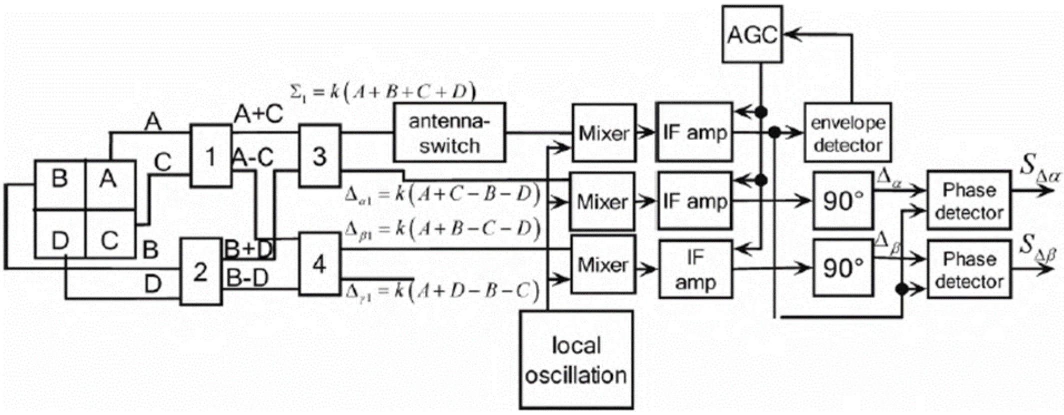

Figure 1.1: An example of 3 channel monopulse feed system [6]

In this thesis, we are interested in antenna array and comparator part of monopulse feeds. The rest of the system is out of scope of this thesis.

To create all three channel radiation patterns, at least a 2 by 2 antenna array is required. To create only two channel radiation patterns, at least a 2 by 1 antenna array is required. In order to understand how three monopulse radiation patterns are created, Figure 1.2 should be examined.

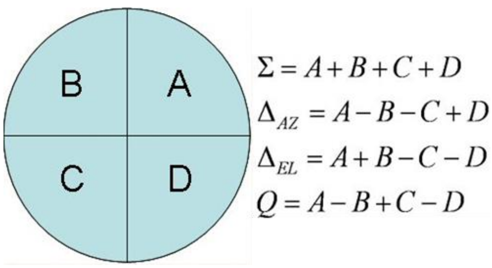

Figure 1.2: Three channel monopulse array and its feeding rules [7]

A, B, C and D are radiators (antenna elements). They can be horn antennas, planar elements or any other antenna. In this thesis, they are assumed to be horn antennas based on rectangular waveguides (or open-ended rectangular waveguides). To create sum channel radiation pattern, all four antenna elements must be fed by the same amplitude and phase. To create azimuth difference channel (sometimes it is also called delta azimuth) radiation pattern, A and D elements are fed by same amplitude and phase, B and C elements are fed by same amplitude and phase, A & D element pair and B & C element pair are fed by same amplitude but 180 degree phase difference. To create elevation difference channel (sometimes it is also called delta elevation) radiation pattern, A and B elements are fed by same amplitude and phase, C and D elements are fed by same amplitude and phase, A & B element pair and C & D element pair are fed by same amplitude but 180 degree phase difference. The Q channel shown in Figure 1.2 is usually not used.

In CST Microwave Studio® software, 2 by 2 horn antenna array based on rectangular waveguide is created and simulated at 10 GHz to illustrate three channel radiation patterns if the radiators are fed as mentioned above. Figure 1.3 shows 3D sum channel radiation pattern, Figure 1.4 shows 3D azimuth difference channel radiation pattern and Figure 1.5 shows 3D elevation difference radiation pattern of this CST model. Finally, Figure 1.6 shows 3D Q channel radiation pattern.

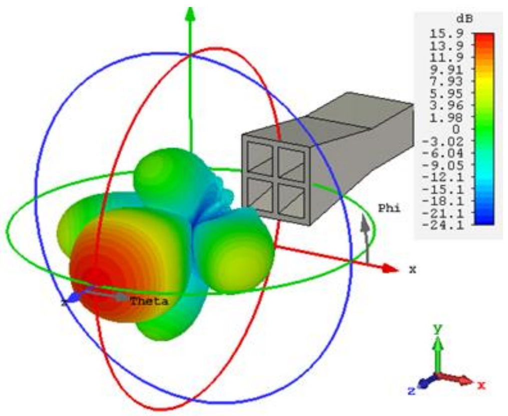

Figure 1.3: Typical 3D sum radiation pattern

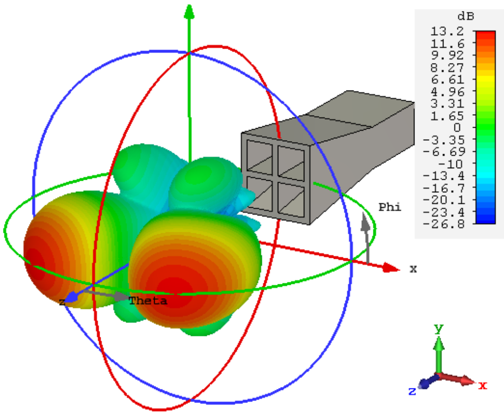

Figure 1.4: Typical 3D azimuth difference radiation pattern

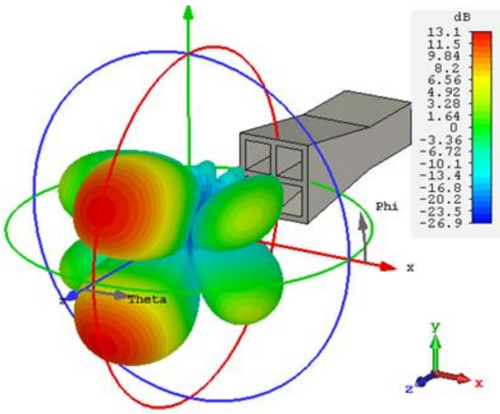

Figure 1.5: Typical 3D elevation difference radiation pattern

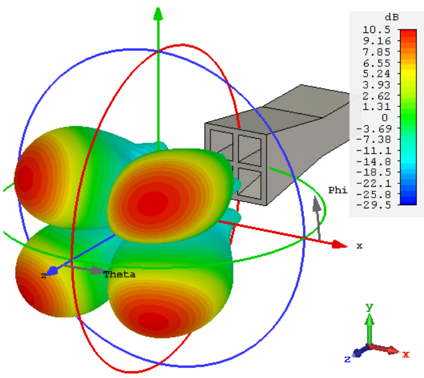

Figure 1.6: Typical 3D Q radiation pattern

Operating principle of monopulse radars is as follows: Assume that the angular position of the target is required. First, signal for the sum (∑) and signal for the delta azimuth ΔAz are obtained. Then these two signals are compared and the angle of target in azimuth plane is obtained (Figure 1.7). Similar procedure is done to obtain the angle of target in the elevation plane.

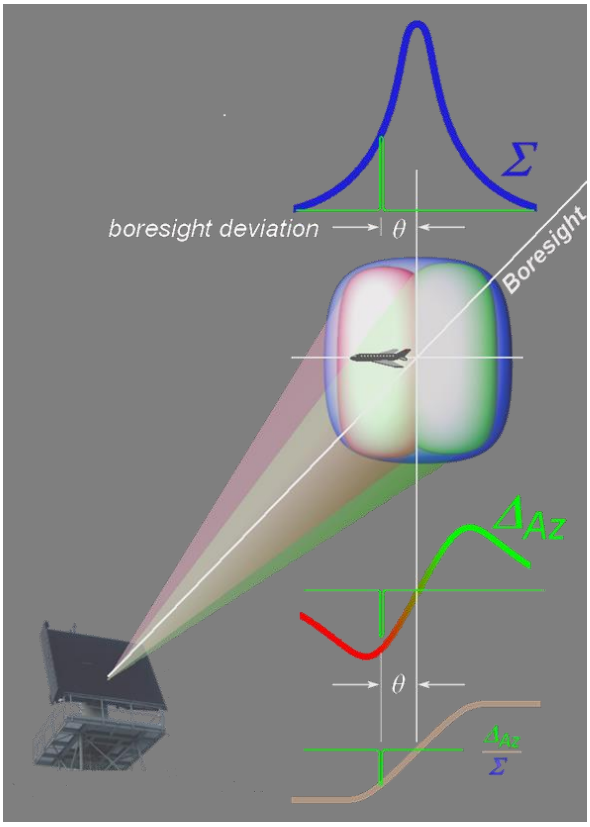

Figure 1.7: Operation principle of monopulse radar [8]

The operation of two channel monopulse antenna is similar to three channel monopulse antenna. It is preferred when the angular position of target in only one plane is sufficient (e.g. some naval radars which are designed to find other ships). For two channel monopulse antenna, using two radiators is enough (easier to design and implement than three channel). In the rest of this thesis, three channel monopulse antenna (or radar) will be simply referred to as monopulse antenna (or radar).

The feeding network (comparator):

The comparator of four antenna (2 by 2) monopulse feed is designed either by 180 degree coupler or 90 degree hybrid coupler. The general idea which is valid for both cases is shown in Figure 1.8.

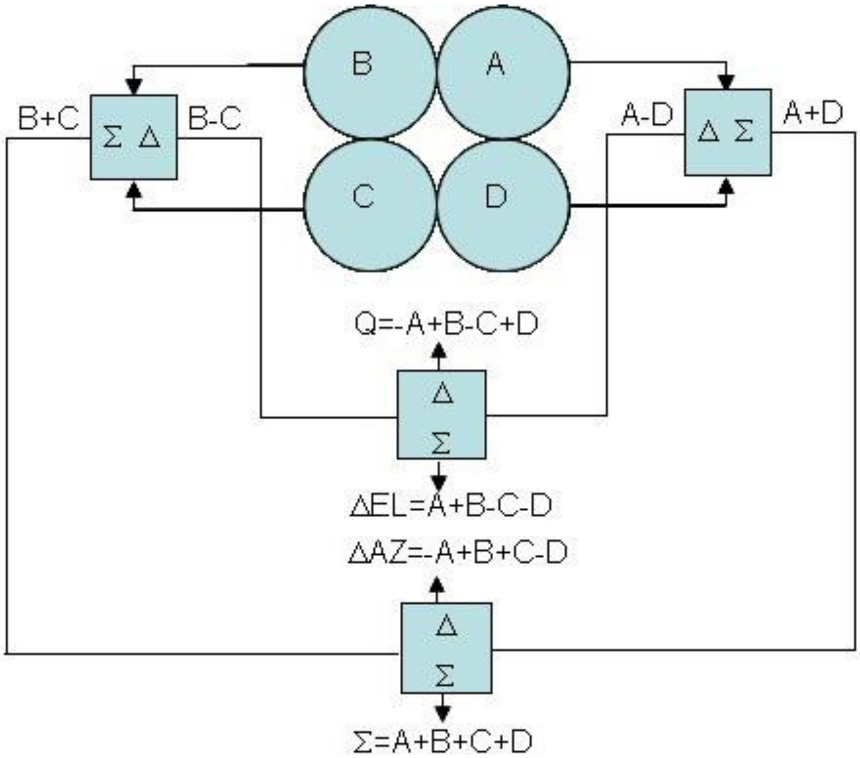

Figure 1.8: The general idea for designing comparators [9]

First method to design comparators is using 180 degree coupler (e.g. magic tee, rat race etc.). Figure 1.9 shows monopulse comparator design idea which uses magic-tees [10]. Figure 1.10 shows monopulse comparator design idea which uses rat-race couplers [7].

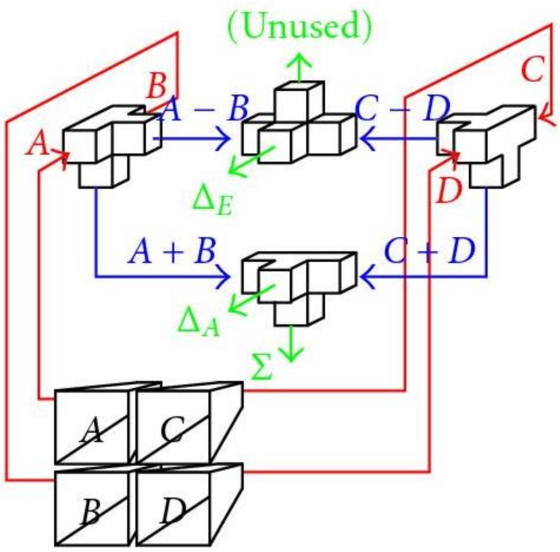

Figure 1.9: Idea for designing comparator by using magic-tees [10]

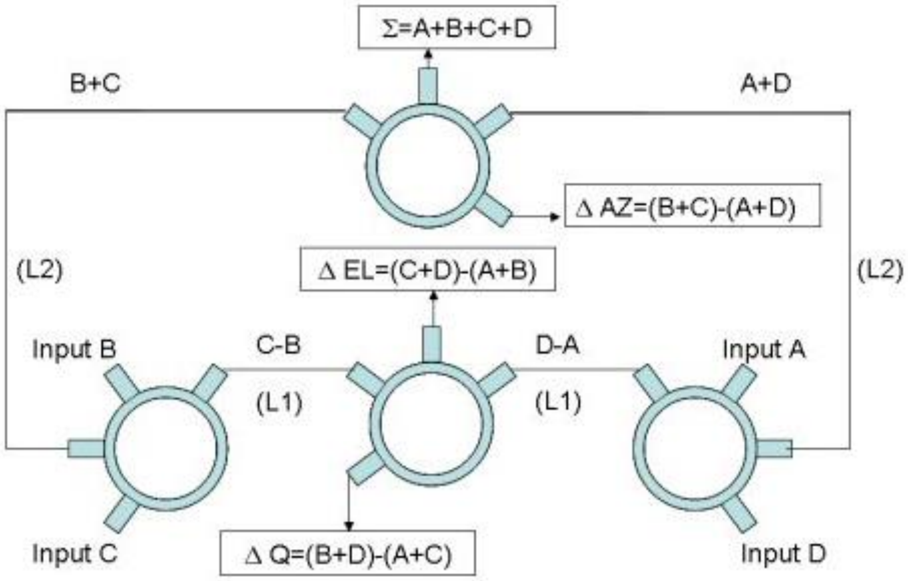

Figure 1.10: Idea for designing comparator by using rat race couplers [7]

Second method to design comparators is using 90 degree hybrid couplers. First, 90 degree section is added to one of the input of 90 degree hybrid coupler (to make 180 degree coupler), then idea shown Figure 1.11 is implemented [7].

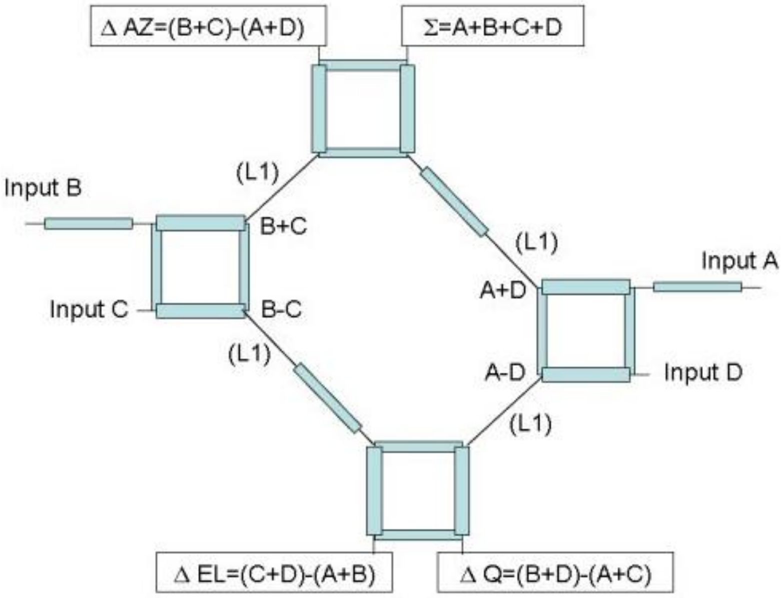

Figure 1.11: Idea for designing comparator by using 90 degree hybrid couplers [7]

As mentioned before, minimum 2 by 2 antenna array is required to generate all monopulse beams. For beam width optimization of different monopulse beams or for other applications (e.g. feeding of slotted waveguide array), more than four antennas can be used. More details about beam optimization of different monopulse beams are given in section 1.2. If more than four antennas are used to generate monopulse beams (sum, azimuth difference and elevation difference), comparator design becomes complex, but the general idea is the same. In such a case, A, B, C and D can be thought as subarrays or quadrants and above ideas for designing feeding networks can be applied. One example for this can be found in [11].

180 degree couplers and 90 degree hybrid couplers used in comparator designs can have different infrastructure based depending on different applications. They can be based on waveguides, planar structures etc. The antennas that are used as radiators can also be based on different infrastructures depending on different applications. They may be horn antennas based on waveguide structure, they may be planar patch antennas etc. Some examples for different radiator and comparator structures can be found in [12], [13], [14], [15], [16], [17], [18], [19], [20], [21], [22], [23], [24].

In this thesis, rectangular waveguide-based comparators and horn antennas are highly important. Please note that if the conventional monopulse feeds are using rectangular waveguide infrastructure, only waveguide mode that antennas radiate for all monopulse channels is the dominant TE_{10} mode.

1.2. Beam Width Optimization Problem in Conventional Monopulse Antennas

Beam width optimization problem arises when four horn array (2 by 2) conventional monopulse feed given in section 1.1 is used as feed of the focusing (reflector or lens) antenna system (for example, the feed given in Figure 1.3 is wanted to be used as feed antenna of parabolic reflector antenna).

Assuming the feed of reflector system only creates one type of radiation pattern (similar to radiation pattern in Figure 1.3), curvature of reflector is designed in such a way that -10 dB point (for normalized feed pattern) of the main lobe of the feed correspond to edges of reflector. This is usually the optimum trade off point between the illumination and spill over losses. If the main lobe value of normalized feed pattern at the edges is further reduced (assume that -15 dB), spill over losses decrease (as a result sidelobe level decreases) but illumination losses increase (antenna becomes inefficient, the gain of reflector system is reduced). If the main lobe value of normalized feed pattern at the edges is increased (assume that -7 dB), illumination losses decreases but spill over losses increase (most of the energy radiated by feed is not reflected by reflector surface, as a result sidelobe level increases and gain decreases) [25]. Figure 1.12 shows the visualization of illumination and spill over losses for different main lobe taper values [26].

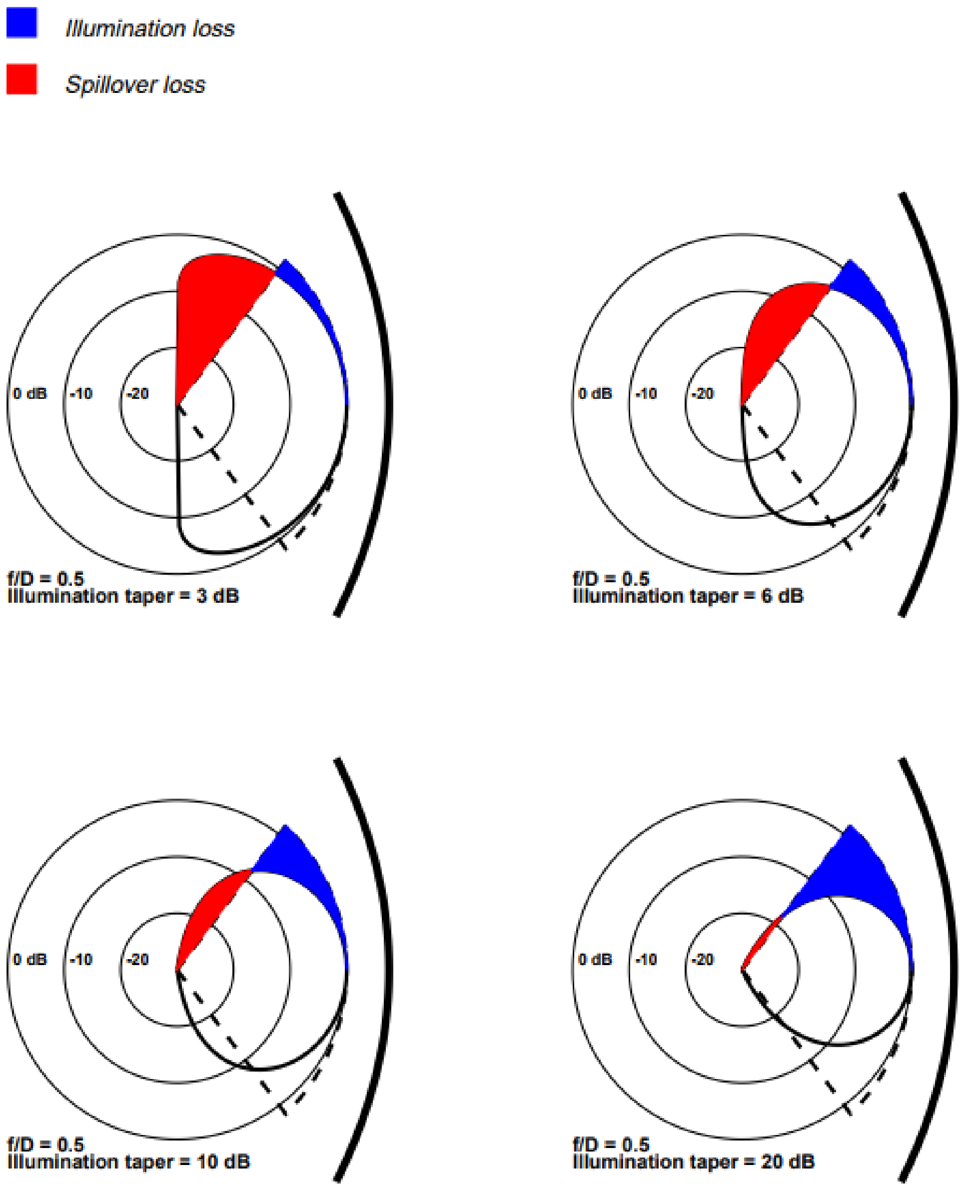

Figure 1.12: The visualization of illumination and spill over losses for different main lobe taper values [26]

Assuming the monopulse feed given in Figure 1.3, Figure 1.4 and Figure 1.5, this feed radiates 3 different patterns (sum, azimuth difference and elevation difference). If the beams in Figure 1.3 and Figure 1.4 are compared, it can be seen that in azimuth plane, beam width of azimuth difference pattern is almost two times of sum pattern in that plane, and in elevation plane, beam widths are almost same. Similarly, if the beams in

Figure 1.3 and Figure 1.5 are compared, it can be seen that in elevation plane, beam width of elevation difference pattern is almost two times of sum pattern in that plane, and in azimuth plane, beam widths are almost same. The reason for this, all three radiation patterns are radiated from same physical aperture. In Figure 1.13, the 2D normalized radiation pattern of the azimuth difference channel is shown on top of 2D normalized radiation pattern of the sum channel for the antenna shown in Figure 1.3. Similarly, in Figure 1.14, the 2D normalized radiation pattern of the elevation difference channel is shown on top of 2D normalized radiation pattern of the sum channel for the antenna shown in Figure 1.3. As it can be seen from Figure 1.13 and Figure 1.14, when all three monopulse radiation patterns are radiated from the same physical aperture, beam width (10 dB) of difference channels are two times of beam width of sum radiation pattern in their corresponding plane.

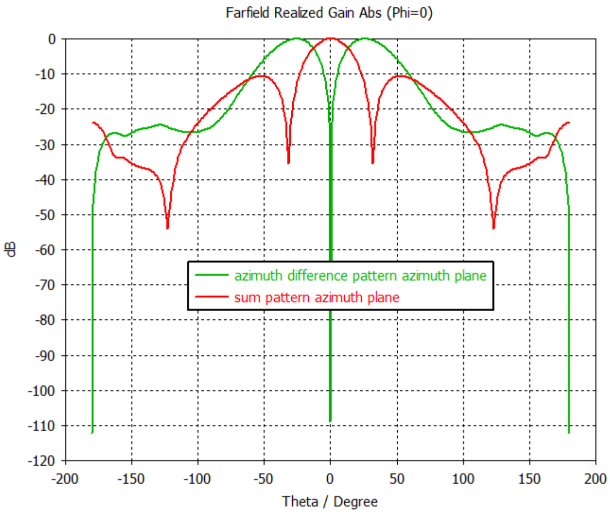

Figure 1.13: The 2D normalized radiation pattern of azimuth difference channel is shown on top of 2D normalized radiation pattern of sum channel

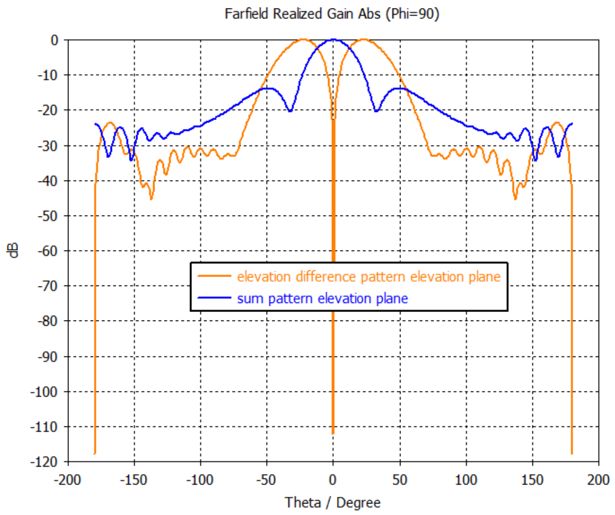

Figure 1.14: The 2D normalized radiation pattern of elevation difference channel is shown on top of 2D normalized radiation pattern of sum channel

Therefore, if the monopulse antenna given in Figure 1.3 is used as a feeding element of focusing antenna system (e.g. reflector antenna), the question of for which radiation pattern the reflector dimension and curvature should be optimized arises. If the reflector is optimized for sum channel, the almost half of energy of difference channel cannot be reflected by reflector antenna (spill over loss). As a result, gain is decreased for difference channels and side lobes are increased. If the reflector is optimized for one of difference channels, the illumination loss is increased for sum pattern and the gain is decreased. Usually the reflector is optimized for the middle point of these two cases and neither radiation pattern shows its full performance [25].

Figure 1.15 summarizes and illustrates the problem explained in two previous paragraphs [25].

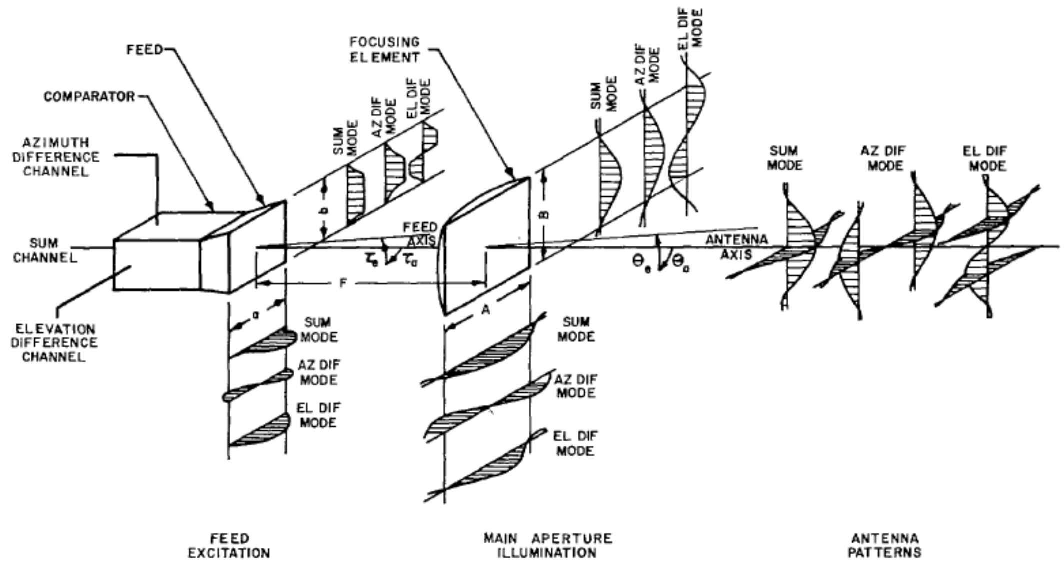

Figure 1.15: The summary of beam optimization problem in conventional monopulse feeds [25]

Different techniques can be found in the literature to overcome different beam widths of three monopulse channel radiation patterns. These techniques are briefly summarized below:

<u>Using different aperture sizes for different monopulse channels:</u> The idea behind this technique is as follows. Assume that sum channel radiated from aperture whose size is $a \times a$. Then if the azimuth channel is radiated from $2a \times a$ aperture size and the elevation channel is radiated from $a \times 2a$ aperture size, the problem is solved, and all three radiation patterns have nearly same beam widths. Example for such a solution is given in Figure 1.16 [27]. It uses 12 horn antennas and the idea for its comparator design is also shown.

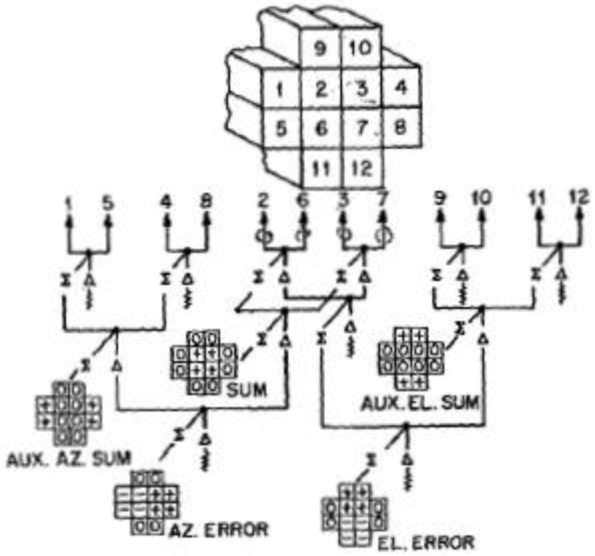

Figure 1.16: Twelve horn antenna monopulse feed [27]

Horn number 2, 3, 6 and 7 are used to radiate sum channel pattern. Horn number 1, 2, 3, 4, 5, 6, 7 and 8 are used to radiate azimuth difference channel. Horn number 9, 10, 2, 3, 6, 7, 11 and 12 are used to radiate elevation difference channel. The only problem with this design is that the comparator design becomes complex and the number of required couplers to be used is increased.

<u>Multimode monopulse feeds:</u> For waveguide structures, instead of using horn array and comparator to create three monopulse channel radiation patterns, different modes of waveguides can be used to generate three different monopulse radiation patterns. The choice of which modes will be radiated depends of type of waveguide (cylindrical, rectangular etc.) and the applications. Multimode feed can radiate all three monopulse radiation patterns from single horn. As a result, very compact feed designs can be obtained. Please note that instead of comparator, multimode monopulse feeds need mode converters to create required waveguide modes.

<u>Combination of conventional and multimode monopulse feeds (multi horn-multimode monopulse feeds):</u> This type of feed combines the advantages of previous two types of

monopulse feeds. This type of feed has horn array, mode conversion sections and comparators. A good example for this type can be found in [28] , [29] and [30].

1.3. Multimode Monopulse Feeds

The idea behind monopulse feeds is as follows: If the similar overall aperture field of the horn array of the conventional monopulse feed can be created by radiating different modes or mode combinations for different monopulse channels instead of using horn array and comparator and radiating only TE_{10} dominant mode or all monopulse channels, then similar far field patterns can be obtained by using one horn and radiating required modes. These required modes and/or mode combinations are created by mode conversion sections (mode converters). The selection of modes and/or mode combinations are dependent on the chosen waveguide structure. If this mode conversion sections are proficiently designed, then multimode monopulse designs can be more compact than the conventional monopulse feeds. This feature can be very important when these monopulse antennas are used as feeds of the reflector antennas (especially prime focus reflectors).

Some examples for multimode monopulse feeds can be found in [31], [32], [33], [34], [35], [36], [37], [38] and [39].

1.4. Thesis Motivation and Contribution

The motivation of the thesis is to investigate which mode converters can be used to obtain required modes for monopulse radiation patterns when the rectangular waveguide substructure is used. The selection of the modes is same as in [37] & [40]. According to this choice:

- TE_{10} mode or the combination of TE_{10} and TE_{30} modes are radiated from single horn aperture to create sum channel radiation pattern. When the combination of TE_{10} and TE_{30} modes is carefully adjusted, TE_{30} mode can be used to cancel sidelobes of TE_{10} mode radiation pattern.
- TE_{20} mode is radiated from the single horn to create azimuth difference radiation pattern

- The TE_{11} and TM_{11} mode combination is radiated from single horn to create elevation difference radiation pattern.

Different types of mode converters to generate these modes are investigated in this thesis, and several mode converters are designed for this purpose by using CST Microwave Studio®. One of these designed mode converters are fabricated using 3D printer and their S parameters and radiation patterns are measured to validate mode converter design techniques and the accuracy of CST Microwave Studio® simulation software.

More details about these modes and the visualization of their electric and magnetic field vectors are given in Chapter 2.

1.5. Thesis Organization

As it is stated, this thesis is focused on rectangular waveguide mode converters for creating monopulse radiation patterns. Hence, the chapters are organized to present details about rectangular waveguide modes, rectangular waveguide mode converter designs and fabrication of one of the designed rectangular mode converter.

Chapter 2 contains fundamental knowledge on wave equation, solution of wave equation in rectangular waveguide structures (rectangular waveguide modes) and detailed information on the rectangular waveguide modes to be used this thesis.

Chapter 3 contains three different rectangular waveguide mode conversion techniques that can be used to convert fundamental mode TE_{10} to required modes to create monopulse radiation patterns. For each mode conversion technique, all required mode converter designs are also given in that chapter.

Chapter 4 contains fabrication details of selected rectangular waveguide mode converter design and the comparison of its measurement and simulation results.

Chapter 5 concludes the work done in this thesis, while that chapter also presents the future works.

CHAPTER 2

BACKGROUND

In this chapter fundamental background information about rectangular waveguides and rectangular waveguide modes are given. [41] is used as reference. At the end of this chapter (in section 2.2.), rectangular waveguide modes used in this thesis are visualized by the help of CST Microwave Studio software®.

2.1. Solutions of Wave Equations in Rectangular Waveguides (Rectangular Waveguide Modes)

Solutions (field distributions, modes) of wave equations must always satisfy Maxwell's equations and boundary conditions. Depending on their field configurations (modes), there are 3 main types of modes of electromagnetic waves, namely: TEM (Transverse Electromagnetic) modes, TE (Transverse Electric, H modes) modes and TM (transverse Magnetic, E modes) modes.

For TEM modes, electric and magnetic field components are transverse to direction specified by superscript (e.g. for TEM^z modes electric and magnetic fields only exist in the plane which is orthogonal to z direction). For TE modes, electric field components are transverse to direction specified by superscript. Only magnetic field **H** have component in that direction. That is why TE modes are sometimes called H modes. For TM modes, magnetic field components are transverse to direction specified by superscript. Only electric field **E** have component in that direction. That is why TM modes are sometimes called E modes.

Only TE and TM modes can exist in rectangular waveguides, TEM modes cannot exist because they do not satisfy boundary conditions on the walls of rectangular hollow waveguides.

TE and TM mode solutions for different rectangular coordinate directions (TE^x, TM^x, TE^y, TM^y, TE^z, TM^z) are given in [41]. If the waveguide whose dimensions shown in Figure 2.1 and which lies along z direction is considered, TE^z and TM^z mode solutions are sufficient for this thesis.

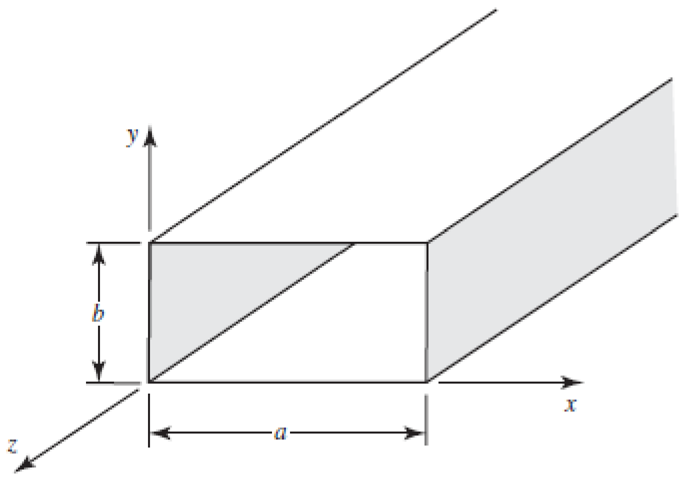

Figure 2.1: Considered rectangular waveguide model [41]

2.1.1. TE^z Modes of Rectangular Waveguide

Details of obtaining the field solutions for TE^z modes are given in [41]. In summary, TE^z_{mn} field expressions are given below:

$$E_x = A_{mn}\frac{\beta_y}{\varepsilon}\cos(\beta_x x)\sin(\beta_y y)e^{-j\beta_z z} \qquad (2\text{-}1a)$$

$$E_y = -A_{mn}\frac{\beta_x}{\varepsilon}\sin(\beta_x x)\cos(\beta_y y)e^{-j\beta_z z} \qquad (2\text{-}1b)$$

$$E_z = 0 \qquad (2\text{-}1c)$$

$$H_x = A_{mn}\frac{\beta_x\beta_z}{w\mu\varepsilon}\sin(\beta_x x)\cos(\beta_y y)e^{-j\beta_z z} \qquad (2\text{-}1d)$$

$$H_y = A_{mn}\frac{\beta_y\beta_z}{w\mu\varepsilon}\cos(\beta_x x)\sin(\beta_y y)e^{-j\beta_z z} \qquad (2\text{-}1e)$$

$$H_z = -jA_{mn}\frac{\beta_c^{\,2}}{w\mu\varepsilon}\cos(\beta_x x)\cos(\beta_y y)e^{-j\beta_z z} \tag{2-1f}$$

$$\beta_c^{\,2} = (\frac{2\pi}{\lambda_c})^2 = \beta^2 - \beta_z^{\,2} = \beta_x^{\,2} + \beta_y^{\,2} = \left(\frac{m\pi}{a}\right)^2 + \left(\frac{n\pi}{b}\right)^2 \tag{2-1g}$$

$$\beta_x = \left(\frac{m\pi}{a}\right) \quad m = 0,1,2,\dots \tag{2-1h}$$

$$\beta_y = \left(\frac{n\pi}{b}\right) \quad n = 0,1,2,\dots \tag{2-1i}$$

$$A_{mn} = A_1 B_1 C_1 \tag{2-1j}$$

Each m and n combination solution represent different $TE^z{}_{mn}$ mode. The values of m & n cannot be 0 simultaneously because it is trivial solution (if both m and n equal to 0, F_Z is constant and all components of electric and magnetic fields are zero).

β_x, β_y and β_z are called wave numbers (eigenvalues) in the x, y and z directions respectively.

β_c equals to β when $\beta_z = 0$ and it is called cut-off wave number.

$$\beta_c = \beta|_{\beta_z=0} = w\sqrt{\mu\varepsilon}|_{\beta_z=0} = w_c\sqrt{\mu\varepsilon} = 2\pi f_c\sqrt{\mu\varepsilon} = \sqrt{\left(\frac{m\pi}{a}\right)^2 + \left(\frac{m\pi}{b}\right)^2} \tag{2-2}$$

$$\Rightarrow (f_c)_{mn} = \frac{1}{2\pi\sqrt{\mu\varepsilon}}\sqrt{\left(\frac{m\pi}{a}\right)^2 + \left(\frac{n\pi}{b}\right)^2} \quad \begin{matrix} m=0,1,2,\dots \\ n=0,1,2,\dots \end{matrix} \tag{2-3}$$

$(f_c)_{mn}$ is called cut-off frequency of mn mode. If two modes have same cut-off frequencies, they are usually referred as degenerate modes.

Rectangular waveguides show high-pass characteristics. Each mode starts to propagate after its cut-off frequency. The mode with the lowest cutoff frequency is called dominant mode. It should be pointed out that dominant mode and the cut-off frequencies are dependent on cross sectional dimensions a & b. If a>b (which is usually the case), the dominant mode is $TE^z{}_{10}$.

The ratio

$$R_{mn} = \frac{(f_c)_{mn}{}^{TE}}{(f_c)_{10}{}^{TE}} = \sqrt{(m)^2 + (\frac{na}{b})^2} \qquad (2\text{-}4)$$

shows the ratio of cut-off frequency of TE^z_{mn} mode to cut-off frequency of TE^z_{10} mode and it can be used to show in which sorting the modes start to propagate and their relative cut-off frequencies with respect to cut-off frequency of TE^z_{10} dominant mode (a>b). Table 2.1 shows the R_{mn} of different TE^z modes with respect to a/b ratio.

Table 2.1: $\boldsymbol{R_{mn}}$ of different TE^z modes with respect to a/b ratio [41]

a/b	10	5	2.25	2	1
m,n R_{mn}	1,0 1	1,0 1	1,0 1	1,0 1	1,0; 0,1 1
m,n R_{mn}	2,0 2	2,0 2	2,0 2	2,0;0,1 2	1,1 1.414
m,n R_{mn}	3,0 3	3,0 3	0,1 2.25	1,1 2.236	2,0 2
m,n R_{mn}	4,0 4	4,0 4	1,1 2.462	2,1 2.828	2,1;1,2 2.236
m,n R_{mn}	5,0 5	5,0;0,1 5	3,0 3	3,0 3	2,2 2.828
m,n R_{mn}	6,0 6	1,1 5.099	2,1 3.010	3,1 3.606	3,0;0,3 3
m,n R_{mn}	7,0 7	2,1 5.385	3,1 3.75	4,0;0,2 4	3,1;1,3 3.162
m,n R_{mn}	8,0 8	3,1 5.831	4,0 4	1,2 4.123	3,2;2,3 3.606
m,n R_{mn}	9,0 9	6,0 6	0,2 4.5	4,1;2,2 4.472	4,0;0,4 4
m,n R_{mn}	10,0;0,1 10	4,1 6.403	4,1 4.589	5,0;3,2 5	4,1;1,4 4.123

Using (2-1g) β_z can be found as

$$
(\beta_z)_{mn} = \begin{cases} \beta\sqrt{1-\left(\frac{\lambda}{\lambda_c}\right)^2} = \beta\sqrt{1-\left(\frac{f_c}{f}\right)^2} & for\ f > f_c \\ 0 & for\ f = f_c \\ -j\beta\sqrt{\left(\frac{\lambda}{\lambda_c}\right)^2 - 1} = -j\beta\sqrt{\left(\frac{f_c}{f}\right)^2 - 1} & for\ f < f_c \end{cases} \qquad (2\text{-}5)
$$

When $f > (f_c)_{mn}$, $(\beta_z)_{mn}$ is real, it means that mn mode is propagating (it can be seen from field expression (2-1a) -(2-1j)). When $f = (f_c)_{mn}$, it means mn mode is standing wave and it is at the edge of propagation ($e^{-j\beta_z z} = 1$ in equations (2-1a) – (2-1j)). When $f < (f_c)_{mn}$, $(\beta_z)_{mn}$ is imaginary, mn mode evanescent (nonpropagating, reactive mode) mode and fields are exponentially decaying in z direction.

$(\lambda_z)_{mn}$ (i.e. wavelength in z direction of mn mode) is sometimes called guided wavelength of that mode $(\lambda_g)_{mn}$ and it is equals to

$$
(\lambda_z)_{mn} = (\lambda_g)_{mn} = \frac{2\pi}{\beta_z} \qquad (2\text{-}6)
$$

Wave impedance of TE^z_{mn} can be found by

$$
Z_w(TE^z{}_{mn}) = \frac{E_x}{H_y} = -\frac{E_y}{H_x} = \frac{w\mu}{\beta_z} \qquad (2\text{-}7)
$$

For simplicity $TE^z{}_{mn}$ modes will be referred as TE_{mn} modes in the other parts of this thesis.

2.1.2. TM^z Modes of Rectangular Waveguide

Details of obtaining the field solutions for TM^z modes are given in [41]. In summary, TM^z_{mn} field expressions are given below:

$$
E_x = -B_{mn}\frac{\beta_x\beta_z}{w\mu\varepsilon}\cos(\beta_x x)\sin(\beta_y y)e^{-j\beta_z z} \qquad (2\text{-}8a)
$$

$$
E_y = -B_{mn}\frac{\beta_y\beta_z}{w\mu\varepsilon}\sin(\beta_x x)\cos(\beta_y y)e^{-j\beta_z z} \qquad (2\text{-}8b)
$$

$$
E_z = -jB_{mn}\frac{{\beta_c}^2}{w\mu\varepsilon}\sin(\beta_x x)\sin(\beta_y y)e^{-j\beta_z z} \qquad (2\text{-}8c)
$$

$$H_x = B_{mn}\frac{\beta_y}{\mu}\sin(\beta_x x)\cos(\beta_y y)e^{-j\beta_z z} \quad \text{(2-8d)}$$

$$H_y = -B_{mn}\frac{\beta_x}{\mu}\cos(\beta_x x)\sin(\beta_y y)e^{-j\beta_z z} \quad \text{(2-8e)}$$

$$H_z = 0 \quad \text{(2-8f)}$$

$$\beta_c{}^2 = (\frac{2\pi}{\lambda_c})^2 = \beta^2 - \beta_z{}^2 = \beta_x{}^2 + \beta_y{}^2 = \left(\frac{m\pi}{a}\right)^2 + \left(\frac{n\pi}{b}\right)^2 \quad \text{(2-8g)}$$

$$\beta_x = \left(\frac{m\pi}{a}\right) \qquad m = 1,2,\dots \quad \text{(2-8h)}$$

$$\beta_y = \left(\frac{n\pi}{b}\right) \qquad n = 1,2,\dots \quad \text{(2-8i)}$$

$$B_{mn} = A_2 B_2 C_1 \quad \text{(2-8j)}$$

$$(f_c)_{mn} = \frac{1}{2\pi\sqrt{\mu\varepsilon}}\sqrt{\left(\frac{m\pi}{a}\right)^2 + \left(\frac{n\pi}{b}\right)^2} \quad \substack{m=1,2,\dots \\ n=1,2,\dots} \quad \text{(2-8k)}$$

The TM^Z mode which has the lowest cut-off frequency is $TM^Z{}_{11}$ mode. For a>b, cut-off frequency of $TE^Z{}_{10}$ is lower than $TM^Z{}_{11}$, $TE^Z{}_{10}$ is the lowest mode.

To complete the illustration of mode starting order for a>b case, the ratio

$$T_{mn} = \frac{(f_c)_{mn}{}^{TM}}{(f_c)_{10}{}^{TE}} = \sqrt{(m)^2 + (\frac{na}{b})^2} \quad \text{(2-9)}$$

is defined and it shows the ratio of cut-off frequency of $TM^z{}_{mn}$ mode to cut-off frequency of $TE^z{}_{10}$ mode. Table 2.2 shows the T_{mn} of different TM^z modes with respect to a/b ratio.

Table 2.2: $\boldsymbol{T_{mn}}$ of different TM^z modes with respect to a/b ratio [41]

$a/b \Rightarrow$	10	5	2.25	2	1
$m,n \Rightarrow$ $T_{mn} \Rightarrow$	1,1 10.05	1,1 5.10	1,1 2.46	1,1 2.23	1,1 1.414
$m,n \Rightarrow$ $T_{mn} \Rightarrow$	2,1 10.19	2,1 5.38	2,1 3.01	2,1 2.83	2,1;1,2 2.236
$m,n \Rightarrow$ $T_{mn} \Rightarrow$	3,1 10.44	3,1 6.00	3,1 3.75	3,1 3.61	2,2 2.828
$m,n \Rightarrow$ $T_{mn} \Rightarrow$	4,1 10.77	4,1 6.40	4,1 4.59	1,2 4.12	3,1;1,3 3.162
$m,n \Rightarrow$ $T_{mn} \Rightarrow$	5,1 11.18	5,1 7.07	1,2 5.09	4,1;2,2 4.47	3,2;2,3 3.606
$m,n \Rightarrow$ $T_{mn} \Rightarrow$	6,1 11.66	6,1 7.81	2,2 5.38	3,2 5.00	4,1;1,4 4.123
$m,n \Rightarrow$ $T_{mn} \Rightarrow$	7,1 12.21	7,1 8.60	3,2 5.41	5,1 5.39	3,3 4.243
$m,n \Rightarrow$ $T_{mn} \Rightarrow$	8,1 12.81	8,1 9.43	5,1 5.48	4,2 5.66	4,2;2,4 4.472
$m,n \Rightarrow$ $T_{mn} \Rightarrow$	9,1 13.82	1,2 10.04	4,2 6.40	1,3 6.08	4,3;3,4 5.00
$m,n \Rightarrow$ $T_{mn} \Rightarrow$	10,1 14.14	2,2 10.20	6,1 6.41	2,3 6.32	5,1;1,5 5.09

Equations for β_z and $(\lambda_g)_{mn}$ are same as in TE^Z modes ((2-5) & (2-6)). Comments on the cases when $f < f_c$, $f = f_c$ and $f > f_c$ are also valid for TM^z modes.

Wave impedance of TM$^z{}_{mn}$ can be found by

$$Z_w(\mathrm{TM}^z{}_{mn}) = \frac{E_x}{H_y} = -\frac{E_y}{H_x} = \frac{\beta_z}{w\varepsilon} \qquad (2\text{-}10)$$

For simplicity TM$^z{}_{mn}$ modes will be referred as TM$_{mn}$ modes in the other parts of this thesis.

2.2. Rectangular Waveguides Modes Used in This Thesis

TE_{10}, TE_{20}, TE_{30}, TE_{11} and TM_{11} modes are highly important for this thesis. As mentioned in section 1.4:

- TE_{10} mode to TE_{20} mode converters are investigated for obtaining azimuth difference monopulse radiation pattern
- TE_{10} mode to combination of TE_{11}+TM_{11} modes converters are investigated for obtaining elevation difference monopulse radiation pattern
- TE_{10} mode to TE_{30} mode converters and TE_{10} mode to combination of TE_{10}+TE_{30} modes converter are investigated for shaping sum monopulse radiation pattern.

In this section, the electric fields and the magnetic fields of these modes will be visualized when they are propagating in arbitrary length rectangular waveguide with the aid of CST Microwave Studio® software.

2.2.1. TE_{10} Mode

The equations for electric and magnetic fields of TE_{10} mode can be obtained when m=1 and n=0 in (2-1):

$$\mathrm{E_x} = 0 \qquad \mathrm{H_x} = \mathrm{A_{10}} \frac{\beta_z}{\mathrm{w}\mu\varepsilon}\left(\frac{\pi}{a}\right)\sin\left(\frac{\pi}{a}\mathrm{x}\right)\mathrm{e}^{-\mathrm{j}\beta_z \mathrm{z}}$$

$$\mathrm{E_y} = -\mathrm{A_{10}}\frac{\pi}{a\varepsilon}\sin\left(\frac{\pi}{a}\mathrm{x}\right)\mathrm{e}^{-\mathrm{j}\beta_z \mathrm{z}} \qquad \mathrm{H_y} = 0 \tag{2-11}$$

$$\mathrm{E_z} = 0 \qquad \mathrm{H_z} = -\mathrm{j}\mathrm{A_{10}}\frac{1}{\mathrm{w}\mu\varepsilon}\left(\frac{\pi}{a}\right)^2\cos\left(\frac{\pi}{a}\mathrm{x}\right)\mathrm{e}^{-\mathrm{j}\beta_z \mathrm{z}}$$

$$\beta_x = \left(\frac{\pi}{a}\right) \qquad \beta_y = 0$$

It can be seen from (2-11) that for TE_{10} mode electric field has no x and z component, it only has y component. Magnetic field, on the other hand, has no y component, it has only x and z components.

The cut-off frequency of TE_{10} is

$$(f_c)_{10} = \frac{1}{2\pi\sqrt{\mu\varepsilon}}\left(\frac{\pi}{a}\right) \tag{2-12}$$

In order to visualize electric and magnetic field vectors of TE_{10} mode inside rectangular waveguide, in CST Microwave Studio® software rectangular waveguide shown Figure 2.2 is created. Operating frequency is selected as 10 GHz, and a & b dimension are selected as 24 mm & 12 mm respectively. Length of this waveguide section l equals to 80 mm.

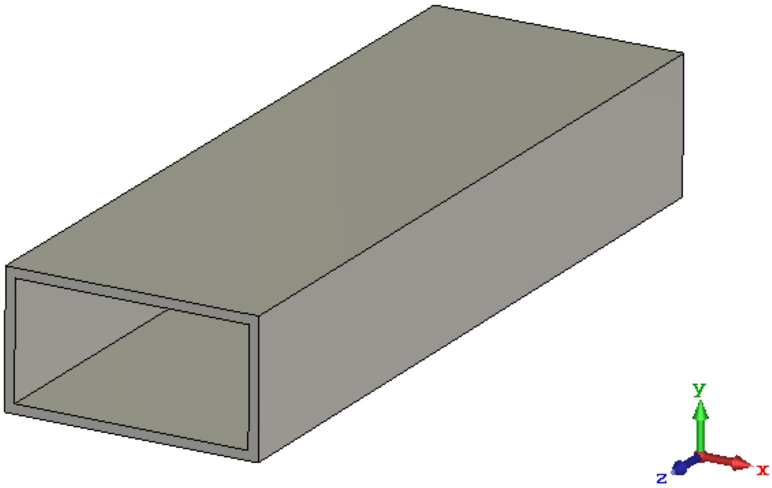

Figure 2.2: Rectangular waveguide with dimensions a = 24 mm, b =12 mm & l = 80 mm

Electric field vectors of TE_{10} mode inside this waveguide is shown in Figure 2.3. Arrows show the direction of electric field in given position and the color shows the magnitude of electric field at that point. The color scale is in normalized dB scale (with respect to largest magnitude of electric field inside the waveguide). As it can be seen from this figure, electric field has only y component.

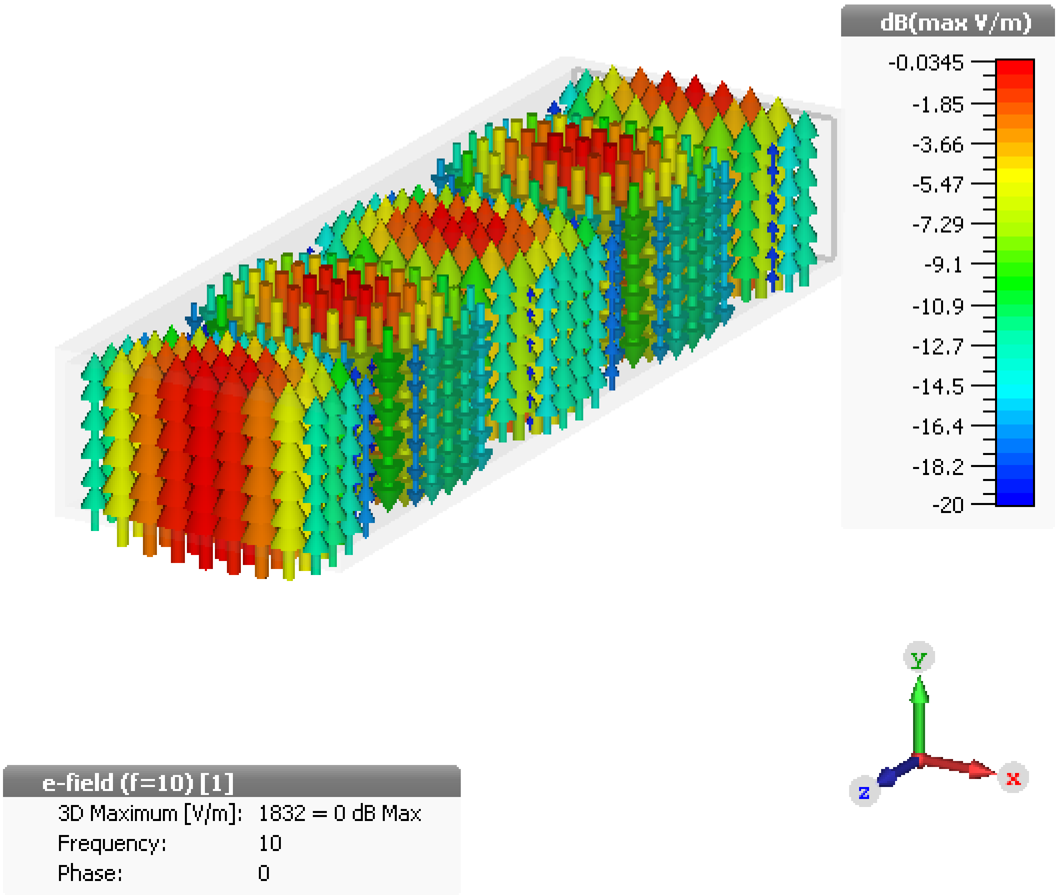

Figure 2.3: Electric field vectors of TE_{10} mode inside rectangular waveguide

Magnetic field vectors of TE_{10} mode inside this waveguide is shown in Figure 2.4. Again, arrows show the direction of electric field in given position and the color shows the magnitude of magnetic field at that point. The color scale is in normalized dB scale (with respect to largest magnitude of magnetic field inside the waveguide). As it can be seen from this figure, magnetic field has only x and z component.

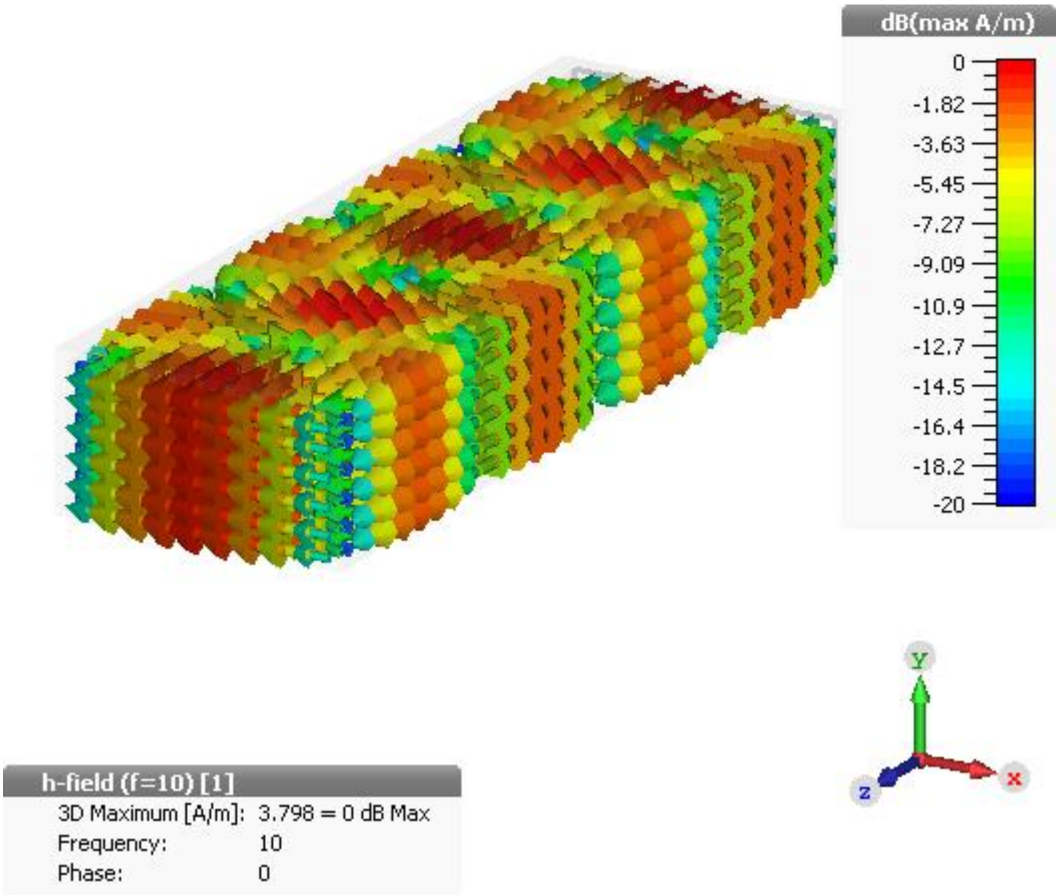

Figure 2.4: Magnetic field vectors of TE_{10} mode inside rectangular waveguide

Figure 2.5 and Figure 2.6 show cross sectional electric and magnetic field vectors of TE_{10} mode at the input.

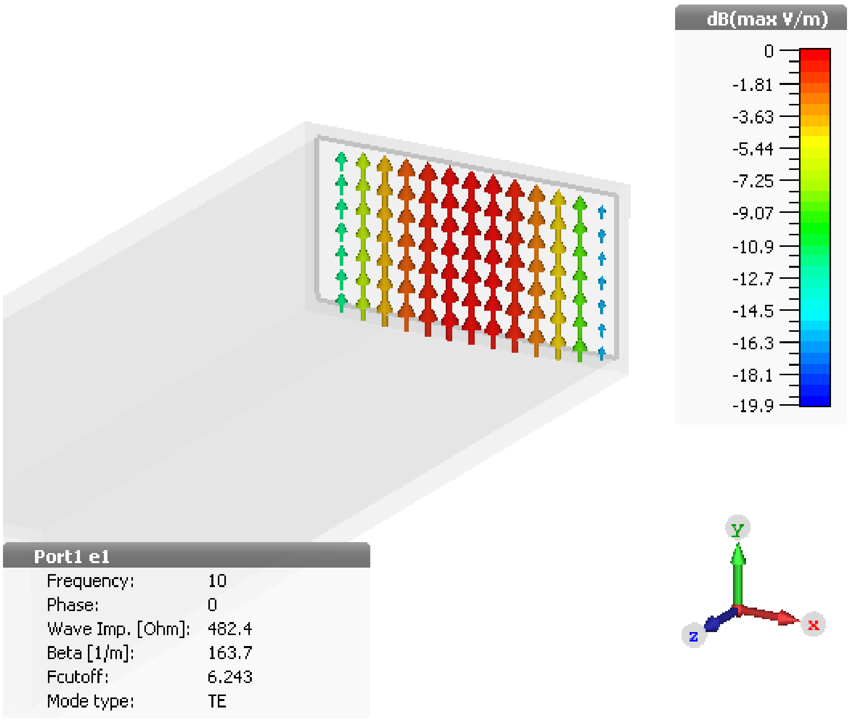

Figure 2.5: Magnetic field vectors of TE_{10} mode inside rectangular waveguide

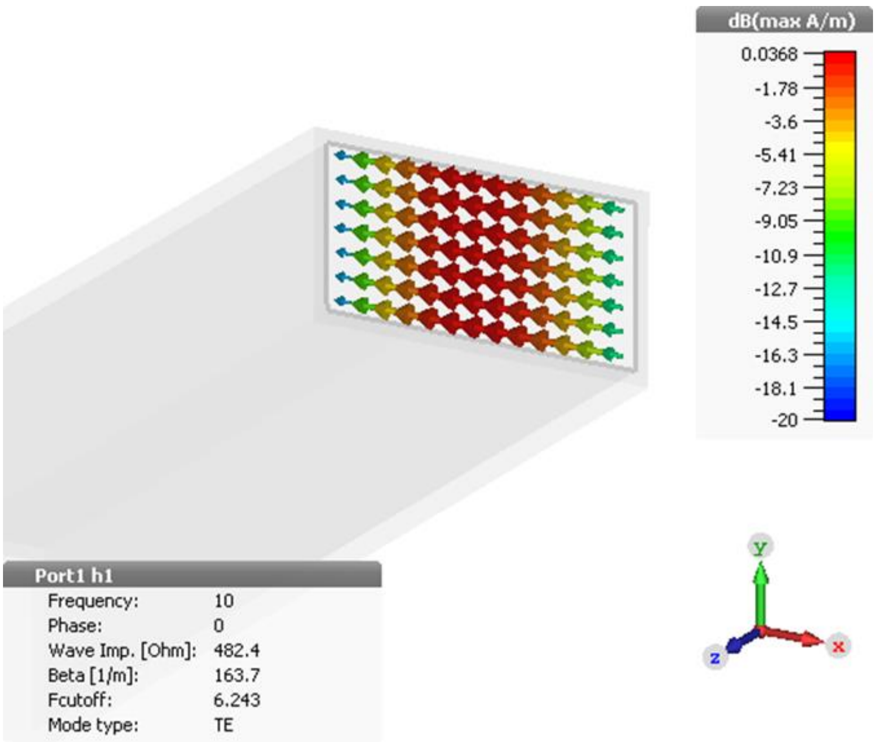

Figure 2.6: Magnetic field vectors of TE_{10} mode inside rectangular waveguide

As it can be seen from Figure 2.5 and Figure 2.6, cut-off frequency of TE_{10} mode of this CST waveguide model (a = 24 mm & b = 12 mm) is calculated as 6.243 GHz and the wave impedance at 10 GHz is found as 482.4 Ohm.

2.2.2. TE_{20} Mode

The equations for electric and magnetic fields of TE_{20} mode can be obtained when $m = 2$ and $n = 0$ in (2-1):

$$E_x = 0 \qquad H_x = A_{20}\frac{\beta_z}{w\mu\varepsilon}\left(\frac{2\pi}{a}\right)\sin\left(\frac{2\pi}{a}x\right)e^{-j\beta_z z}$$

$$E_y = -A_{20}\frac{2\pi}{a\varepsilon}\sin\left(\frac{2\pi}{a}x\right)e^{-j\beta_z z} \qquad H_y = 0 \tag{2-13}$$

$$E_z = 0 \qquad H_z = -jA_{20}\frac{1}{w\mu\varepsilon}\left(\frac{2\pi}{a}\right)^2\cos\left(\frac{2\pi}{a}x\right)e^{-j\beta_z z}$$

$$\beta_x = \left(\frac{2\pi}{a}\right) \qquad \beta_y = 0$$

It can be seen from (2-13) that for TE_{20} mode electric field has no x and z component, it only has y component. Magnetic field, on the other hand, has no y component, it has only x and z components.

The cut-off frequency of TE_{20} is

$$(f_c)_{20} = \frac{1}{2\pi\sqrt{\mu\varepsilon}}\left(\frac{2\pi}{a}\right) \tag{2-14}$$

In order to visualize electric and magnetic field vectors of TE_{20} mode inside rectangular waveguide, in CST Microwave Studio® software rectangular waveguide shown Figure 2.7 is created. Operating frequency is selected as 10 GHz, and a & b dimension are selected as 35 mm & 10.16 mm respectively. Length of this waveguide section l equals to 80 mm.

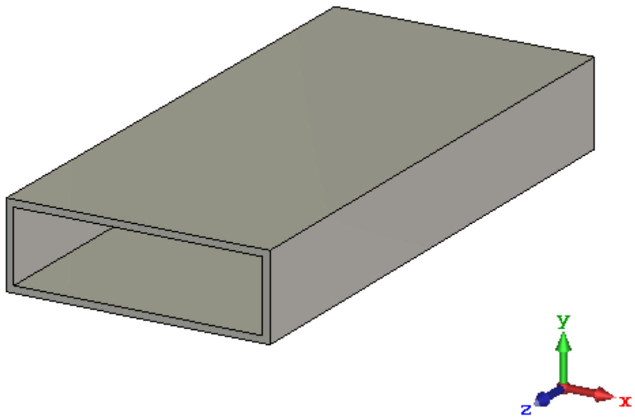

Figure 2.7: Rectangular waveguide with dimensions a = 35 mm, b = 10.16 mm & l = 80 mm

Electric field vectors of TE_{20} mode inside this waveguide is shown in Figure 2.8. Arrows show the direction of electric field in given position and the color shows the magnitude of electric field at that point. The color scale is in normalized dB scale (with respect to largest magnitude of electric field inside the waveguide). As it can be seen from this figure, electric field has only y component.

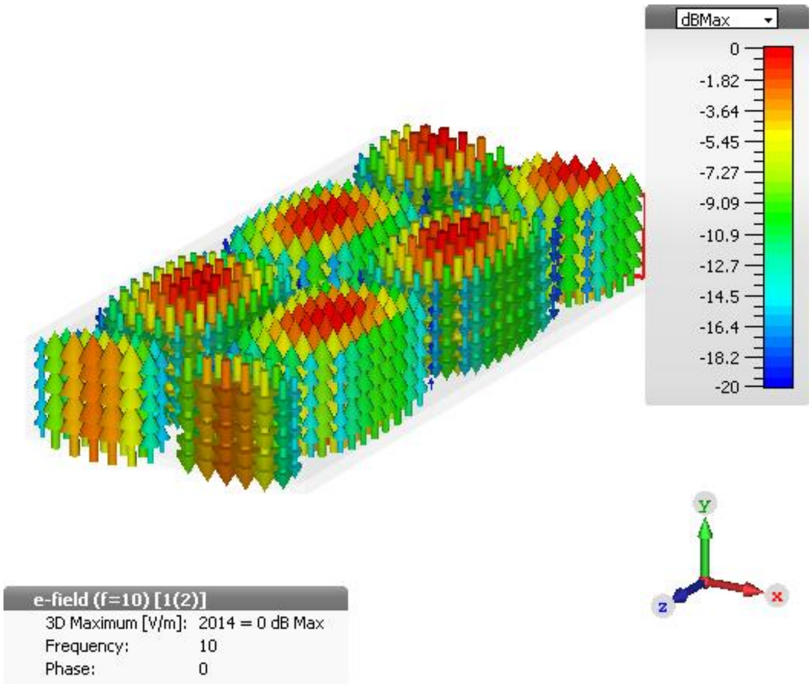

Figure 2.8: Electric field vectors of TE_{20} mode inside rectangular waveguide

Magnetic field vectors of TE_{20} mode inside this waveguide is shown in Figure 2.9. Again, arrows show the direction of electric field in given position and the color shows the magnitude of magnetic field at that point. The color scale is in normalized dB scale (with respect to largest magnitude of magnetic field inside the waveguide). As it can be seen from this figure, magnetic field has only x and z component.

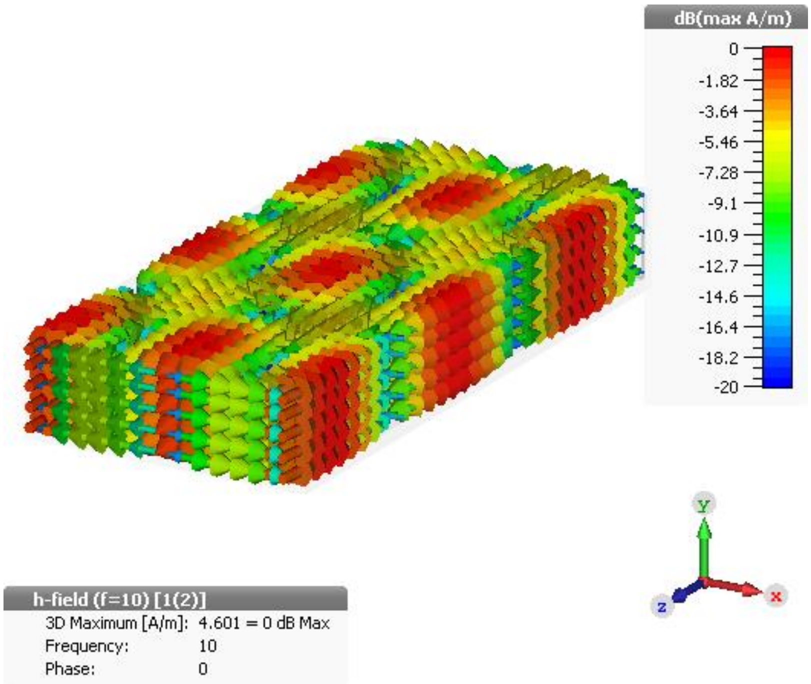

Figure 2.9: Magnetic field vectors of TE_{20} mode inside rectangular waveguide

Figure 2.10 and Figure 2.11 show cross sectional electric and magnetic field vectors of TE_{20} mode at the input.

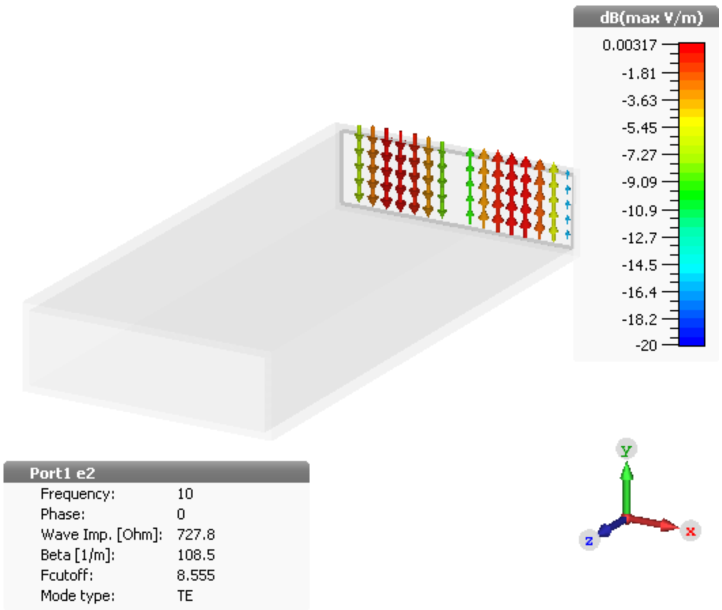

Figure 2.10: Cross sectional electric field vectors of TE_{20} mode at the input

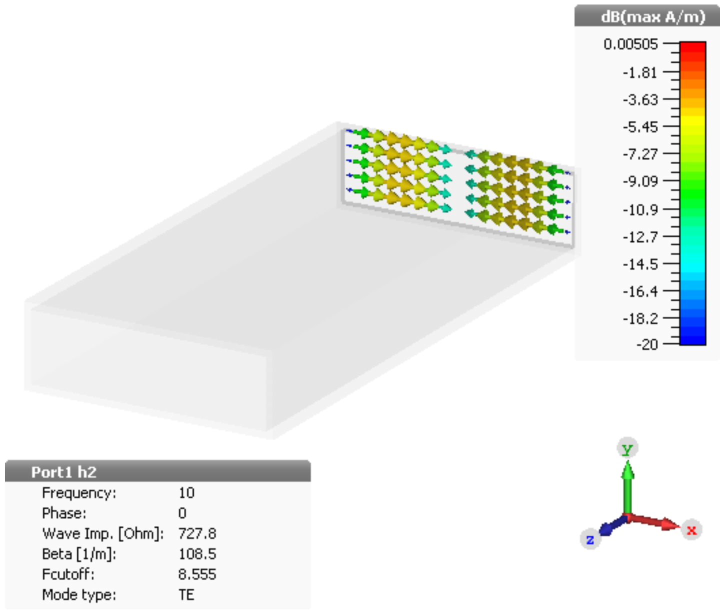

Figure 2.11: Cross sectional magnetic field vectors of TE_{20} mode at the input

As it can be seen from Figure 2.10 and Figure 2.11, cut-off frequency of TE_{20} mode of this CST waveguide model (a = 35 mm & b = 10.16 mm) is calculated as 8.555 GHz and the wave impedance at 10 GHz is found as 727.8 Ohm.

2.2.3. TE_{30} Mode

The equations for electric and magnetic fields of TE_{30} mode can be obtained when $m = 3$ and $n = 0$ in (2-1):

$$E_x = 0 \qquad H_x = A_{30}\frac{\beta_z}{w\mu\varepsilon}\left(\frac{3\pi}{a}\right)\sin\left(\frac{3\pi}{a}x\right)e^{-j\beta_z z}$$

$$E_y = -A_{30}\frac{3\pi}{a\varepsilon}\sin\left(\frac{3\pi}{a}x\right)e^{-j\beta_z z} \qquad H_y = 0 \tag{2-15}$$

$$E_z = 0 \qquad H_z = -jA_{30}\frac{1}{w\mu\varepsilon}\left(\frac{3\pi}{a}\right)^2\cos\left(\frac{3\pi}{a}x\right)e^{-j\beta_z z}$$

$$\beta_x = \left(\frac{3\pi}{a}\right) \qquad \beta_y = 0$$

It can be seen from (2-15) that for TE_{30} mode electric field has no x and z component, it only has y component. Magnetic field, on the other hand, has no y component, it has only x and z components.

The cut-off frequency of TE_{30} is

$$(f_c)_{30} = \frac{1}{2\pi\sqrt{\mu\varepsilon}}\left(\frac{3\pi}{a}\right) \quad (2\text{-}16)$$

In order to visualize electric and magnetic field vectors of TE_{30} mode inside rectangular waveguide, in CST Microwave Studio® software rectangular waveguide shown Figure 2.12 is created. Operating frequency is selected as 10 GHz, and a & b dimension are selected as 52.7 mm & 10.16 mm respectively. Length of this waveguide section l equals to 120 mm.

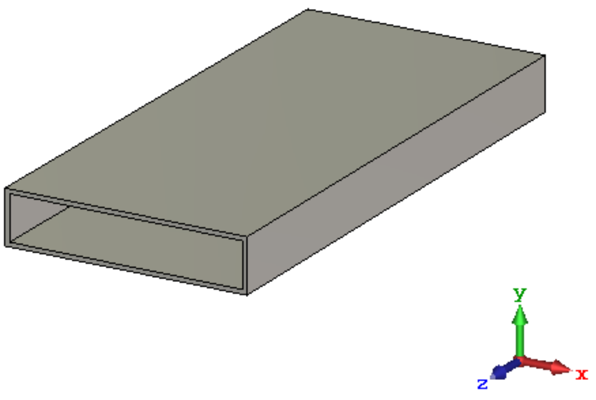

Figure 2.12: Rectangular waveguide with dimensions a = 52.7 mm, b = 10.16 mm & l = 120 mm

Electric field vectors of TE_{30} mode inside this waveguide is shown in Figure 2.13. Arrows show the direction of electric field in given position and the color shows the magnitude of electric field at that point. The color scale is in normalized dB scale (with respect to largest magnitude of electric field inside the waveguide). As it can be seen from this figure, electric field has only y component.

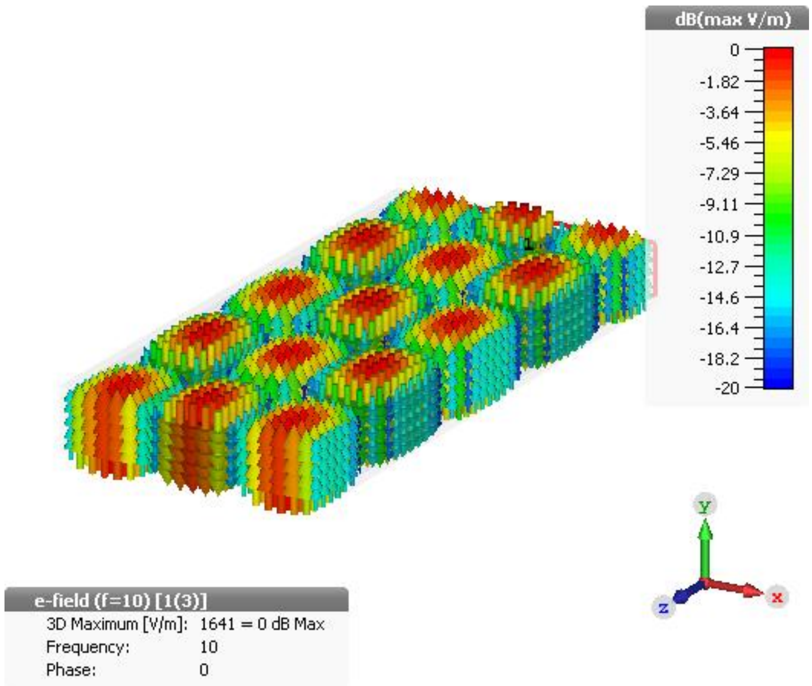

Figure 2.13: Electric field vectors of TE_{30} mode inside rectangular waveguide

Magnetic field vectors of TE_{30} mode inside this waveguide is shown in Figure 2.14. Again, arrows show the direction of electric field in given position and the color shows the magnitude of magnetic field at that point. The color scale is in normalized dB scale (with respect to largest magnitude of magnetic field inside the waveguide). As it can be seen from this figure, magnetic field has only x and z component.

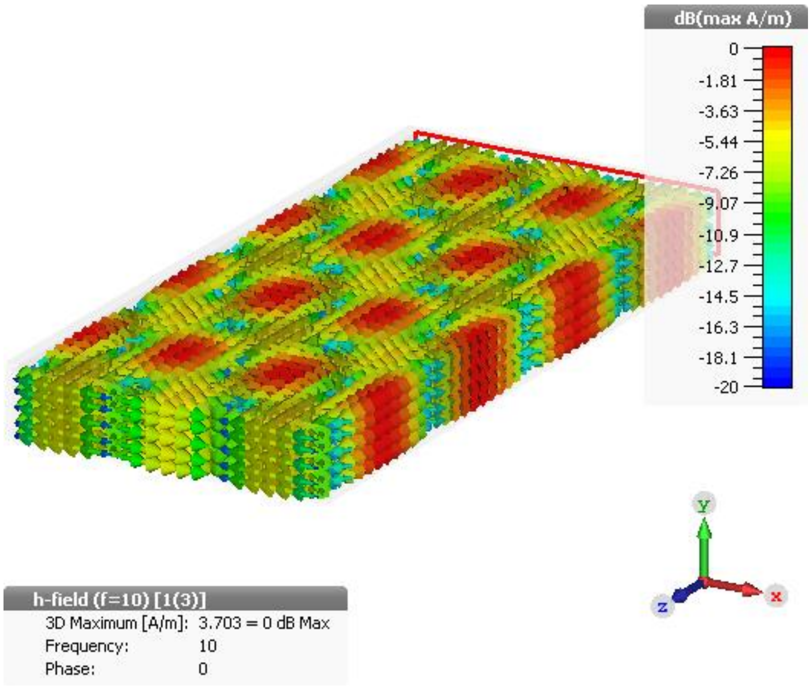

Figure 2.14: Magnetic field vectors of TE_{20} mode inside rectangular waveguide

Figure 2.15 and Figure 2.16 show cross sectional electric and magnetic field vectors of TE_{30} mode at the input.

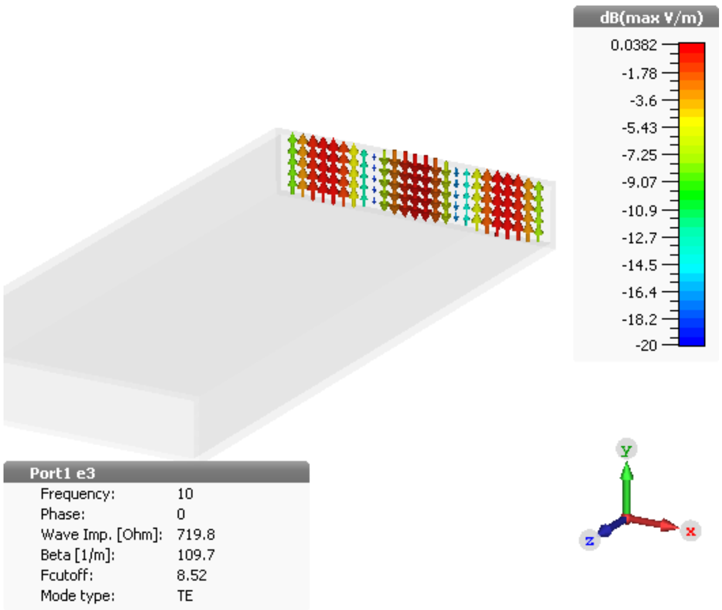

Figure 2.15: Cross sectional electric field vectors of TE_{30} mode at the input

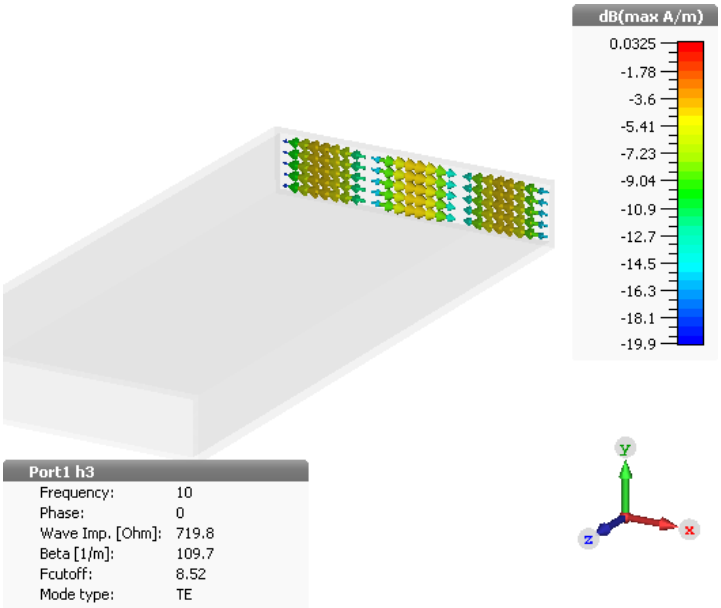

Figure 2.16: Cross sectional magnetic field vectors of TE_{30} mode at the input

As it can be seen from Figure 2.15 and Figure 2.16, cut-off frequency of TE_{30} mode of this CST waveguide model (a = 52.7 mm & b = 10.16 mm) is calculated as 8.52 GHz and the wave impedance at 10 GHz is found as 719.8 Ohm.

2.2.4. TE_{11} Mode

The equations for electric and magnetic fields of TE_{11} mode can be obtained when $m = 1$ and $n = 1$ in (2-1):

$$E_x = A_{11}\frac{\pi}{b\varepsilon}\cos(\beta_x x)\sin(\beta_y y)\, e^{-j\beta_z z} \qquad H_x = A_{11}\frac{\beta_z}{w\mu\varepsilon}\left(\frac{\pi}{a}\right)\sin(\frac{\pi}{a}x)\cos(\frac{\pi}{b}y)e^{-j\beta_z z}$$

$$E_y = -A_{11}\frac{\pi}{a\varepsilon}\sin\left(\frac{\pi}{a}x\right)\cos\left(\frac{\pi}{b}y\right)e^{-j\beta_z z} \qquad H_y = A_{11}\frac{\beta_z}{w\mu\varepsilon}\left(\frac{\pi}{b}\right)\cos(\frac{\pi}{a}x)\sin(\frac{\pi}{b}y)e^{-j\beta_z z}$$

$$E_z = 0 \qquad H_z = -jA_{11}\frac{{\beta_c}^2}{w\mu\varepsilon}\cos\left(\frac{\pi}{a}x\right)\cos\left(\frac{\pi}{b}y\right)e^{-j\beta_z z} \tag{2-17}$$

$$\beta_x = \left(\frac{\pi}{a}\right) \qquad \beta_y = \left(\frac{\pi}{b}\right)$$

It can be seen from (2-17) that for TE_{11} mode electric field has no z component, it only has x and y components. Magnetic field, on the other hand, has all x, y and z components.

The cut-off frequency of TE_{11} is

$$(f_c)_{11} = \frac{1}{2\pi\sqrt{\mu\varepsilon}}\sqrt{\left(\frac{\pi}{a}\right)^2 + \left(\frac{\pi}{b}\right)^2} \quad (2\text{-}18)$$

In order to visualize electric and magnetic field vectors of TE_{11} mode inside rectangular waveguide, in CST Microwave Studio® software rectangular waveguide (square waveguide is also a rectangular waveguide) shown Figure 2.17 is created. Operating frequency is selected as 10 GHz, and a & b dimension are selected as a = b = 24 mm respectively. Length of this waveguide section l equals to 80 mm.

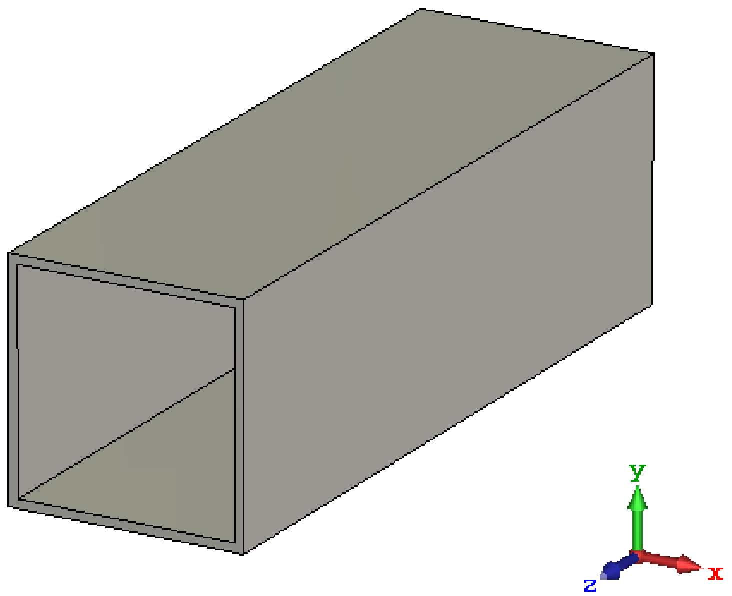

Figure 2.17: Rectangular waveguide with dimensions a = 24 mm, b= 24 mm & l = 80 mm

Electric field vectors of TE_{11} mode inside this waveguide is shown in Figure 2.18. Arrows show the direction of electric field in given position and the color shows the magnitude of electric field at that point. The color scale is in normalized dB scale (with respect to largest magnitude of electric field inside the waveguide).

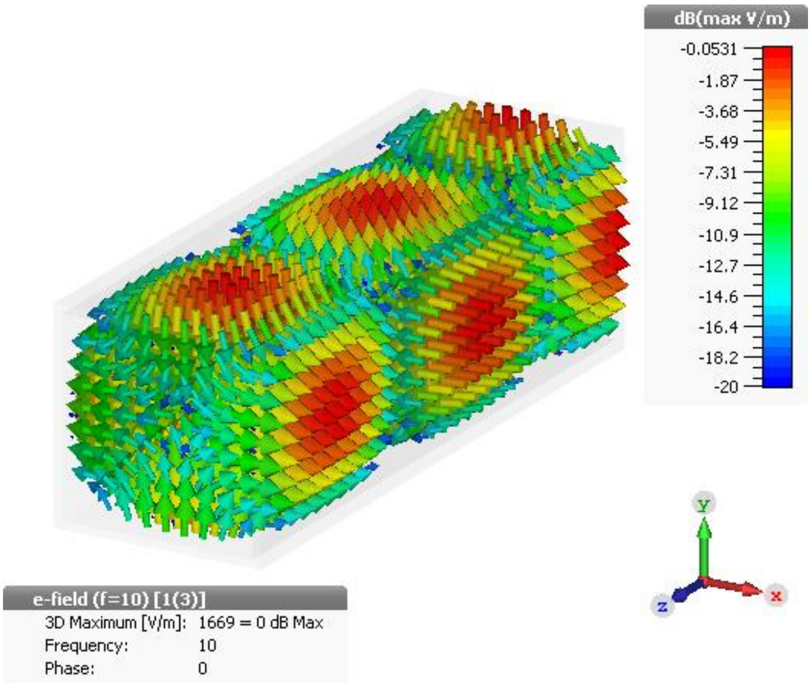

Figure 2.18: Electric field vectors of TE_{11} mode inside rectangular waveguide

Magnetic field vectors of TE_{11} mode inside this waveguide is shown in Figure 2.19. Again, arrows show the direction of electric field in given position and the color shows the magnitude of magnetic field at that point. The color scale is in normalized dB scale (with respect to largest magnitude of magnetic field inside the waveguide.

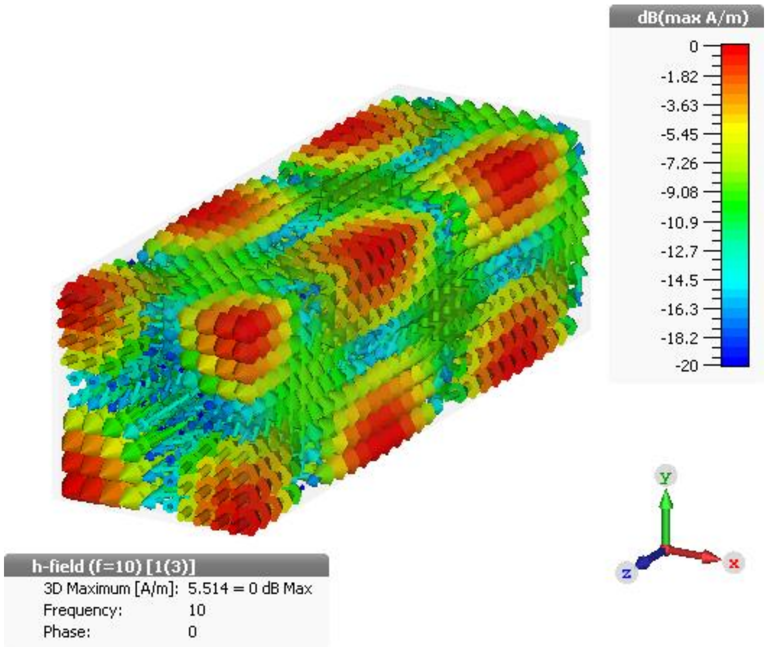

Figure 2.19: Magnetic field vectors of TE_{11} mode inside rectangular waveguide

Figure 2.20 and Figure 2.21 show cross sectional electric and magnetic field vectors of TE_{11} mode at the input.

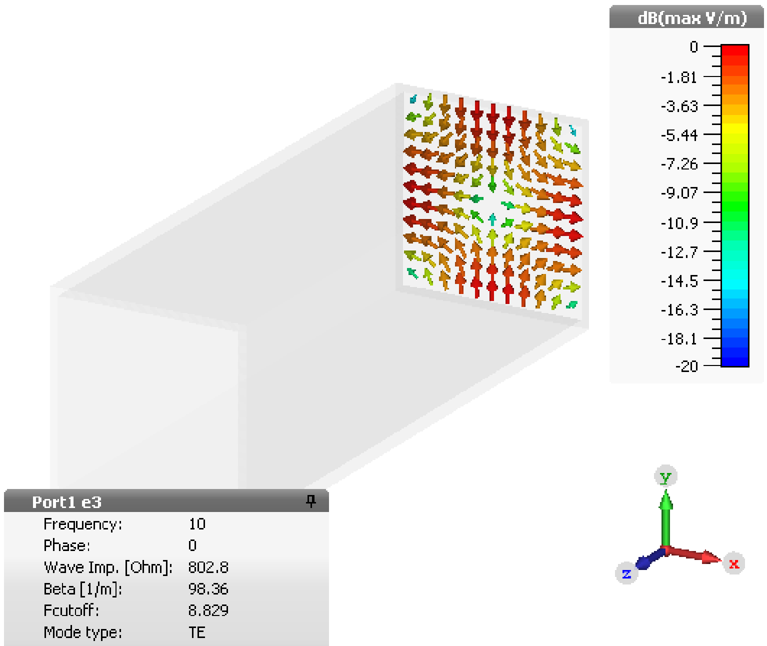

Figure 2.20: Cross sectional electric field vectors of TE_{11} mode at the input

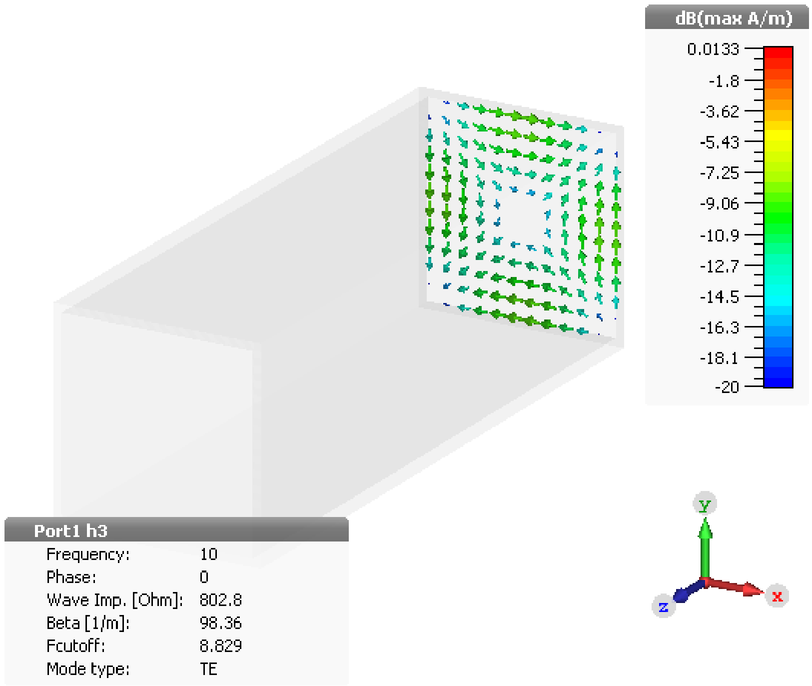

Figure 2.21: Cross sectional magnetic field vectors of TE_{11} mode at the input

As it can be seen from Figure 2.20 and Figure 2.21, cut-off frequency of TE_{11} mode of this CST waveguide model (a = b = 24 mm) is calculated as 8.829 GHz and the wave impedance at 10 GHz is found as 802.8 Ohm.

2.2.5. TM_{11} Mode

The equations for electric and magnetic fields of TM_{11} mode can be obtained when m = 1 and n = 1 in (2-8):

$$E_x = -B_{11}\frac{\beta_z}{w\mu\varepsilon}\left(\frac{\pi}{a}\right)\cos\left(\frac{\pi}{a}x\right)\sin\left(\frac{\pi}{b}y\right)e^{-j\beta_z z} \qquad H_x = B_{11}\frac{\pi}{b\mu}\sin\left(\frac{\pi}{a}x\right)\cos\left(\frac{\pi}{b}y\right)e^{-j\beta_z z}$$

$$E_y = -B_{11}\frac{\beta_z}{w\mu\varepsilon}\left(\frac{\pi}{b}\right)\sin\left(\frac{\pi}{a}x\right)\cos\left(\frac{\pi}{b}y\right)e^{-j\beta_z z} \qquad H_y = -B_{11}\frac{\beta_x}{\mu}\cos\left(\frac{\pi}{a}x\right)\sin\left(\frac{\pi}{b}y\right)e^{-j\beta_z z} \tag{2-19}$$

$$E_z = -jB_{11}\frac{{\beta_c}^2}{w\mu\varepsilon}\sin\left(\frac{\pi}{a}x\right)\sin\left(\frac{\pi}{b}y\right)e^{-j\beta_z z} \qquad H_z = 0$$

$$\beta_x = \left(\frac{\pi}{a}\right) \qquad \beta_y = \left(\frac{\pi}{b}\right)$$

It can be seen from (2-19) that for TM_{11} mode electric field has all x, y and z components. Magnetic field, on the other hand, has only x and y components.

The cut-off frequency of TM_{11} is

$$(f_c)_{11} = \frac{1}{2\pi\sqrt{\mu\varepsilon}}\sqrt{\left(\frac{\pi}{a}\right)^2 + \left(\frac{\pi}{b}\right)^2} \qquad (2\text{-}20)$$

As it can be seen from (2-41) & (2-43), TE_{11} and TM_{11} has the same cut-off frequency expressions. Therefore, these two modes are degenerate modes.

In order to visualize electric and magnetic field vectors of TM_{11} mode inside rectangular waveguide, in CST Microwave Studio® software rectangular waveguide (square waveguide is also a rectangular waveguide) shown Figure 2.17 is created. Operating frequency is selected as 10 GHz, and a & b dimension are selected as a = b = 24 mm respectively. Length of this waveguide section l equals to 80 mm.

Electric field vectors of TM_{11} mode inside this waveguide is shown in Figure 2.22. Arrows show the direction of electric field in given position and the color shows the magnitude of electric field at that point. The color scale is in normalized dB scale (with respect to largest magnitude of electric field inside the waveguide).

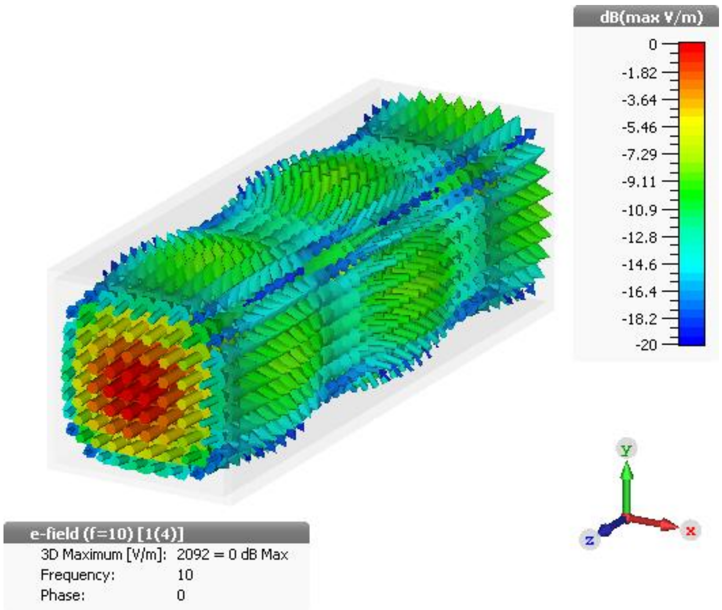

Figure 2.22: Electric field vectors of TM_{11} mode inside rectangular waveguide

Magnetic field vectors of TM_{11} mode inside this waveguide is shown in Figure 2.23. Again, arrows show the direction of electric field in given position and the color shows the magnitude of magnetic field at that point. The color scale is in normalized dB scale (with respect to largest magnitude of magnetic field inside the waveguide.

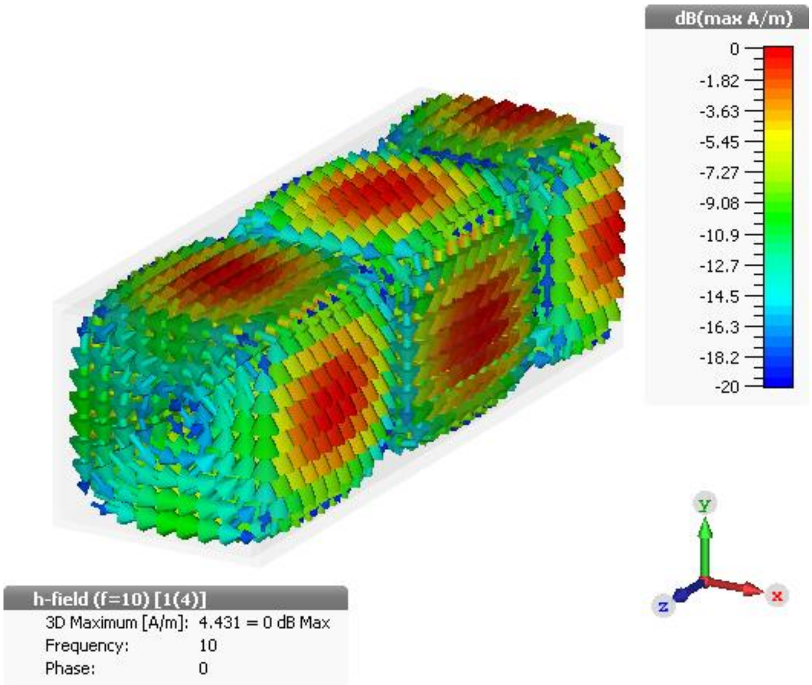

Figure 2.23: Magnetic field vectors of TM_{11} mode inside rectangular waveguide

Figure 2.24 and Figure 2.25 show cross sectional electric and magnetic field vectors of TM_{11} mode at the input.

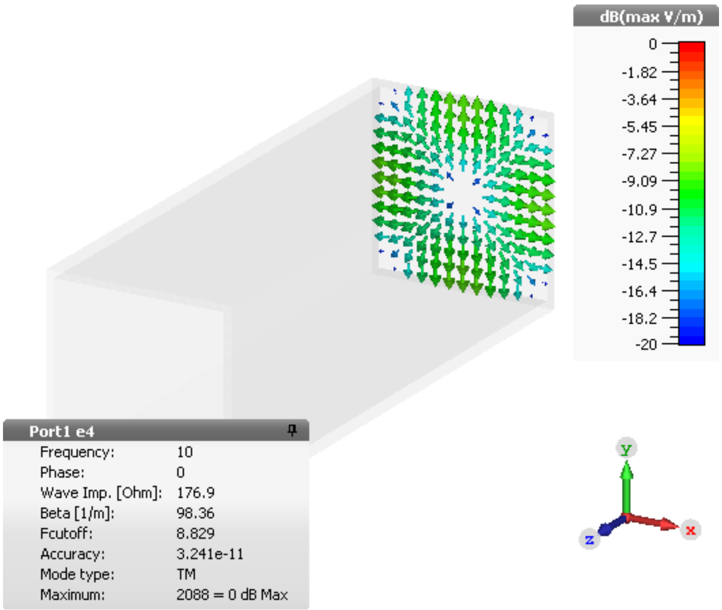

Figure 2.24: Cross sectional electric field vectors of TM_{11} mode at the input

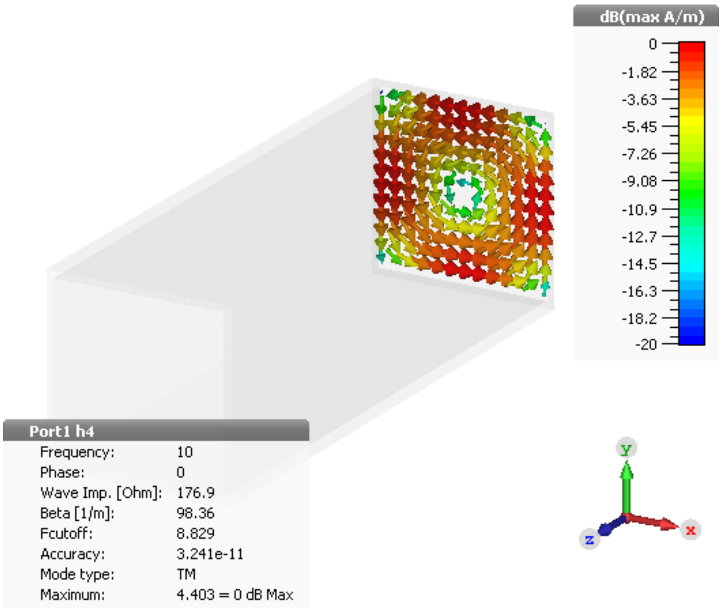

Figure 2.25: Cross sectional magnetic field vectors of TM_{11} mode at the input

As it can be seen from Figure 2.24 and Figure 2.25, cut-off frequency of TM_{11} mode of this CST waveguide model (a = b = 24 mm) is calculated as 8.829 GHz and the wave impedance at 10 GHz is found as 176.9 Ohm.

CHAPTER 3

RECTANGULAR WAVEGUIDE MODE CONVERTER DESIGNS FOR MONOPULSE FEEDS

In this chapter, mode converters based on three different mode generation substructures are designed to obtain rectangular waveguide modes mentioned in section 1.4. These mode generations substructures are irregular (aperiodic) stepped mode generation, corner mode generation, bended waveguide mode generation. The design details of these three mode generation mechanisms to obtain desired rectangular waveguide modes are given in this chapter. The simulation results of designed rectangular mode converters are also given.

In this thesis, the mode conversion is aimed to be achieved at the center frequency fc = 10 GHz (we are only interested in proof of mode conversion operation with given structure, we are not interested in operating bandwidth, so optimization goals are set as single frequency goals according to this approach), the simulations of mode converter designs are done at 8-12 GHz band to observe full X band characteristics. There are two reasons why X band is chosen as operating band for all mode converter designs in this thesis. First reason is related with the measurement infrastructure available. The second reason is that X band is sweet spot when the standard waveguide dimensions are considered. The dimensions are very large in lower frequency bands, so waveguide design in those frequency bands are bulky and expensive to manufacture. The dimensions are very small in upper frequency bands, the manufacturing tolerances become important and the cost of manufacture rises. In addition, the surface roughness in waveguides can become major issue in upper frequency bands. Therefore, X band is thought as a sweet spot for designing mode converters. Although, the mode converter designs are optimized for fc = 10 GHz, the dimensions can be changed to wavelength and then scaled to different frequencies (for example if one of the designs is required to be used in fc = 20 GHz, all physical dimensions of 10 GHz design should be divided by 2, so that the electrical dimensions will be same in terms of wavelength).

3.1. Irregular (Aperiodic) Stepped Mode Converters

A step discontinuity in waveguides are well-known mode generation technique. This step discontinuity can be in the H-plane only, in the E-plane only, or in both E and H planes. If the step discontinuity is introduced in the E-plane, it is usually called "capacitive step". Similarly, if the step discontinuity is introduced in the H-plane, it is called "inductive step". These step discontinuities can be symmetrical or asymmetrical. In Figure 3.1, both symmetric and asymmetric H-plane step discontinuities are shown.

Figure 3.1: Symmetric H-plane step (top view) & Asymmetric H-plane step (top view)

Extensive work for finding the solution of step discontinuity problems is done in literature. The main idea is to match the transverse electric and magnetic fields on the discontinuity junction in terms of modal expansion in both sides of step junction. In addition, the network parameters or the lumped circuit models of step discontinuities in waveguides are also investigated. Some examples for finding the solution of step discontinuity problems and finding the circuit models of these discontinues can be found in [42], [43], [44], [45], [46], [47], [48], [49], [50], [51], [52], [53], [54], [55], [56], [57], [58], [59], [60], [61], [62], [63], [64], [65] and [66]. One can write numerical codes using the formulations given in these papers or one can import the given lumped circuit models into readily available circuit simulator to obtain field solutions when step discontinuities are present. The third method is to use a readily available 3D electromagnetic simulation software (e.g. CST Microwave Studio®) and analyze the behavior of electric and magnetic fields and coupling of modes when step discontinuity present. This third method is chosen for analyzing the fields and mode conversion inside the stepped mode converters.

The cascade of step discontinuities can be used as mode converters. These steps can be periodic (regular, repeating waveguide widths or heights) or they can be aperiodic (irregular). Cascading irregular symmetrical step discontinuities and using optimization tools to optimize widths (and/or heights) and lengths of these steps is known as Scattering Optimization Method (SOM), [67], [68]. Using SOM is superior to using periodic mode converters (which uses corrugations) in terms of physical size (smaller converter length) and performance, [67], [68], [69]. For this reason, periodic stepped converters are not considered as a mode converter element, only irregular stepped mode converters are investigated.

In [69], a SOM for designing TE_{10} to TE_{m0} (m is odd number) is offered. The technique uses irregular symmetrical H-plane step discontinuities and multi-resolution algorithm ([70]) to optimize lengths and widths of these steps. The offered structure of this mode converter is shown in Figure 3.2.

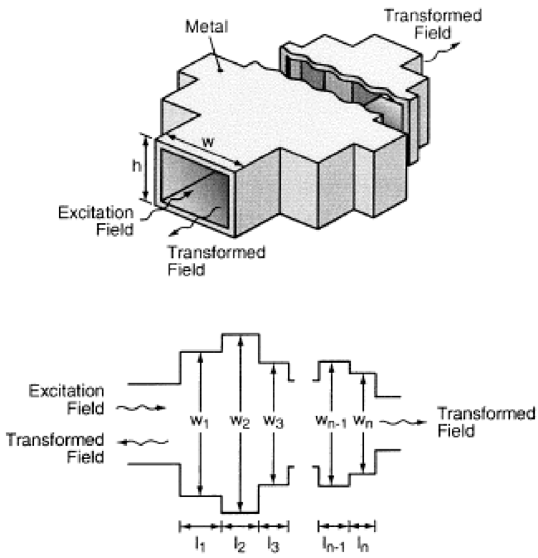

Figure 3.2: Offered irregular symmetrical H-plane stepped structure for designing TE_{10} to TE_{m0} (m is odd number) [69]

The structure shown in Figure 3.2 can be used for 4 different purposes, [69]. The first one is to convert the dominant TE_{10} mode to TE_{m0} (m is odd number). The second one is to convert TE_{10} mode to combinations of two modes (e.g. TE_{10} and TE_{30}). The third area of usage is to design phase shifter for TE_{10} mode. Finally, it can be used as mode selective reflector (e.g. when the combinations of TE_{10} and TE_{20} modes enters, it can reflect TE_{10} modes and let TE_{20} mode to pass).

Depending on the step size and optimization constraints, more than one converters can be obtained because the degree of freedom is large (one of them can have larger bandwidth). Therefore, the initial values of parameters determine which optimization solution will be reached [69]. The design starts with 5 steps [70] and this 5 stepped converter is optimized. If satisfactory result is obtained, each step section is divided into 2 subsections, so the resolution is increased further until desired performance is obtained. This from coarse to fine resolution increase optimization process is called multi-resolution algorithm [70]. This algorithm save time when there are large number of parameters. In this thesis, similar optimization procedure is applied to design irregular stepped mode converters. Design process starts with a 5-stepped mode converter, and if the result is not satisfactory, the number of steps increased as in the multi-resolution algorithm. If the result of the 5 stepped converter is satisfactory, design process ends. Optimization tools of CST Microwave Studio® software are used. The choice of optimization tool and how they are used in this thesis are mentioned in Appendix A.

3.1.1. General Design Guidelines for Discrete Stepped Mode Converters

- Input waveguide dimensions are chosen such that only TE_{10} mode exist at input port at the simulated frequency range
- Output waveguide dimensions are chosen such that the desired output waveguide mode exists at the output port with the minimum number of unwanted other waveguide modes
- Optimization process starts with 5 discrete waveguide steps (E-plane or H-plane steps, depending on desired output mode/mode combination)

- Initial dimensions of 5 discrete steps are set such that desired output mode could flow through these sections, in other words, the cut-off frequency of the output mode/mode combination is lower than operating frequency/frequency band.

- In the design procedure, desired mode converter can be obtained generally as follows:

    a. Input reflection coefficient of TE_{10} mode (S1(TE_{10}),1(TE_{10}) parameter) is set to be as low as possible

    b. S2(desired mode),1(TE_{10}) parameter shows how good is TE_{10} mode at the input port is converted to desire mode and in dB scale it is usually set to be 0 dB.

    c. S2(TE_{10}),1(TE_{10}) parameter shows proportionally how much of input TE_{10} mode reaches the output port without being converted into the desired mode. This is usually undesired, and this parameter is set to be as low as possible

    d. Additional some optimization goals are set to ensure appropriate mode combination ratio (amplitude) and combination phases if mode combination is desired at the output port.

- Dimensions of discrete steps are set as optimization parameters.

- If the design criteria are not reached after first optimization process, each discrete step is sub divided into 2 new steps, in other words, number of discrete steps are doubled, and the optimization process starts again. This cycle continues until the design criteria are reached. Increasing step number results in smoothing out S parameter and increasing the operating bandwidth so it may help to reach design criteria.

3.1.2. 5 Stepped TE_{10} to TE_{30} Converter

The structure shown in Figure 3.2 is proven to accomplish TE_{10} to TE_{m0} (m is odd number) conversion, this irregular symmetrical H-plane stepped structure is used. Input waveguide is connected to port 1 and output waveguide is connected to port 2. Dimensions of input waveguide are chosen as a = 24 mm & b = 12 mm. The cut-off frequency of the dominant TE_{10} mode in the input waveguide is 6.241 GHz with these dimensions and the second mode (TE_{01}) cut-off frequency is 12.41 GHz, so there is only TE_{10} mode in the input waveguide section between 8-12 GHz. Dimensions of the output waveguide are chosen as a = 50 mm & b = 12 mm to support TE_{30} mode and to have the minimum number of unwanted modes between 8-12 GHz. The lowest cut off frequency in the output waveguide is the cut-off frequency of the dominant TE_{10} mode with $f_{c_{10}} = 2.997$ GHz. The second mode is TE_{20} mode and its cutoff frequency is 5.986 GHz. The third mode and final mode in the output waveguide is TE_{30} and its cut-off frequency is 8.977 GHz. The initial width of all 5 steps are set to 80 mm and the initial length of all step sections are set to 20 mm. The height of all waveguide sections equal to 12 mm and it is not an optimization parameter. The optimization goal and their weights are set as follows:

- $S2(TE_{30}),1(TE_{10})$ = 0 dB at fc = 10 GHz, weight = 1.0
- $S2(TE_{10}),1(TE_{10})$ < -20 dB at fc = 10 GHz, weight = 1.0
- $S1(TE_{10}),1(TE_{10})$ < -20 dB at fc = 10 GHz, weight = 1.0

Figure 3.3 shows the initial (starting) model and Figure 3.4 shows the obtained 5 stepped mode converter from optimization process. The dimensions of final design are also shown in Figure 3.4. Figure 3.5 shows the S parameter result (in dB scale) of the obtained mode converter.

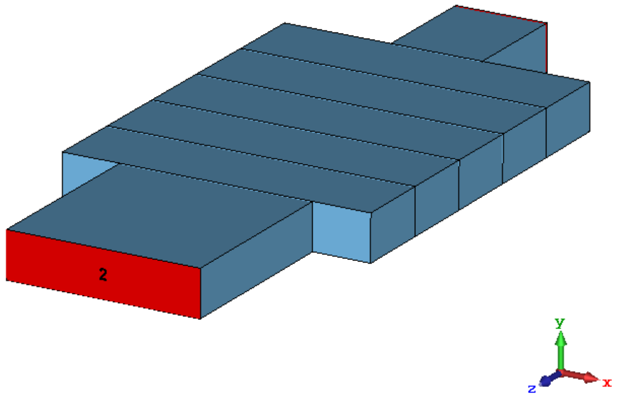

Figure 3.3: The initial (starting) model of 5 stepped TE_{10} to TE_{30} converter

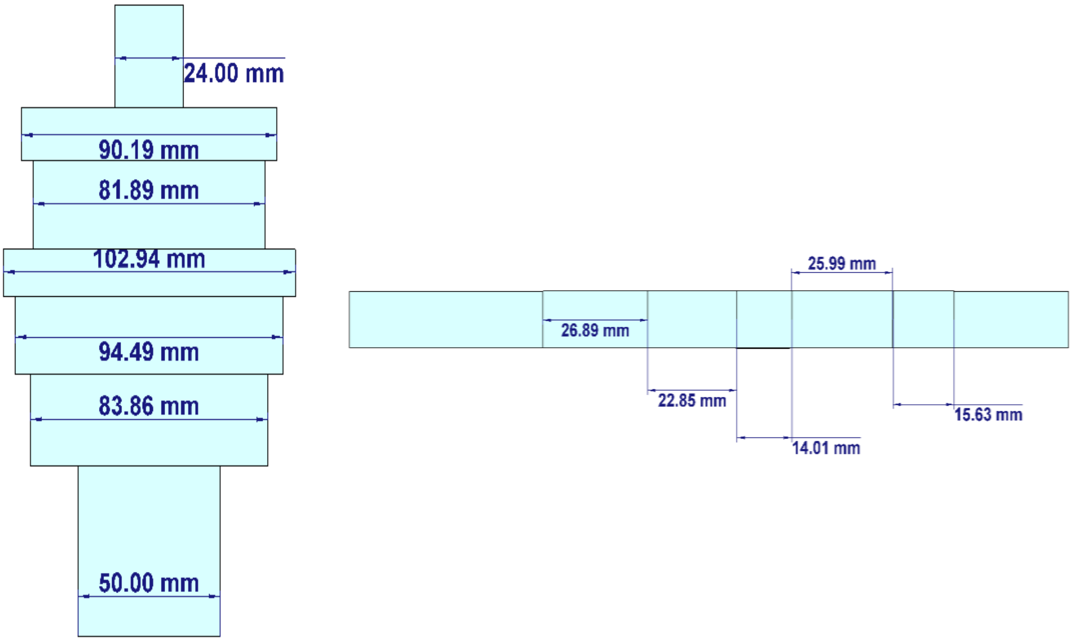

Figure 3.4: Designed 5 stepped TE_{10} to TE_{30} converter with its dimensions (left: top view, right: side view)

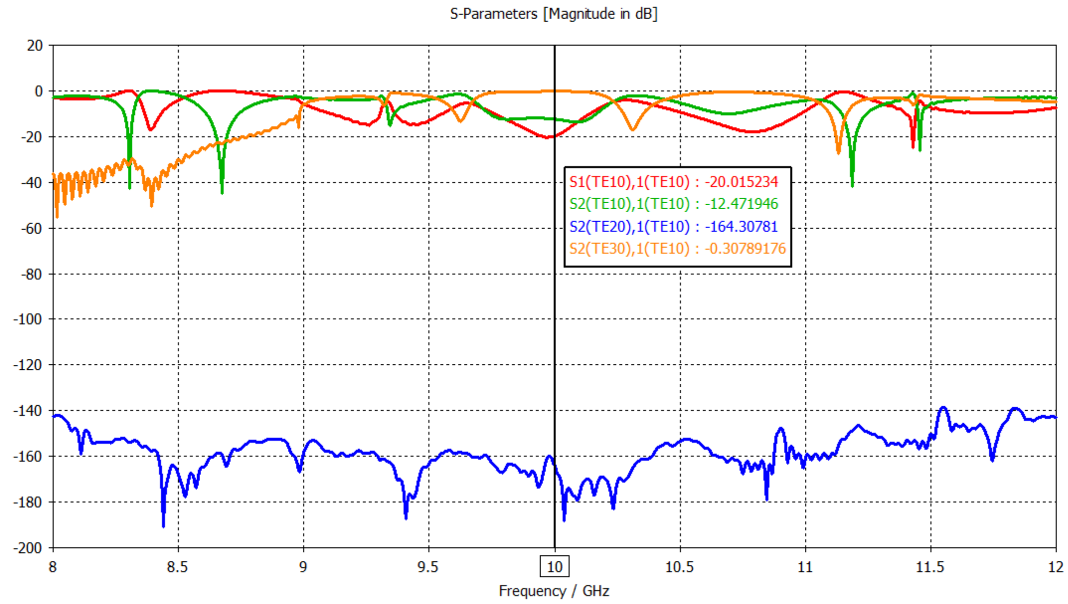

Figure 3.5: S parameter result of designed 5 stepped TE_{10} to TE_{30} converter

When Figure 3.5 is analyzed at 10 GHz, it can be seen that input reflection of TE_{10} mode is -20 dB, which means that almost all the energy is entered from input port (port 1) as TE_{10} mode. Only -12.47 dB of entered TE_{10} mode reach the output port (port 2) as TE_{10} mode. Almost all the energy entered as TE_{10} mode from input port is converted to TE_{30} mode at the output port with only -0.31 dB conversion loss. As said in [69], symmetrical H-plane stepped structures do not generate TE_{20} due to symmetry, one can see that there is no TE_{20} mode at the output port (-164.3 dB).

To illustrate mode conversion operation, the electric field monitor of CST Microwave Studio® software can be used. Figure 3.6 shows the electric field vectors inside the designed mode converter by using this feature, when TE_{10} mode enters from input port. As it can be seen in Figure 3.6, TE_{10} mode is converted to TE_{30} mode at the output of this converter.

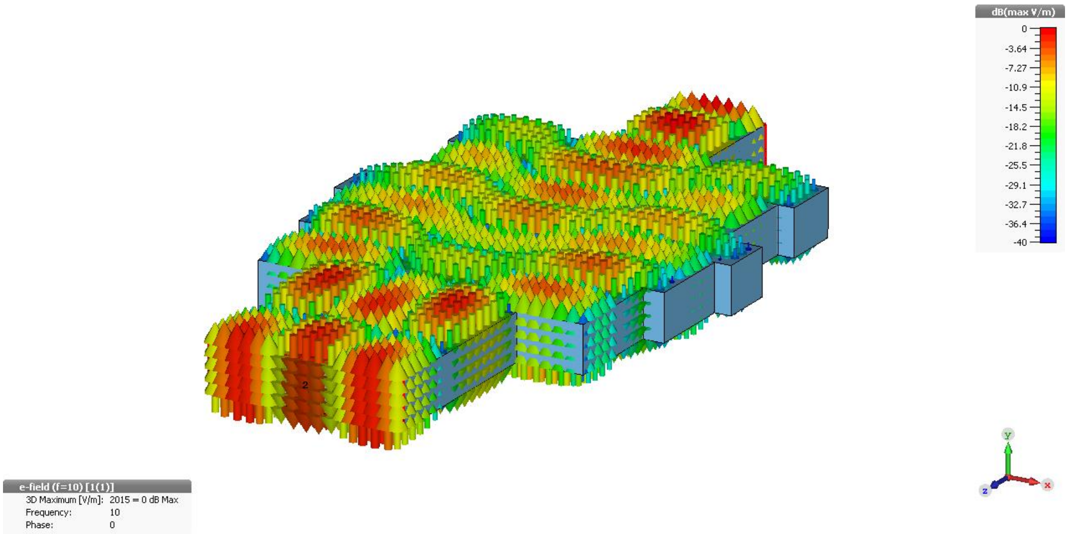

Figure 3.6: Electric field vectors inside designed 5 stepped TE_{10} to TE_{30} converter at 10 GHz

TE_{10} to TE_{30} mode conversion is obtained in approximately 3.51 wavelengths.

To see the effect of asymmetries of steps, which can be due to fabrication of such a waveguide mode converter geometry, step asymmetries with 1 mm value are introduced. When the H-plane steps are not symmetrical anymore, these steps can generate TE_{20} mode. Figure 3.7 shows S2(TE20),1(TE10) results with and without these introduced step asymmetries. Figure 3.8 shows S2(TE30),1(TE10) results with and without these introduced step asymmetries. If these two figures are examined, it can be see that 1 mm step asymmetries gave rise to TE_{20} mode at the output, but value of TE20 mode is still relatively small, as a result, value of TE_{30} mode at the output is not affected very much.

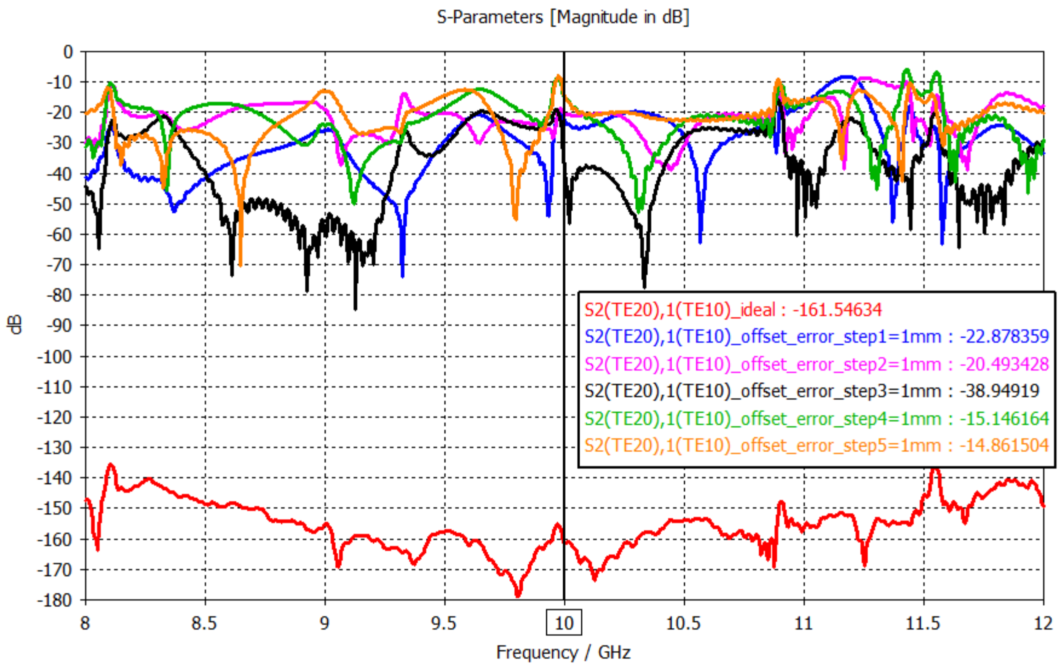

Figure 3.7: S2(TE20),1(TE10) results with and without 1 mm step asymmetries

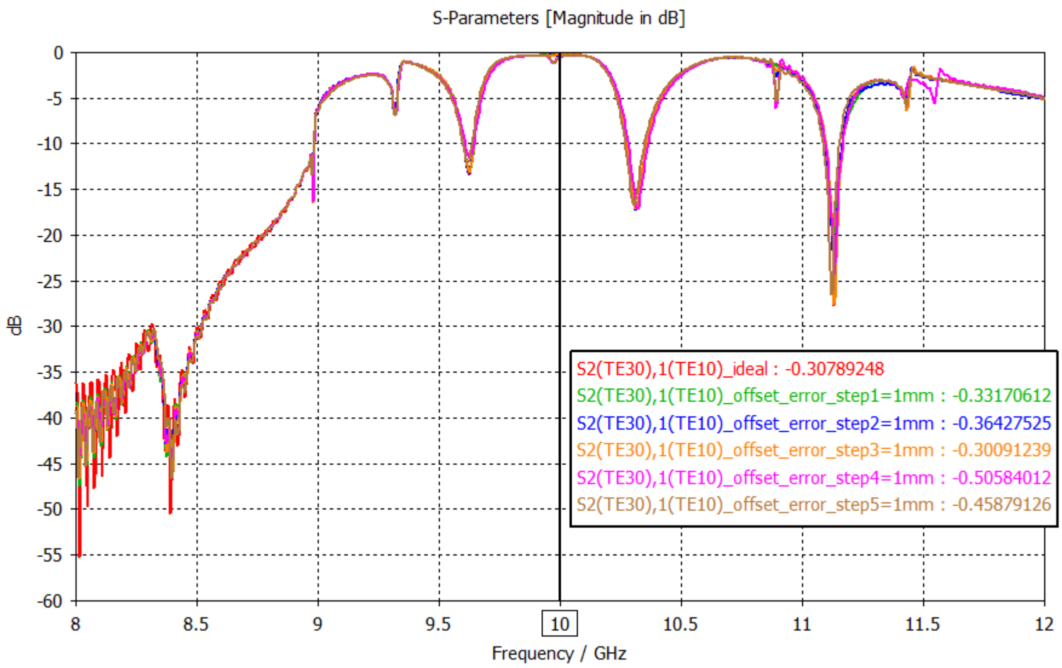

Figure 3.8: S2(TE30),1(TE10) results with and without 1 mm step asymmetries

3.1.3. 20 Stepped TE_{10} to TE_{30} Converter

To see the effect of increasing the number of steps of irregular symmetric H-plane stepped mode converters on conversion efficiency and bandwidth, 20 stepped TE_{10} to TE_{30} mode converter is designed. The input waveguide is connected to port 1 and the output waveguide is connected to port 2. Input waveguide dimensions are chosen as a = 22.9 mm & b = 10.16 mm to allow propagation of TE_{10} mode only between 9-11 GHz. The cut-off frequency of TE_{10} mode in input waveguide section is 6.543 GHz. Output waveguide dimensions are chosen as a = 52.7 mm & b = 10.16 mm to allow propagation of TE_{30} mode with minimum undesired modes in 9-11 GHz band. The cut-off frequency of TE_{30} mode in this output waveguide section is 8.52 GHz. In order to decrease number of parameters to be optimized, the lengths of all waveguide steps are set to 40 mm and they are not optimization parameter. The height of all waveguide sections equal to 10.16 mm. The initial widths of waveguide steps are set to 80 mm and initially only 5 steps are considered and same optimization goals in 3.1.2 are used. When the optimization of 5 step converter came to some maturity level, each step is divided into 2 sub steps of length 20 mm (10 steps total), and the optimization is re-started again from that point. When the optimization of 10 step converter came again to some maturity level, each step is divided into 2 sub steps of length 10 mm (20 steps total), and final optimization is started from that point. As a result, stepped TE_{10} to TE_{30} converter shown in Figure 3.9 is obtained. The widths of waveguide steps of obtained converter are also shown in Figure 3.9. The total length of mode conversion section is 200 mm (= 6.67 wavelengths). Figure 3.10 shows the S parameter result of designed mode converter.

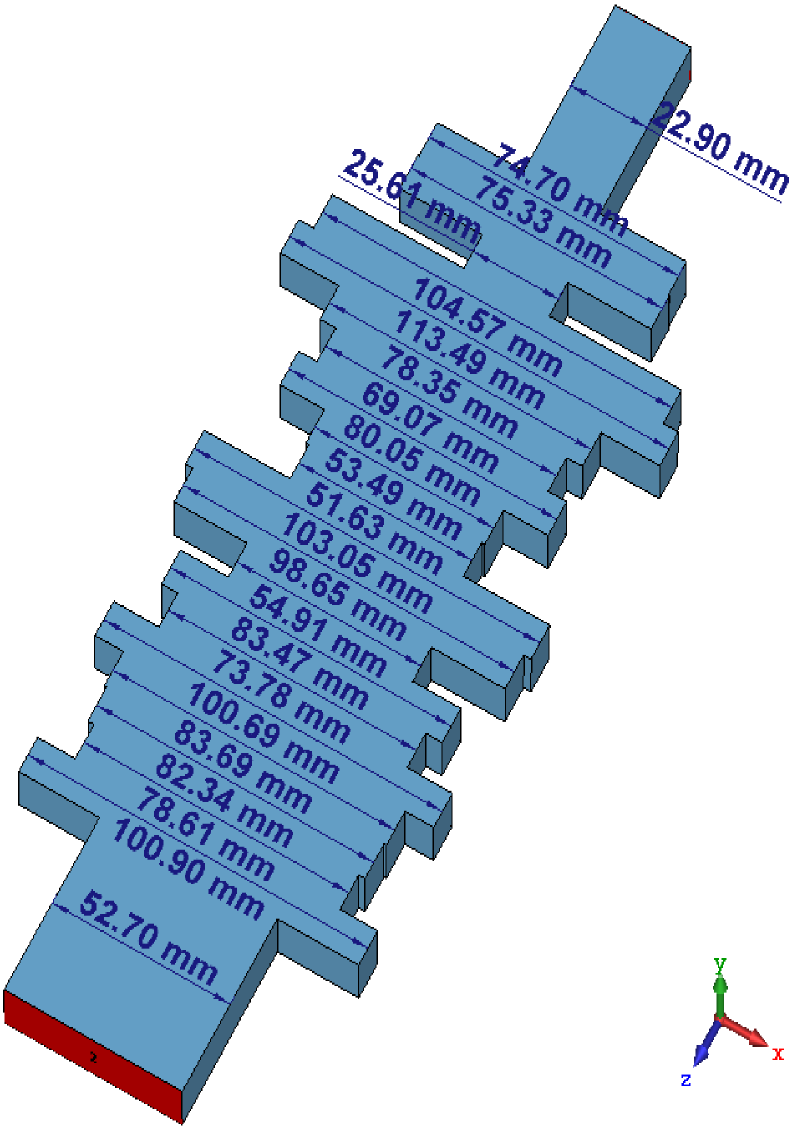

Figure 3.9: Designed 20 stepped TE_{10} to TE_{30} converter with its dimensions

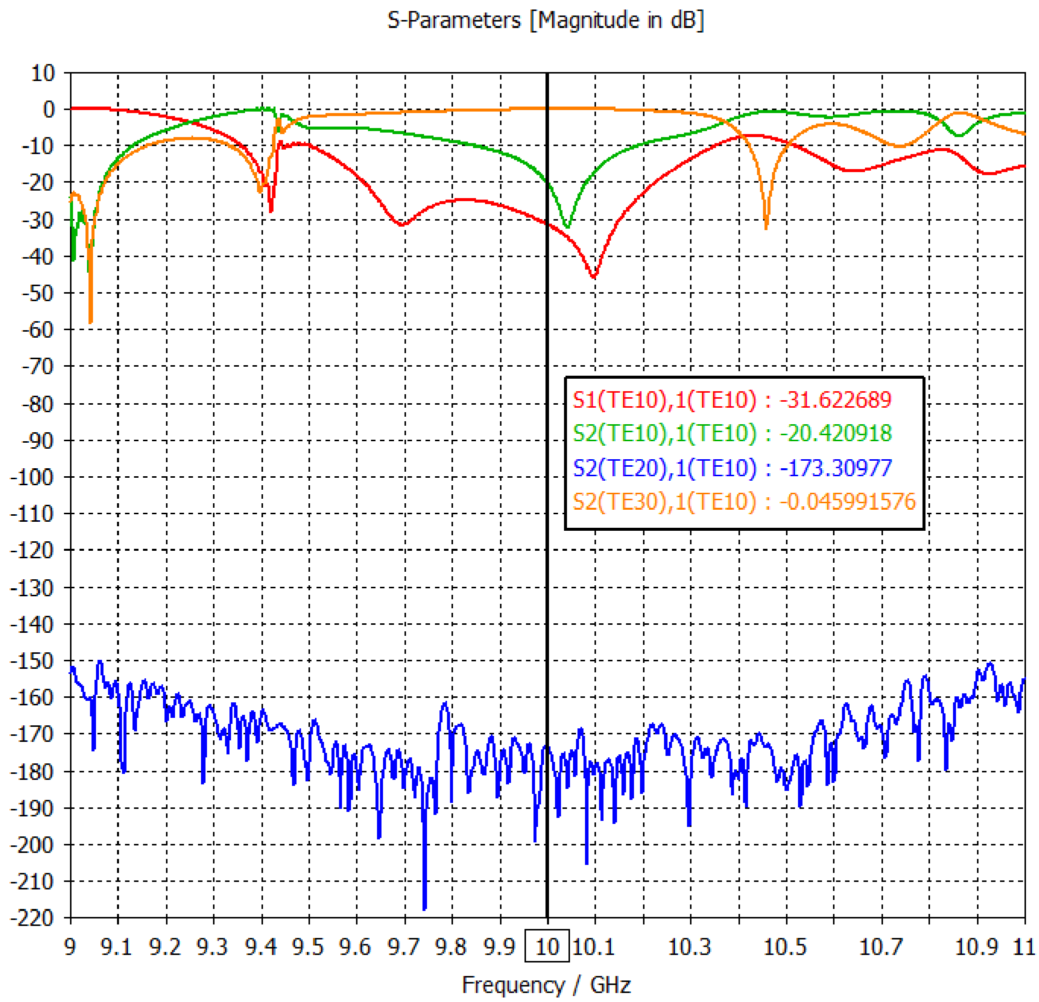

Figure 3.10: S parameter result of designed 20 stepped TE_{10} to TE_{30} converter

As it can be seen from Figure 3.10, the input reflection coefficient of TE_{10} mode at the input port (port 1) is very low at 10 GHz (-31.62 dB). Entered TE_{10} mode converted to TE_{30} mode at the output with only -0.046 dB conversion loss at 10 GHz. The TE_{10} mode content at the output port is very low at 10 GHz (-20.42 dB). Again, as it can be seen from Figure 3.10, these symmetrical steps cannot be used to generate TE_{20} mode at the output (below -150 dB between 9-11 GHz).

When Figure 3.10 is compared with Figure 3.5, it can be seen that mode conversion loss of 20 stepped mode converter is less than 5 stepped mode converter. In addition, mode conversion bandwidth of 20 stepped mode converter is wider than 5 stepped mode converter.

To illustrate how mode conversion is achieved inside this 20 stepped mode converter, Figure 3.11 shows the electric field vectors inside the mode converter when TE_{10} mode enters from input port. As it can be seen from output port in Figure 3.11, TE_{10} mode is successfully converted to TE_{30} mode.

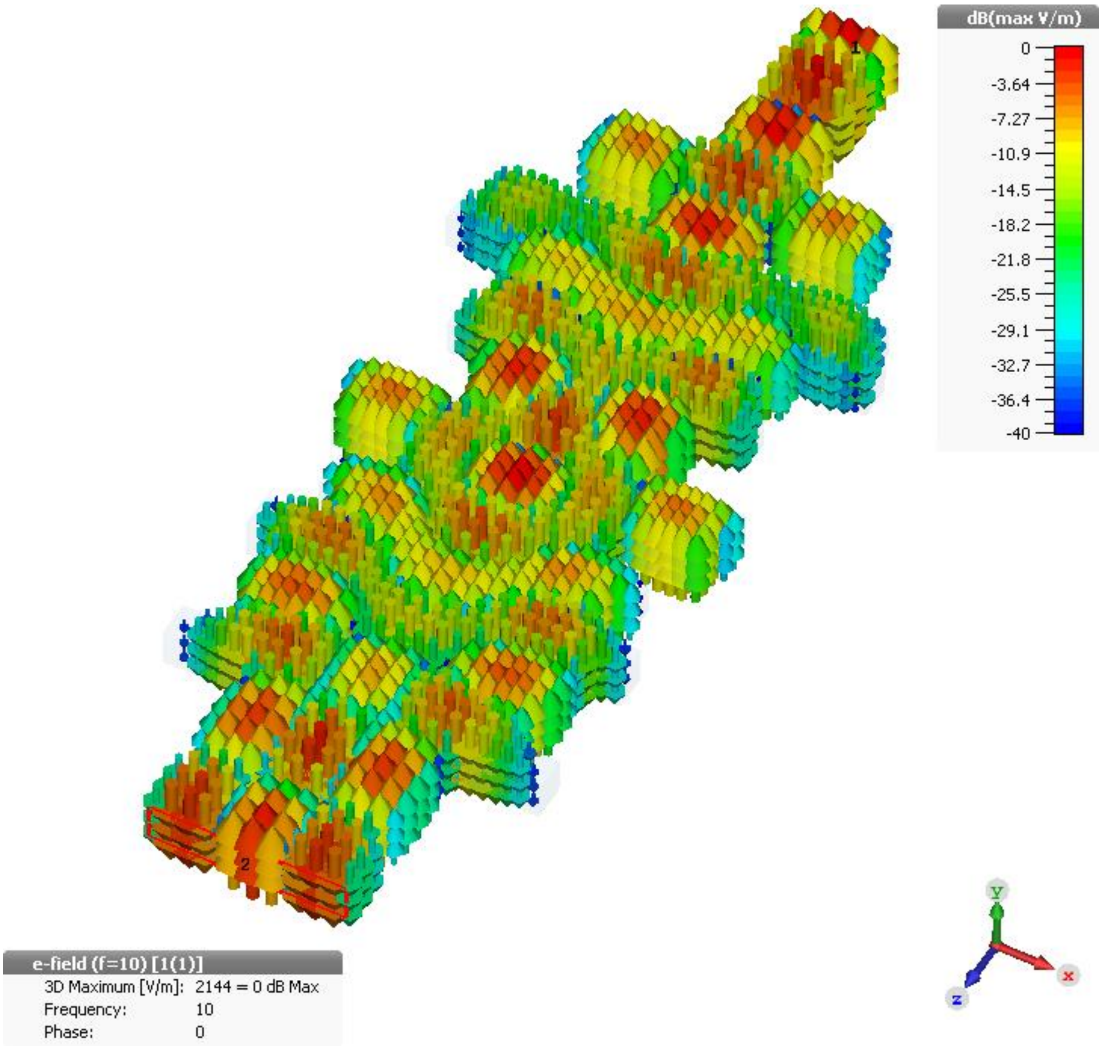

Figure 3.11: Electric field vectors inside designed 20 stepped TE_{10} to TE_{30} converter at 10 GHz

3.1.4. 5 Stepped TE_{10} to TE_{10}+TE_{30} Converter

In [69], it is shown that irregular symmetrical H-plane stepped converters can convert TE_{10} mode to combination of modes TE_{10}+TE_{30} modes. As mentioned in section 1.4, when the combination of TE_{10} and TE_{30} modes is carefully adjusted, TE_{30} mode can be used to cancel sidelobes of TE_{10} mode radiation pattern. Therefore, combination ratio of two modes can be anything depending on sidelobe position and level. However, in order to cancel side lobes, there should be 180 degree phase difference between two modes and the reason for this is shown in Figure 3.12.

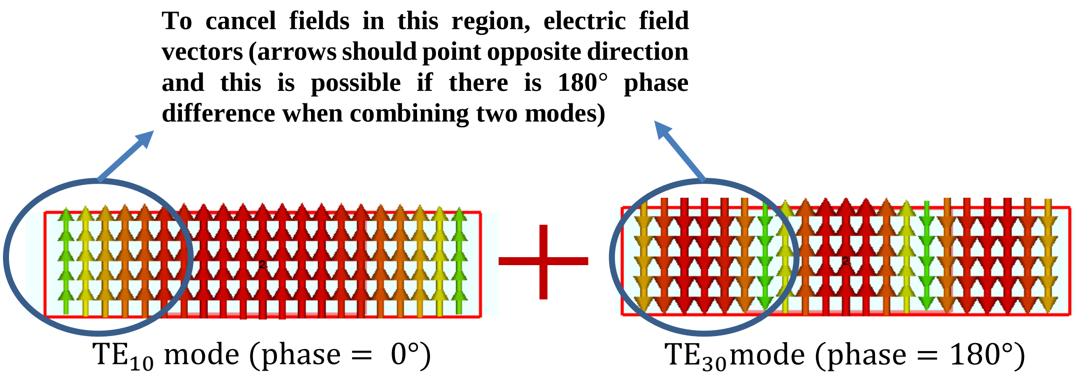

Figure 3.12: The reason for 180° phase difference when combining two modes

As a proof of concept, assume that we need to convert TE_{10} mode to TE_{10}+TE_{30} mode combination with equal ratios of TE_{10} and TE_{30} and with 180° phase difference. To achieve this, 5 stepped irregular symmetrical H-plane stepped mode converter is used. The input waveguide is connected to port 1 and its dimensions are set as a = 24 mm & b = 12 mm to allow propagation of only TE_{10} mode between 8-12 GHz. The output waveguide is connected to port 2 and its dimensions are set as a = 50 mm & b = 12 mm to allow propagation of both TE_{10} and TE_{30} modes with minimum number of undesired other modes. Initial widths of steps are set to 80 mm and their initial lengths are set to 20 mm. The heights of these steps are set to 12 mm (same height with input and output waveguides) and they are fixed parameters. The optimization goal and their weights are as follows:

- S2(TE_{30}),1(TE_{10}) = -3 dB at fc = 10 GHz, weight = 1
- S2(TE_{10}),1(TE_{10}) = -3 dB at fc = 10 GHz, weight = 1
- S1(TE_{10}),1(TE_{10}) = -20 dB at fc = 10 GHz, weight = 1

- Phase difference between TE_{10} and TE_{30} modes = 180° at fc = 10 GHz, weight = 0.1

Figure 3.13 shows the obtained 5 stepped mode converter after design process. Final value of widths and lengths of steps are also shown in Figure 3.13. As it can be seen from Figure 3.13, 2nd step width is almost equal to 1st step width and 5th step width almost equal to width of output waveguide. Therefore, it can be claimed that same performance can be obtained from 3 stepped mode converter and optimization goals for this mode converter were not challenging very much. If more challenging optimization goals are set, better performance can be obtained from this 5-stepped mode converter. However, as a proof of concept, these optimization goals are sufficient (optimum performance at fc = 10 GHz is sufficient for that purpose).

The total length of mode conversion section is 118.77 mm (= 3.96 wavelengths).

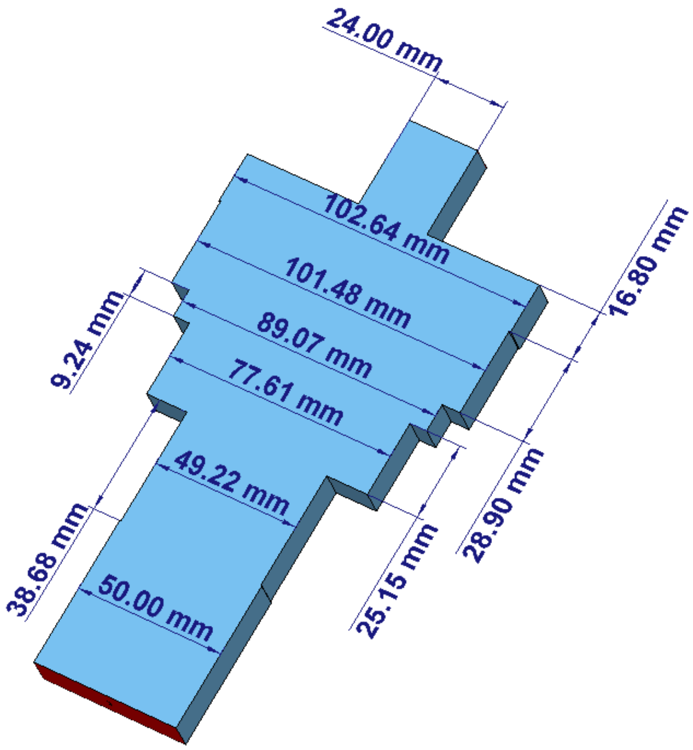

Figure 3.13: Designed 5 stepped TE_{10} to TE_{10}+TE_{30} converter

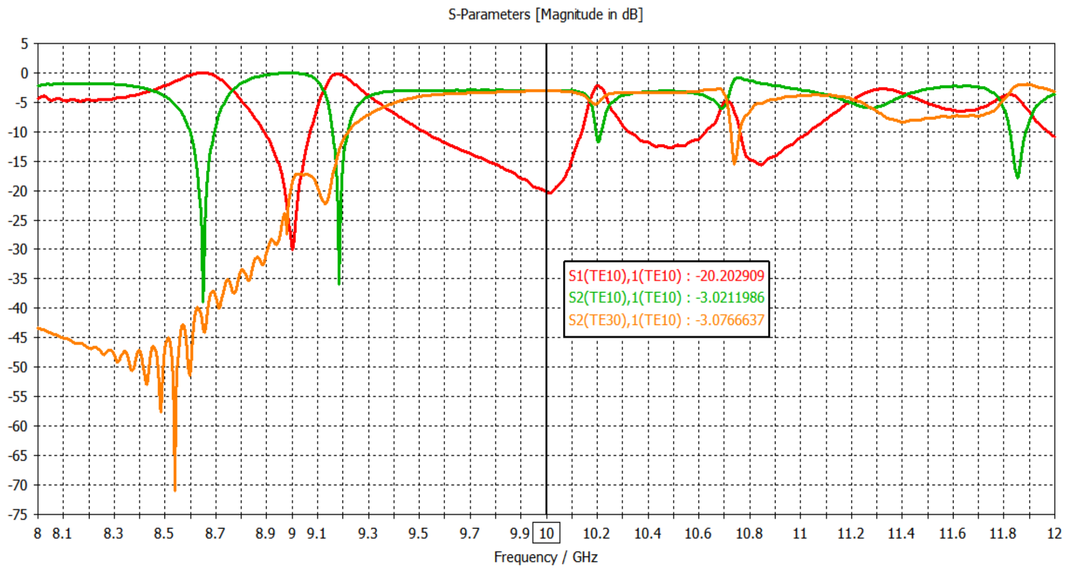

Figure 3.14: S parameter result of designed 5 stepped TE_{10} to TE_{10}+TE_{30} converter

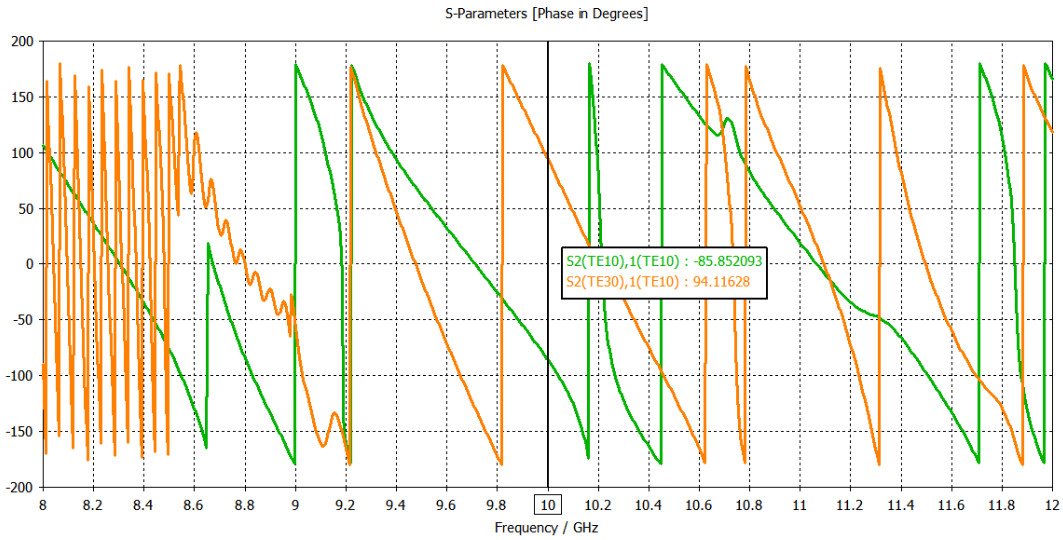

Figure 3.15: Phases of TE_{10} and TE_{30} modes at the output terminal

S parameter result of designed mode converter is given in Figure 3.14. As it can be seen from this figure, input reflection coefficient of TE_{10} mode is -20.21 dB at 10 GHz. All energy which entered as TE_{10} from input port is equally converted to TE_{10} and TE_{30} modes (S2(TE_{30}),1(TE_{10}) = -3.08 dB at 10 GHz, S2(TE_{10}),1(TE_{10}) = -3.02 dB at 10

GHz). S2(TE_{20}),1(TE_{10}) is below -200 dB between 8-12 GHz, so it is not shown here. Figure 3.15 shows the phases of S2(TE_{30}),1(TE_{10}) and S2(TE_{10}),1(TE_{10}). As it can be seen from Figure 3.15, there is 180° phase difference between S2(TE_{30}),1(TE_{10}) and S2(TE_{10}),1(TE_{10}) as desired.

To illustrate how mode conversion is achieved inside this 5-stepped mode converter and what the total electric field looks like, Figure 3.16 shows the electric field vectors inside the mode converter when TE_{10} mode enters from input port. As it can be seen from output port in Figure 3.16, TE_{10} mode is successfully converted to TE_{10} and TE_{30} mode combination.

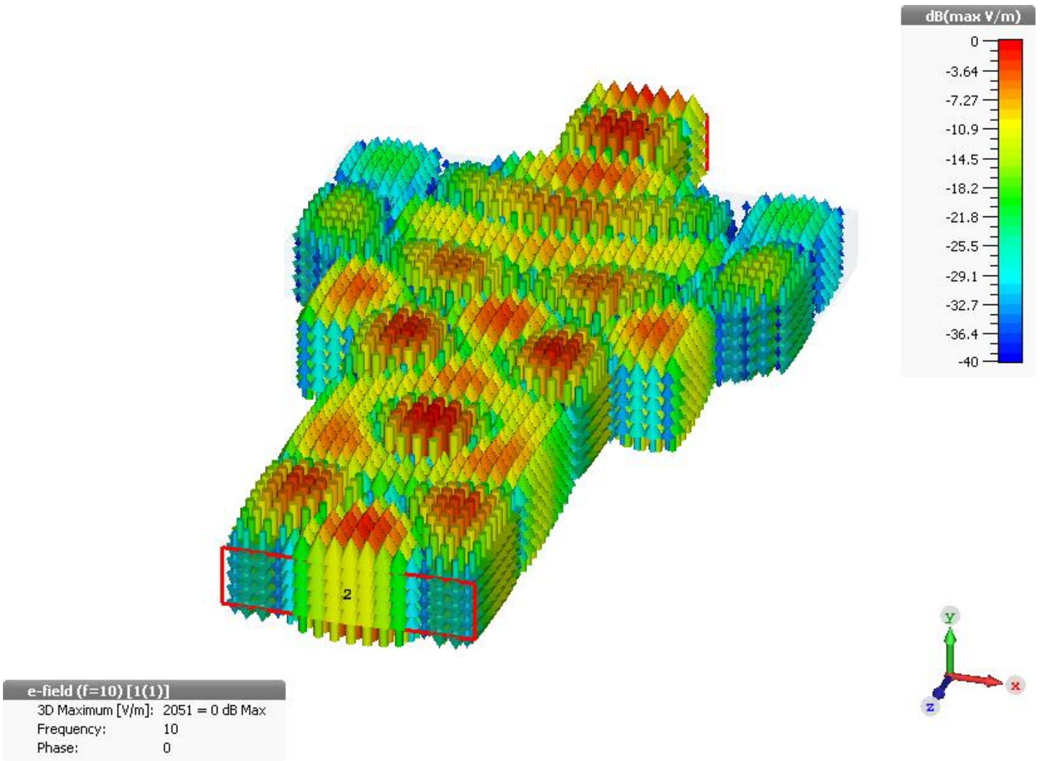

Figure 3.16: Electric field vectors inside designed 5 stepped TE_{10} to TE_{10}+TE_{30} converter at 10 GHz

3.1.5. 5 Stepped TE_{10} to TE_{20} Converter

The mode conversion from TE_{10} mode to TE_{20} mode cannot be done with irregular symmetrical H-plane stepped mode converters due to symmetry of structure, [69]. To achieve TE_{10} mode to TE_{20} mode conversion, irregular asymmetrical H-plane steps are investigated. Five irregular asymmetrical H-plane steps are used as building blocks of this TE_{10} to TE_{20} converter. Input waveguide is connected to port 1 and its dimensions are set as a = 22.86 mm & b = 10.16 mm to allow propagation of only TE_{10} mode between 9-11 GHz. Output waveguide is connected to port 2 and its dimensions are set as a = 35 mm & b = 10.16 mm to allow propagation of only TE_{10} and TE_{20} modes. The initial widths of waveguide steps are set to 60 mm and initial lengths are set to 20 mm. Offset parameters are introduced for each step, and initially they are set to 0 mm. Optimization goals and their weights are defined as follows:

- S2(TE_{20}),1(TE_{10}) > -0.05 dB at fc =10 GHz, weight = 3
- S1(TE_{10}),1(TE_{10}) < -20 dB at fc =10 GHz, weight = 1
- S2(TE_{10}),1(TE_{10}) < -20 dB at fc = 10 GHz, weight = 1

Figure 3.17 shows the designed TE_{10} to TE_{20} converter. The final values of parameters are given in Table 3.1. The total length of mode conversion section is 87.61 mm (= 2.92 wavelengths).

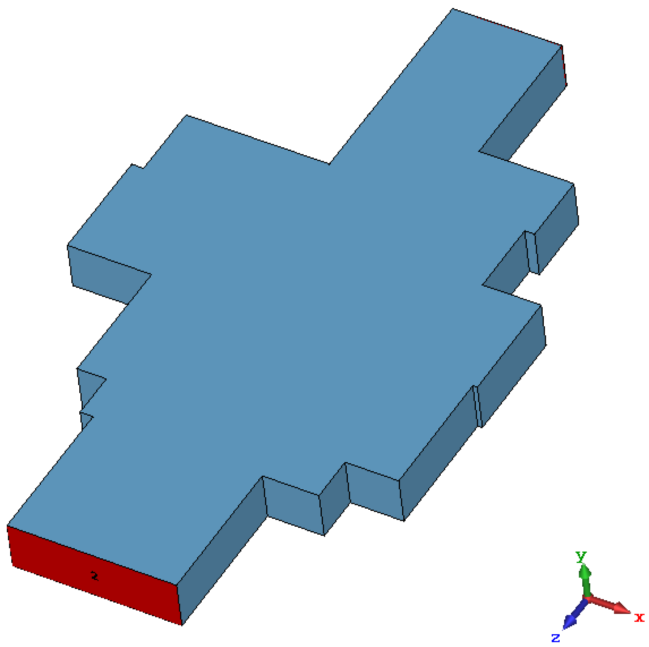

Figure 3.17: Designed 5 stepped TE_{10} to TE_{20} converter

Table 3.1: Final values of optimized parameters

Parameter name	Description of parameter	Value (~in mm)
a1	Width of 1st step	42.61
a2	Width of 2nd step	70.57
a3	Width of 3rd step	85.15
a4	Width of 4th step	66.55
a5	Width of 5th step	49.40
l1	Length of 1st step	14.22
l2	Length of 2nd step	15.10
l3	Length of 3rd step	22.83
l4	Length of 4th step	26.25
l5	Length of 5th step	9.20
trans1	Offset value of 1st step	9.82
trans2	Offset value of 2nd step	-6.21
trans3	Offset value of 3rd step	-1.38
trans4	Offset value of 4th step	6.97
trans5	Offset value of 5th step	4.50

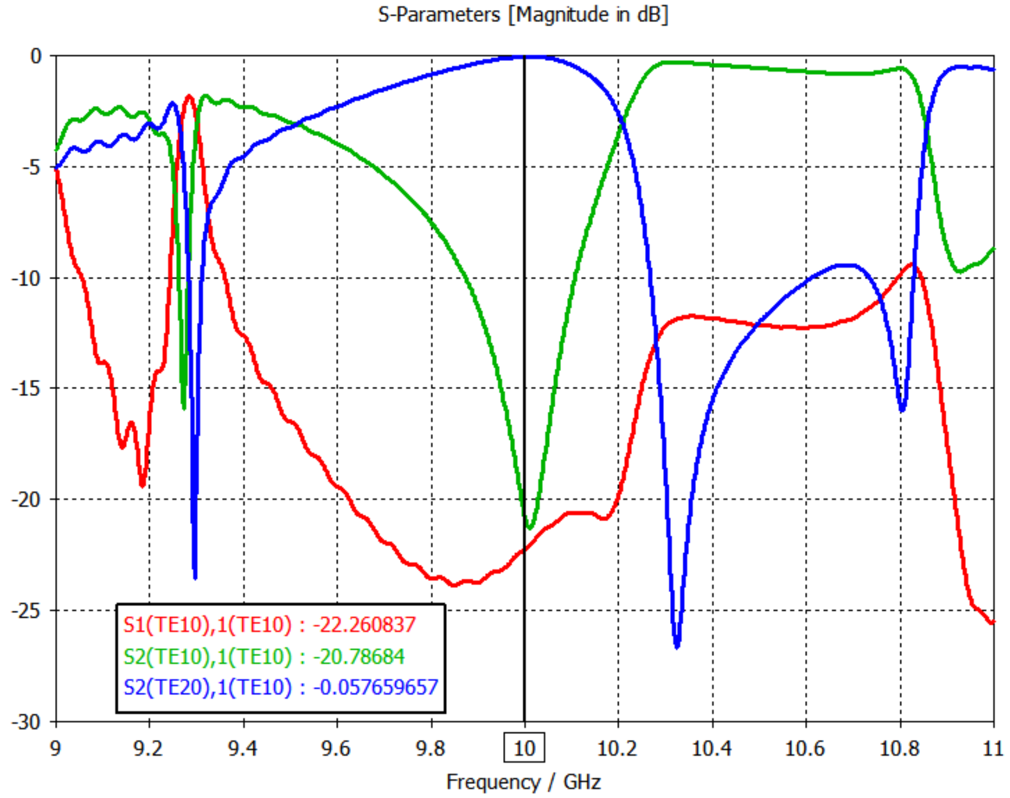

Figure 3.18: S parameter result of designed 5 stepped TE_{10} to TE_{20} converter

S parameter results are given in Figure 3.18. As it can be seen from Figure 3.18, the reflection coefficient of TE_{10} mode at the input port (port 1) is -22.26 dB at 10 GHz. TE_{10} mode entered from port 1 is converted into TE_{20} mode with very small conversion loss of -0.058 dB at 10 GHz. There is no TE_{10} at the output port (port 2) because $S2(TE_{10}),1(TE_{10})$ = -20.79 dB at 10 GHz.

When Figure 3.18 is examined, another important thing can be observed. When the frequency is 10.324 GHz, $S2(TE_{10}),1(TE_{10})$ = -0.3 dB, $S2(TE_{20}),1(TE_{10})$ = -26.66 dB and $S1(TE_{20}),1(TE_{10})$ = -11.89 dB. Therefore, at 10.324 GHz, the designed mode converter does not convert TE_{10} mode to TE_{20} mode, it passes TE_{10} mode to output port (port 2). This feature may be very useful depending on the application. In terms of monopulse feeds, if horn antenna is connected directly to this mode converter, at 10 GHz, TE_{20} mode is radiated and azimuth difference radiation pattern is obtained. At 10.324 GHz, TE_{10} mode is radiated and sum radiation pattern is obtained.

Figure 3.19 and Figure 3.20 show the electric field vectors inside this mode converter when TE_{10} enters from input port at 10 GHz and 10.324 GHz respectively. As it can also be seen from these two figures, at 10 GHz, TE_{20} mode is coming out of output port and TE_{10} mode is coming out of output port at 10.324 GHz.

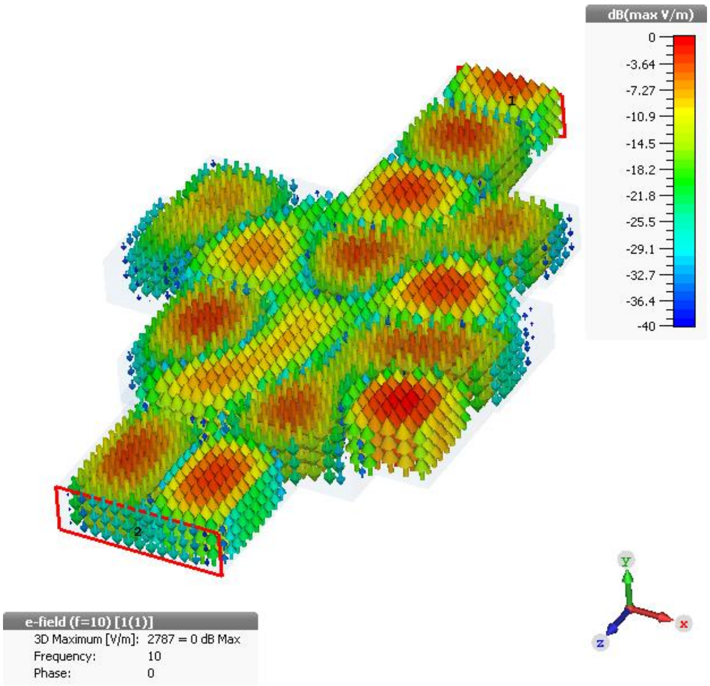

Figure 3.19: Electric field vectors inside designed 5 stepped TE_{10} to TE_{20} converter at 10 GHz

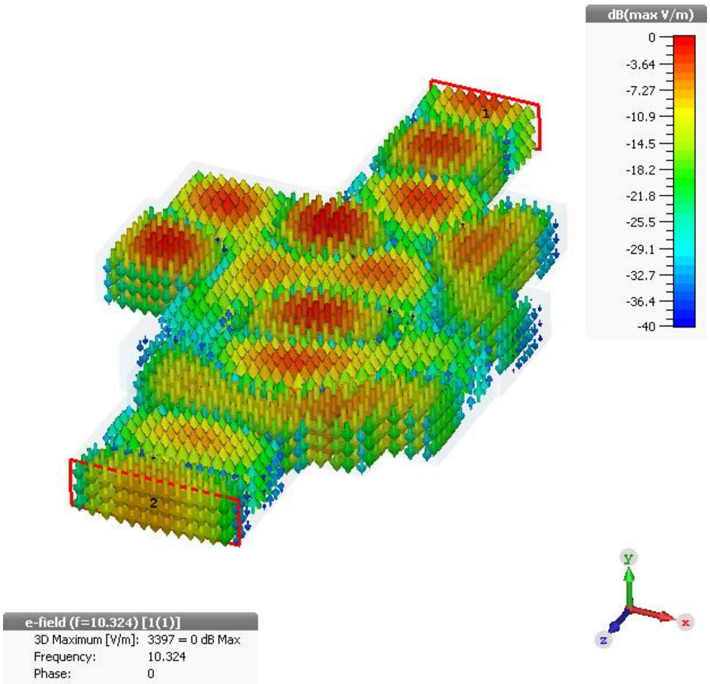

Figure 3.20: Electric field vectors inside designed 5 stepped TE_{10} to TE_{20} converter at 10.324 GHz

To check if this mode converter radiates sum radiation pattern at 10.324 GHz and azimuth difference radiation pattern at 10 GHz, the horn antenna is connected to output port of this mode converter. Figure 3.21 shows this structure, Figure 3.22 and Figure 3.23 shows the 3D radiation patterns in 10 GHz and 10.324 GHz respectively. As it can be seen from Figure 3.22 and Figure 3.23, this is really the case.

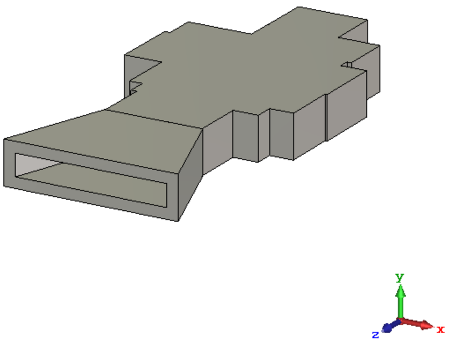

Figure 3.21: Horn antenna and designed 5 stepped TE_{10} to TE_{20} converter structure

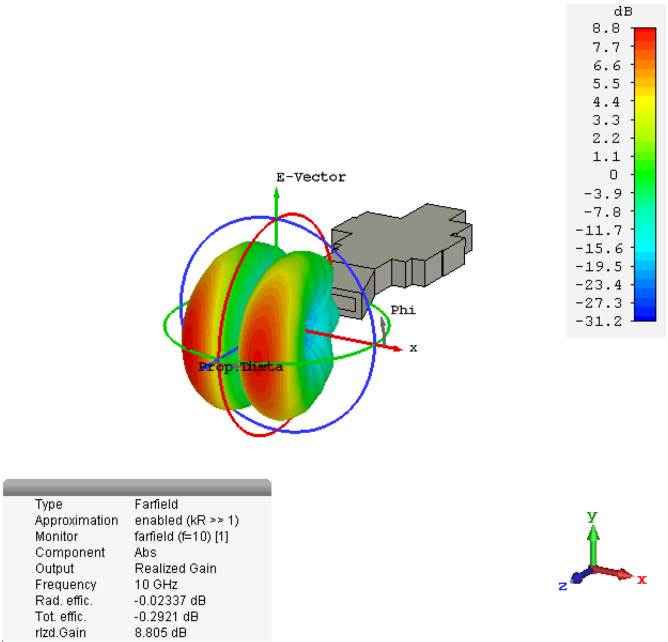

Figure 3.22: 3D radiation pattern at 10 GHz

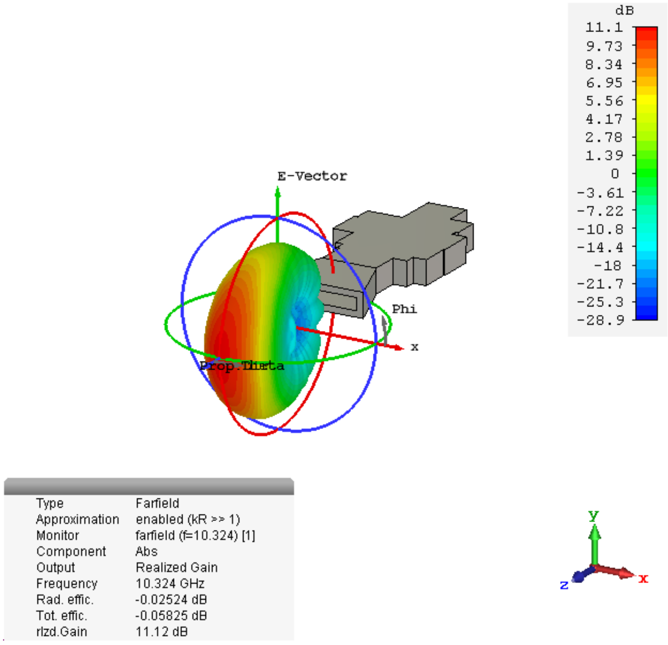

Figure 3.23: 3D radiation pattern at 10.324 GHz

3.1.6. 5 Stepped TE_{10} to TE_{11}+TM_{11} Converter

To excite TM_{11} and TE_{11} fields, waveguide height should be increased. Therefore, E-plane steps are investigated. Since symmetrical E-plane steps were not successful to generate these two modes in previous trials, asymmetrical E-plane steps are used. In order to create delta elevation pattern by combining these two modes, there should be particular magnitude ratio and phase differences between these two modes. This magnitude ratio and phase differences of two modes can be found by investigating these two modes in CST Microwave Studio®. Figure 3.24 shows the electric fields vectors of these two modes when their phases equal to 0° and the electric field vectors of desire combination to generate elevation difference radiation pattern. Figure 3.25 shows the magnitude of x component of electric fields of TE_{11} and TM_{11} modes.

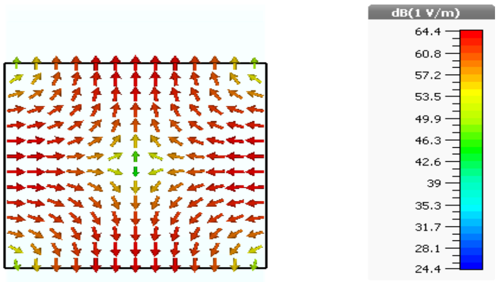

TE11 mode (0° phase)

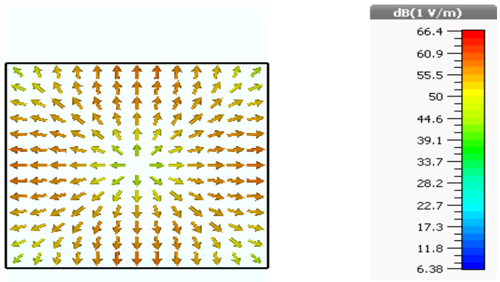

TM11 mode (0° phase)

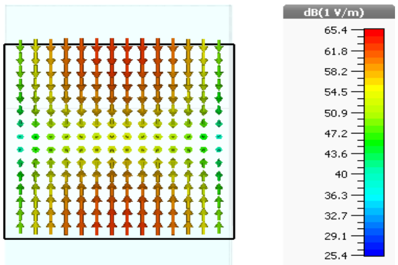

Desired mode combination (0° phase)

Figure 3.24: Electric field vectors of TE_{11} and TM_{11} modes and the desired mode combination

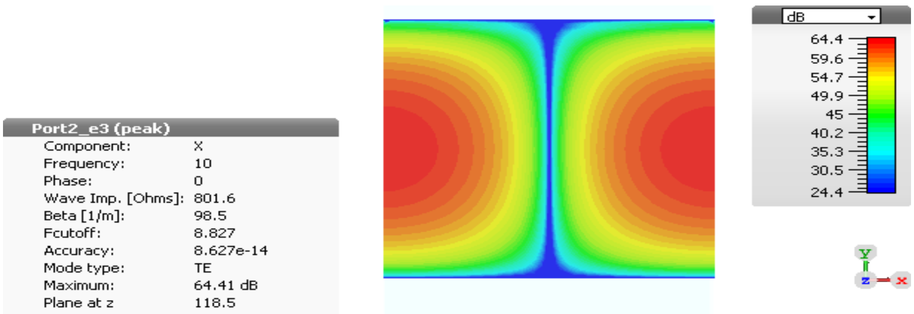

Magnitude of x component of TE_{11} mode electric field

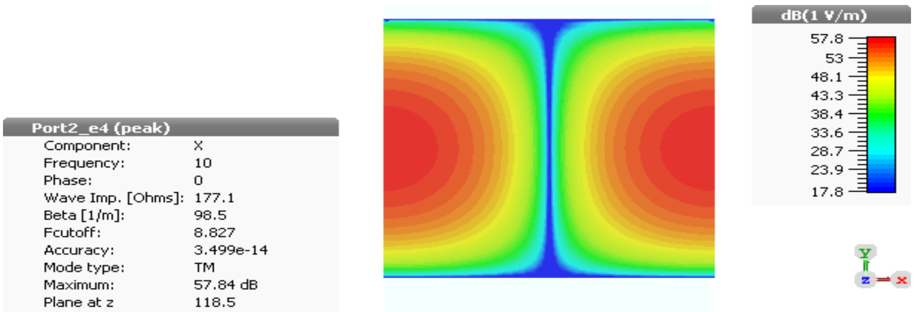

Magnitude of x component of TM_{11} mode electric field

Figure 3.25: Magnitudes of x component of TE_{11} and TM_{11} electric fields

To obtain desired mode combination shown in Figure 3.24, there should be only y and z components of electric field of desired mode combination and x component should be eliminated. Therefore, if we combine TE_{11} and TM_{11} modes with same phase, it seems possible. However, as it can be seen from Figure 3.25, x component of electric field of TE_{11} mode is 6.57 dB higher than x component of electric field of TM_{11} mode (64.41-57.84 = 6.57 dB), therefore in the desired combination, TM_{11} mode should be 6.57 dB higher than TE_{11} mode to eliminate x components of electric fields.

To design TE_{10} to TE_{11}+TM_{11} converter, 5 irregular asymmetrical E-plane steps are used. Input waveguide is a rectangular waveguide with dimensions a = 24 mm & b = 12 mm and it is connected to port 1. This waveguide section only allows propagation of TE_{10} mode between 9-11 GHz. Output waveguide is a square waveguide with dimensions a = 24 mm & b = 24 mm and it is connected to port 2. The reason of square waveguide choice is to support propagation of TE_{11} and TM_{11} modes with minimum additional undesired modes. Width of all waveguide steps are set to 24 mm and they are not optimization parameter. Initial lengths of waveguide steps are set to 20 mm. Initial heights of waveguide steps are set to 40 mm. Offset parameters for each waveguide steps and output waveguide section are introduced. Optimization goals and their weights are set as follows:

- $S1(TE_{10}),1(TE_{10}) < -15$ dB at fc = 10 GHz, weight = 1.0
- $S2(TE_{10}),1(TE_{10}) < -15$ dB at fc = 10 GHz, weight = 1.0
- $S2(TM_{11}),1(TE_{10}) – S2(TE_{11}),1(TE_{10}) = 6.57$ dB at fc = 10 GHz, weight = 1.0

After optimization process, the designed TE_{10} to TE_{11}+TM_{11} mode converter shown in Figure 3.26 is obtained. The final values of parameters are given in Table 3.2. The total length of mode conversion section is 78.51 mm (= 2.62 wavelengths).

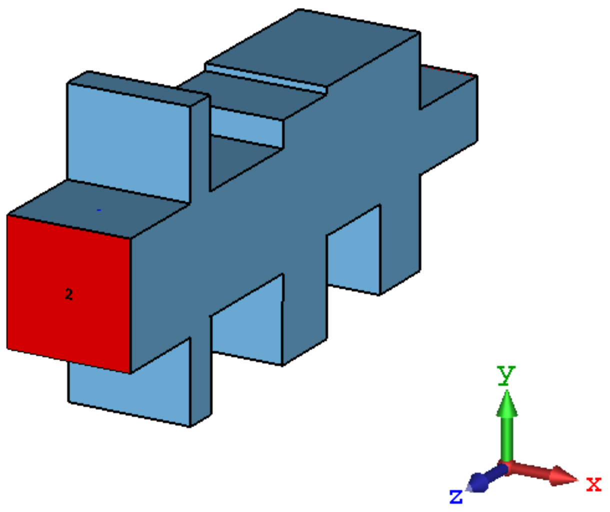

Figure 3.26: Designed 5 stepped TE_{10} to TE_{11}+TM_{11} converter

Table 3.2: Final values of optimized parameters

Parameter name	Description of parameter	Value (~in mm)
b1	Height of 1st step	43.73
b2	Height of 2nd step	27.02
b3	Height of 3rd step	44.35
b4	Height of 4th step	22.49
b5	Height of 5th step	57.44
l1	Length of 1st step	13.97
l2	Length of 2nd step	18.28
l3	Length of 3rd step	15.11
l4	Length of 4th step	24.41
l5	Length of 5th step	6.73
trans1	Offset value of 1st step	-1.74
trans2	Offset value of 2nd step	6.53
trans3	Offset value of 3rd step	-3.53
trans4	Offset value of 4th step	2.24
trans5	Offset value of 5th step	1.98
trans_out	Offset value of output waveguide	1.36

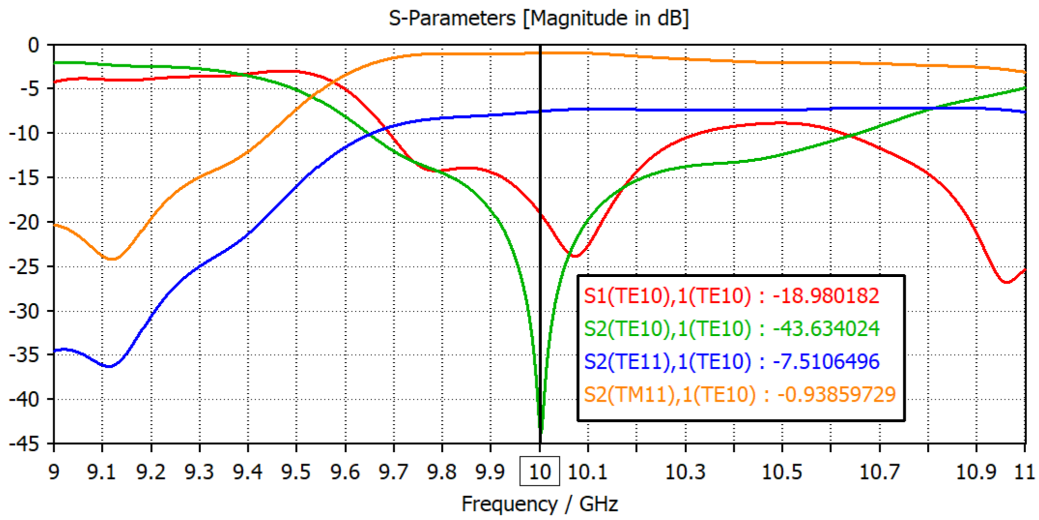

Figure 3.27: S parameter result of designed 5 stepped TE_{10} to TE_{11}+TM_{11} converter

S parameter results are given in Figure 3.27. Input reflection coefficient of TE_{11} mode is -18.98 dB at 10 GHz. There is no TE_{10} mode at the output port (port 2) at 10 GHz (S2(TE10),1(TE10) = -43.63 dB at 10 GHz). TE_{20} mode is not generated by this converter, its value is below -165 dB between 9-11 GHz (not shown in Figure 3.27). TM_{11} mode content at port 2 is -0.94 dB at 10 GHz and TE_{11} mode content at port 2 is -7.51 dB at 10 GHz. As it can be seen in Figure 3.27, difference between S2(TM_{11}),1(TE_{10}) and S2(TE_{11}),1(TE_{10}) is 6.57 dB at 10 GHz as desired. Figure 3.28 shows this difference between 9-11 GHz.

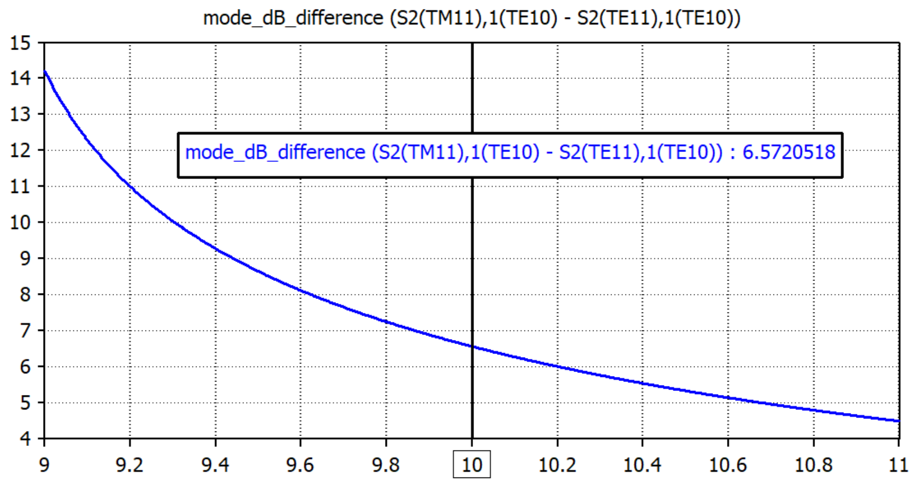

Figure 3.28: S2,1 difference of TM_{11} and TE_{11} modes

To see how mode conversion is realized within this structure and to check if the electric field vectors at the output port are as desired, electric field monitor (a feature of CST Microwave Studio® software) is placed at 10 GHz. Figure 3.29 shows the result of this monitor. As it can be seen from Figure 3.29, at the output port, desired mode combination (shown in Figure 3.24) is obtained and there is no x component of electric fields.

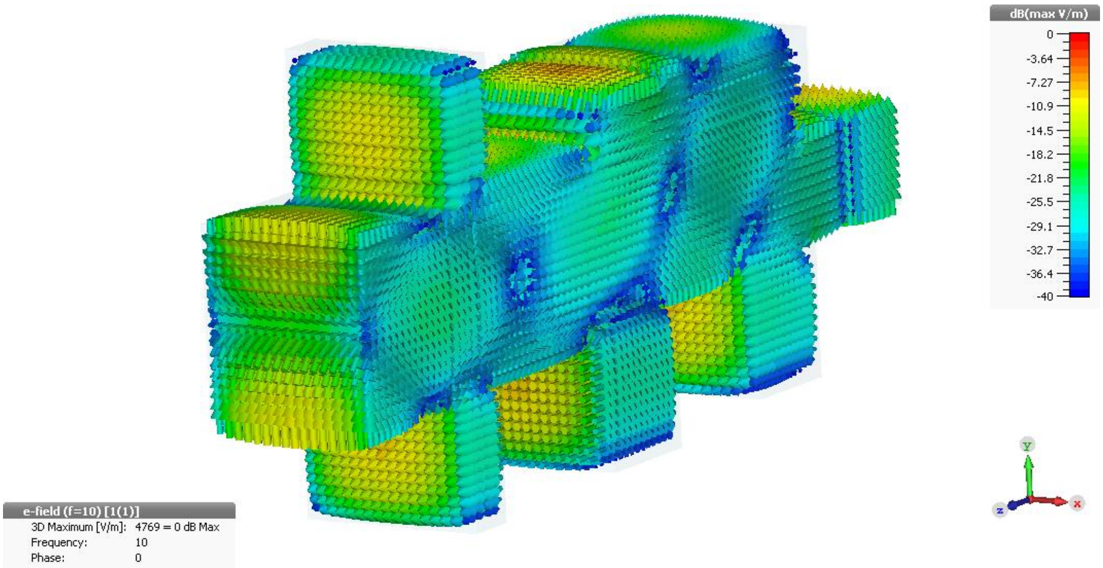

Figure 3.29: Electric field vectors inside designed 5 stepped TE_{10} to TE_{11}+TM_{11} converter at 10 GHz

To compare dispersion effect of this type of waveguide structure with the dispersion effect of normal (regular) waveguide section, group delays of TE_{11} and TM_{11} modes in both cases are plotted in Figure 3.30. Although this comparison is done for only TE_{10} to TE_{11}+TM_{11} mode converter type (to save space), similar type of behavior is also valid for other irregular (aperiodic, discrete) stepped mode converters given in this thesis. As it can be seen from Figure 3.30, in terms of dispersion, discrete stepped mode converters can be problematic, and this effect should also be considered when commenting on operating bandwidth.

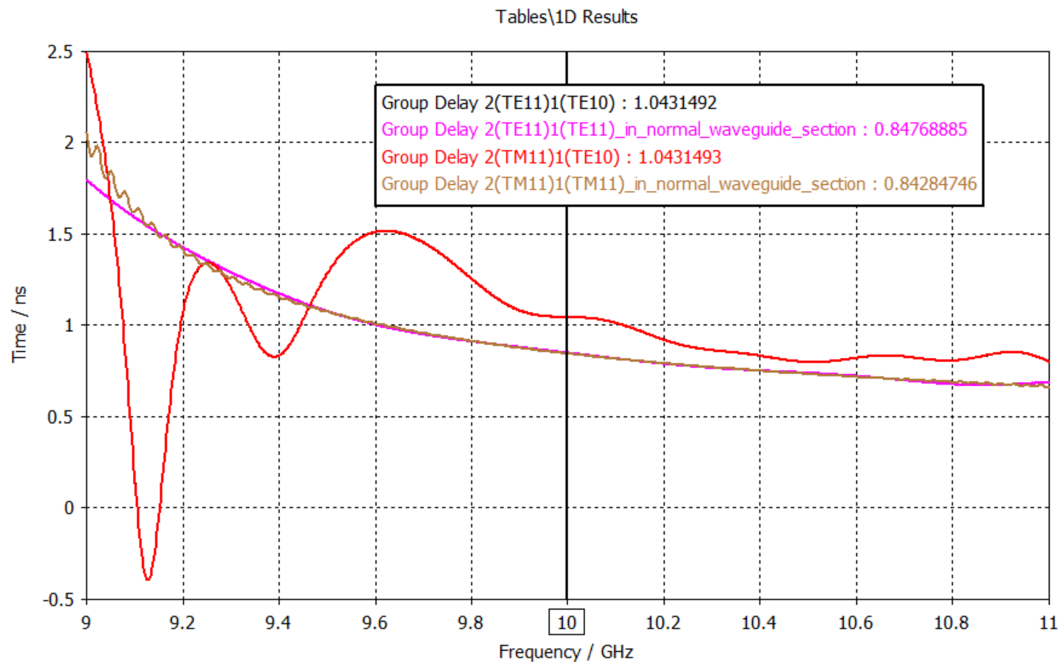

Figure 3.30: Comparison of group delays of TE_{11} and TM_{11} modes in 5 stepped TE_{10} to TE_{11}+TM_{11} mode converter and in normal waveguide section (a=b=24 mm, l= 118.5 mm)

3.2. Waveguide Bend Mode Converters

In oversized rectangular waveguide, waveguide bends in E or H plane can convert some percentage of dominant TE_{10} mode to other modes, [71] & [72]. There are extensive work done for the formulation of the solution of waves in such a region and their network parameters (circuit models), and some of them are given in [73], [74], [75], [76], [77], [78], [79], [80], [81], [82], [83], [84], [43]. In this thesis, CST Microwave Studio® 3D electromagnetic analysis software is used for the solutions of waveguide problems, therefore the information in above references is not used.

In [71] & [72], it is said that TE_{10} mode can couple into TE_{20} when H-plane bend is used and TE_{10} mode can couple into TE_{11}+TM_{11} degenerate mode pair when E-plane bend is used. Therefore, in this thesis, TE_{10} to TE_{20} waveguide bend mode converter uses H-plane bends and TE_{10} to TE_{11}+TM_{11} waveguide bend mode converter uses E-plane bends.

3.2.1. TE_{10} to TE_{20} Waveguide Bend Mode Converter

This type of mode converter is previously investigated in [85]. It uses double or triple cascaded H-plane bends to convert TE_{10} mode into TE_{20} mode. The formulations of these types of H-plane bend TE_{10} to TE_{20} mode converters are also given in this paper. The structures that are investigated in [85] are shown in Figure 3.31 and Figure 3.32.

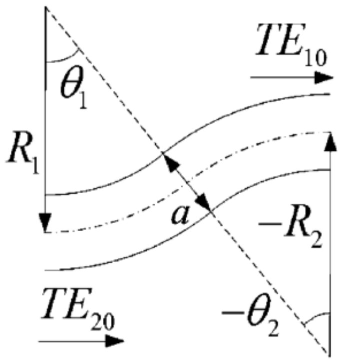

Figure 3.31: Geometry of double bend TE_{10}-TE_{20} mode converter (top view) [85]

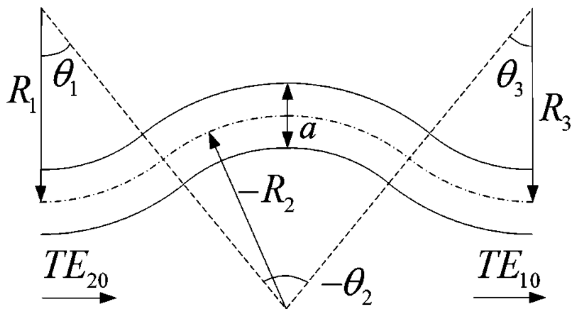

Figure 3.32: Geometry of triple bend TE_{10}-TE_{20} mode converter (top view) [85]

The design process for TE_{10}-TE_{20} mode converter started with one H-plane bend. The dimensions of waveguide are set to a = 40.42 mm & b = 18.83 mm to allow propagation of only TE_{10} and TE_{20} modes. Only R and θ parameters are the optimization parameters. After optimization process of one H-plane bend, it is seen that only one H-plane bend is not sufficient to fully convert TE_{10} mode to TE_{20} mode. Therefore, double H-plane bend structure shown in Figure 3.31 is used. By setting

$R_1=R_2$ and $\theta_1=\theta_2$, there is only two optimization parameters, R and θ. It is done, and after simple optimization process, TE_{10}-TE_{20} mode converter shown in Figure 3.33 is obtained. Since the structure in Figure 3.33 is a symmetrical structure, input or output waveguide can be either port 1 or port 2. To eliminate this, input port (port 1) of the structure is tapered down in E and H planes to a = 22.86 mm & b = 10.16 mm so that only TE_{10} mode can enter from port 1 (input side). This final design is shown in Figure 3.34 with its dimensions.

The optimization goals were as follows:

- $S1(TE_{10}),1(TE_{10})$ < -20 dB at fc = 10 GHz, weight = 1
- $S2(TE_{10}),1(TE_{10})$ < -20 dB at fc = 10 GHz, weight = 1
- Move min of $S2(TE_{10}),1(TE_{10})$ to fc = 10 GHz, weight = 1
- $S2(TE_{20}),1(TE_{10})$ = 0 dB at fc = 10 GHz, weight = 5

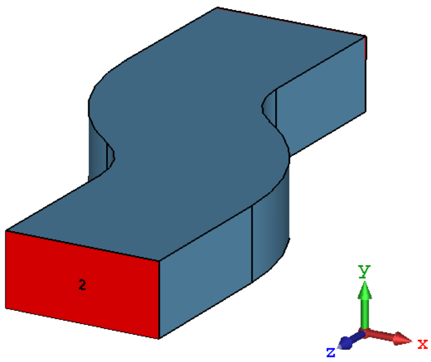

Figure 3.33: Designed TE_{10}-TE_{20} double H-plane bend mode converter

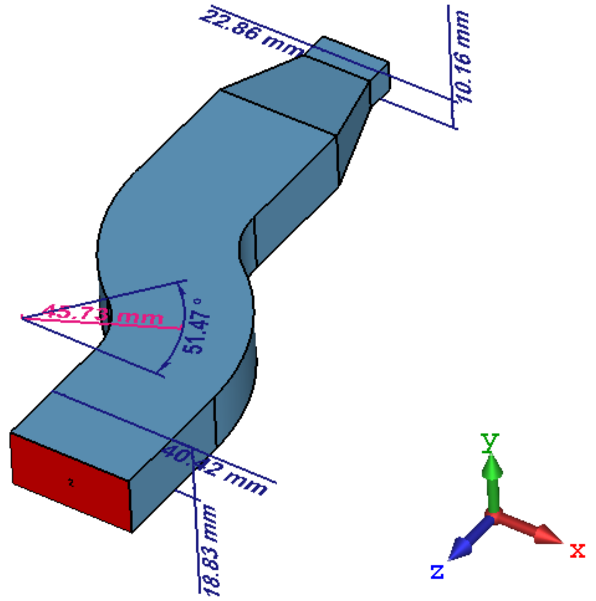

Figure 3.34: Final design of TE_{10}-TE_{20} double H-plane bend mode converter

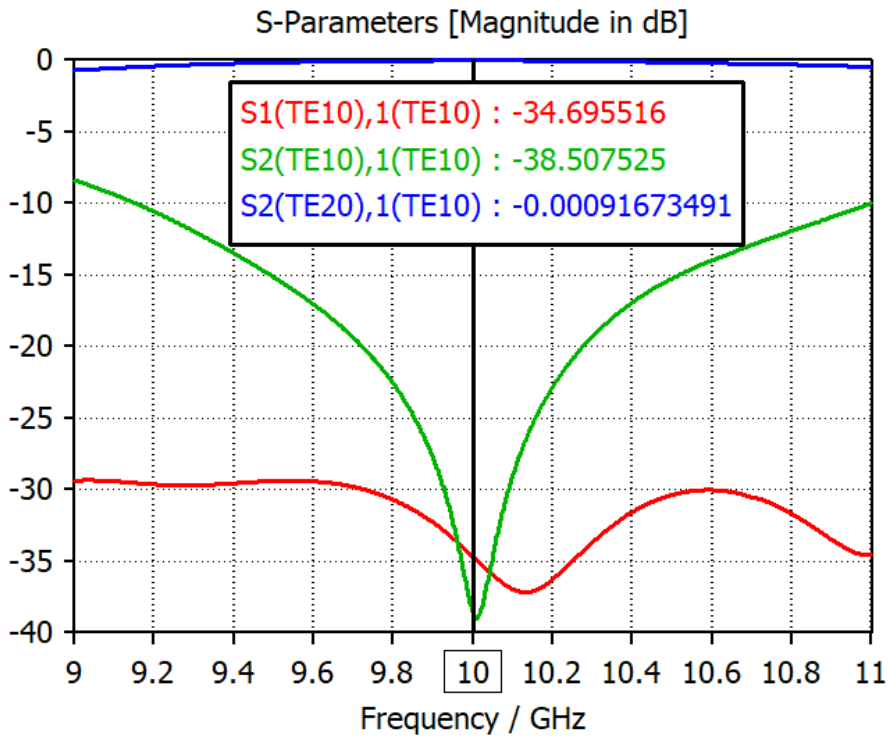

Figure 3.35: S parameter result of designed TE_{10} to TE_{20} converter

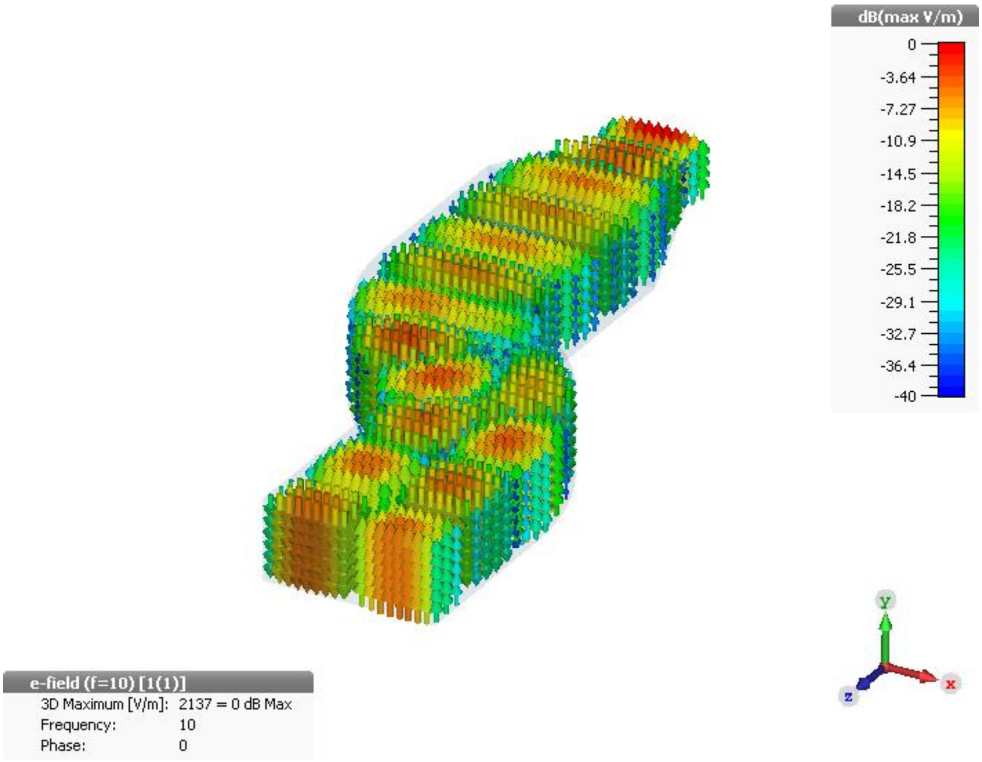

Figure 3.36: Electric field vectors inside designed TE_{10} to TE_{20} converter at 10 GHz

Figure 3.35 shows the S parameter results of final TE_{10}-TE_{20} mode converter design. As it can be seen from Figure 3.35, input reflection coefficient of TE_{10} mode is almost less than -30 dB between 9-11 GHz. There is no TE_{10} mode at the output port (port 2) at 10 GHz, S2(TE_{10}),1(TE_{10}) = -38.51 dB at 10 GHz. All energy of TE_{10} mode entered from input port (port 1) is converted into TE_{20} mode with -0.0009 dB conversion loss.

If S parameter response and behavior of this converter is compared with S parameter responses of the previous discrete stepped mode converters, it can be said that waveguide bend mode converter is more suitable for wideband applications. In addition, S parameters of bend mode converter is well-behaved (no sharp changes, it seems less resonant). These results are expected because this bend mode converter can be thought as formed by infinite number of discrete steps with same width and infinitesimal lengths. Please note that when the number of steps is increased similar behavior of S parameter is also observed when discrete stepped mode converters are designed (e.g. compare the S parameter responses in Figure 3.5 and Figure 3.10).

Figure 3.36 shows the electric field vectors as arrows when TE_{10} mode enters from input port at 10 GHz. As it can be seen from Figure 3.36, at the output port there is TE_{20} mode only.

3.2.2. TE_{10} to TE_{11}+TM_{11} Waveguide Bend Mode Converter

To design TE_{10} to TE_{11}+TM_{11} waveguide bend mode converter, 2 cascaded E-plane bends are used. The structure is similar to the one in Figure 3.31, but this time, bends are E-plane bends. Combination ratio of TM_{11} and TE_{11} modes is same as in section 3.1.6. In mode conversion section, the square waveguide with dimensions a = b = 24 mm is used to only allow propagation of TE_{10}, TE_{01}, TM_{11} and TE_{11} modes between 9-11 GHz. There are only two optimization parameters: R and θ (radius of bend and angle of bend). Optimization goals and their weights are set as follows:

- $S1(TE_{10}),1(TE_{10}) < -20$ dB at fc = 10 GHz, weight = 1
- $S2(TE_{10}),1(TE_{10}) < -20$ dB at fc = 10 GHz, weight = 1
- $S2(TE_{01}),1(TE_{10}) < -20$ dB at fc = 10 GHz, weight = 1
- $S2(TM_{11}),1(TE_{10}) – S2(TE_{11}),1(TE_{10}) = 6.57$ dB at fc = 10 GHz, weight = 1

The designed TE_{10} to TE_{11}+TM_{11} mode converter is shown in Figure 3.37. Since this structure is a symmetrical structure, input or output waveguide can be either port 1 or port 2. To eliminate this, port 1 side of the structure is tapered down in E plane to b = 12 mm so that only TE_{10} mode can enter from port 1 (input side). This final design is shown in Figure 3.38 with its dimensions.

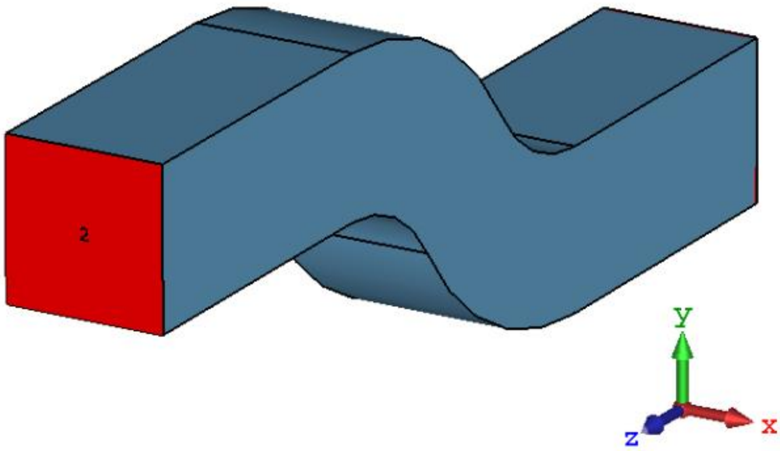

Figure 3.37: Designed TE_{10} to TE_{11}+TM_{11} double E-plane bend mode converter

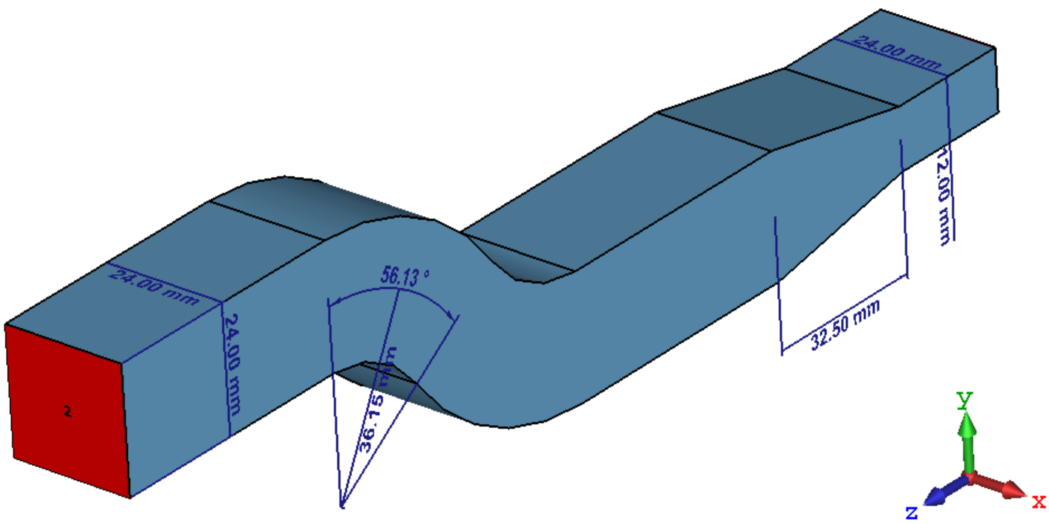

Figure 3.38: Final design of TE_{10} to TE_{11}+TM_{11} double E-plane bend mode converter

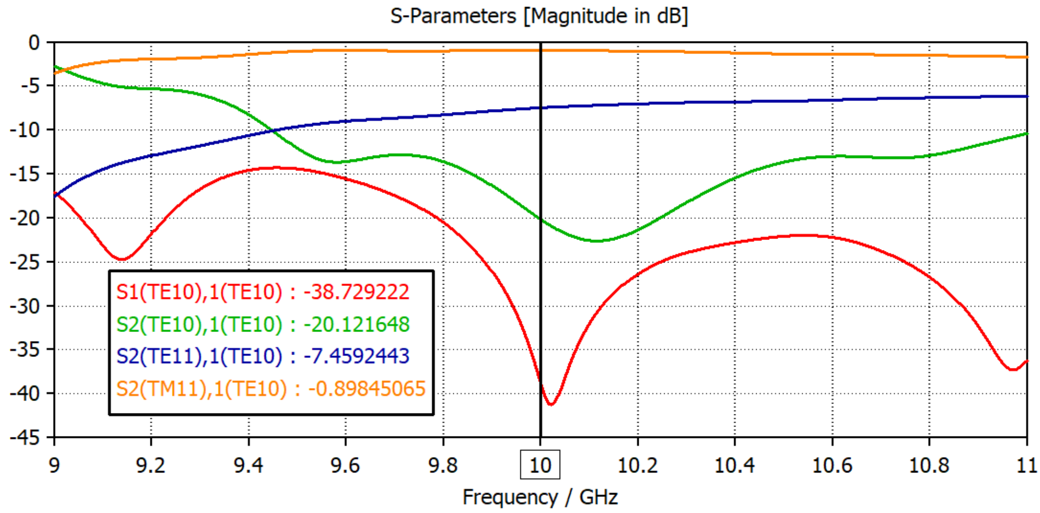

Figure 3.39: S parameter result of designed TE_{10} to TE_{11}+TM_{11} double E-plane bend mode converter

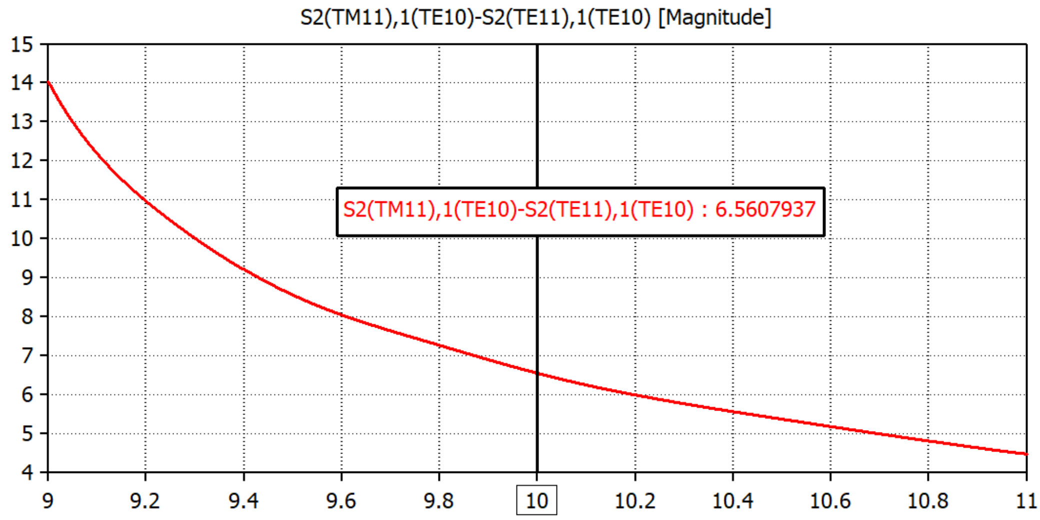

Figure 3.40: S2,1 difference of TM_{11} and TE_{11} modes

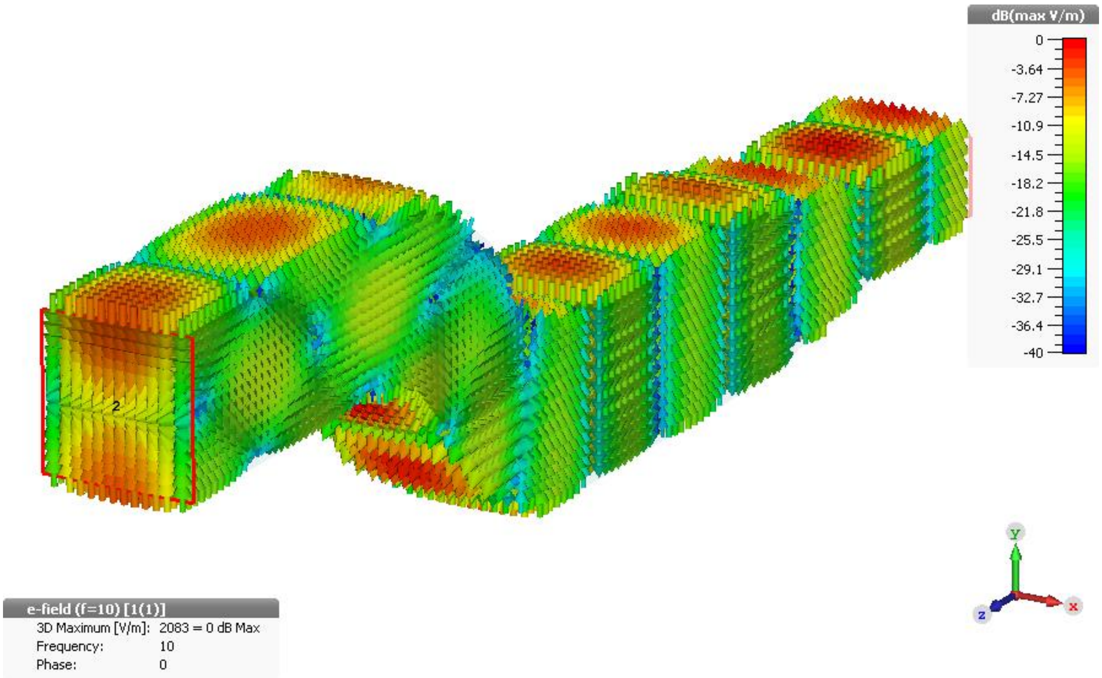

Figure 3.41: Electric field vectors inside designed TE_{10} to TE_{11}+TM_{11} converter at 10 GHz

Figure 3.39 shows the S parameter results of final TE_{10} to TE_{11}+TM_{11} mode converter design. As it can be seen from Figure 3.39, input reflection coefficient of TE_{10} mode is -38.73 dB at 10 GHz. There is no TE_{10} mode at the output port (port 2) at 10 GHz, S2(TE_{10}),1(TE_{10}) = -20.12 dB at 10 GHz. There is no TE_{10} to TE_{01} coupling between 9-11 GHz, S2(TE_{01}),1(TE_{10}) < -120 dB, and since it is very low, it is not shown in Figure 3.39. All energy of TE_{10} mode entered from input port (port 1) is converted into TE_{11} and TM_{11} modes. The combination ratio of TM_{11} and TE_{11} modes are shown in Figure 3.40. As it can be seen, there is 6.56 dB difference between two modes as desired.

Finally, Figure 3.41 shows the electric field vector inside designed mode converter when TE_{10} mode enters from the input port (port 1) at 10 GHz. As it can be seen, at the output port (port 2), desired electric field distribution is obtained.

Again, to compare dispersion effect of this type of waveguide structure with the dispersion effect of normal (regular) waveguide section, group delays of TE_{11} and TM_{11} modes in both cases are plotted in Figure 3.44. Although this comparison is done for only TE_{10} to TE_{11}+TM_{11} mode converter type (to save space), similar type of behavior is also valid for other bend mode converter given in this thesis. As it can be seen by comparing Figure 3.30 and Figure 3.44, in terms of dispersion, waveguide bend mode converter shows better results than irregular stepped mode converter.

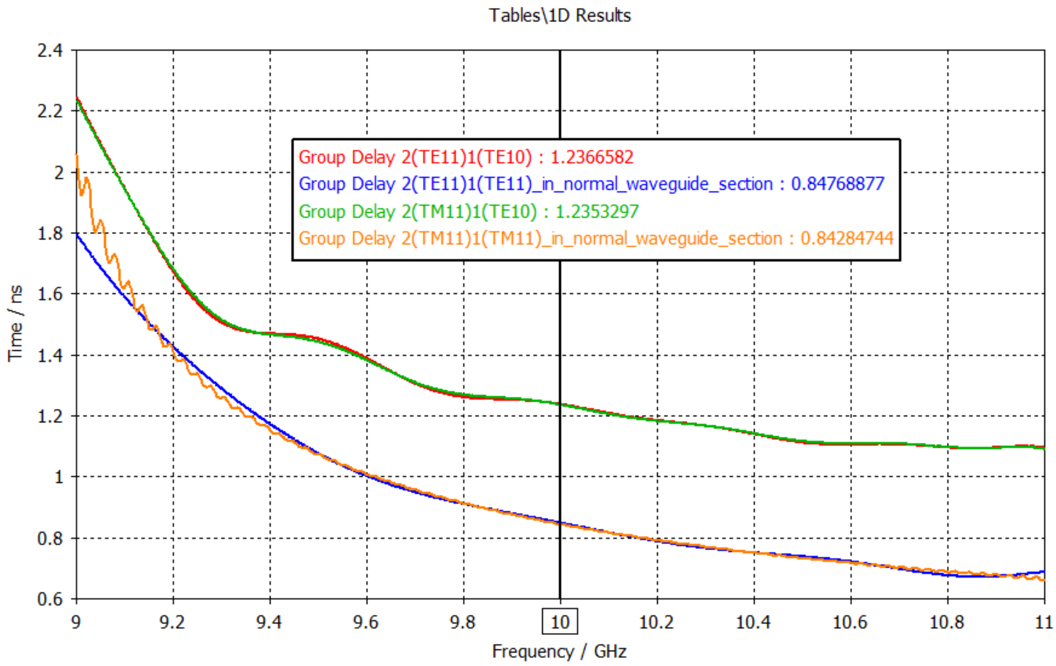

Figure 3.42: Comparison of group delays of TE_{11} and TM_{11} modes in TE_{10} to TE_{11}+TM_{11} waveguide bend mode converter and in normal waveguide section (a=b=24 mm, l= 118.5 mm)

3.2.3. Design Guidelines for Waveguide Bend Mode Converters

General design guidelines for waveguide bend mode converters are summarized below:

- Waveguide dimensions in input port, output port and bend sections must be same, and they must be chosen such that all desired modes propagate inside mode converter with minimum number of undesired modes.

- To design TE_{10} to TE_{20} mode converter, 2 H-plane bends are connected one after another

- To design TE_{10} to TE_{11}+TM_{11} mode converter, 2 E-plane bends are connected one after another

- In both cases, radii and angles of successive bends are set to equal to simplify design problem.

- As a result, only two optimization parameters are obtained: radius of bend and angle of bend

- S1(TE_{10}),1(TE_{10}) result shows input reflection coefficient of TE_{10} mode. This parameter must be as low as possible and it is used as one of the optimization goals.

- S2(TE_{10}),1(TE_{10}) result shows proportionally how much of TE_{10} mode entered from input port is not converted to desired mode and exits from output port. TE_{10} mode content at the output port is not a desired feature, so this result is used as one of optimization goal to make it as low as possible.

- S2(TE_{20}),1(TE_{10}) result shows how successfully TE_{10} mode at the input port is converted to TE_{20} mode at the output. If TE_{10} to TE_{20} mode converter is wanted to be designed, this should be used as one of the optimization goals to make it as high as possible.

- S2(TM_{11}),1(TE_{10}) – S2(TE_{11}),1(TE_{10}) difference shows the combination ratio of TE_{11} and TM_{11} modes and if TE_{10} to TE_{11}+TM_{11} mode converter is wanted to be designed, this should be used as one of the optimization goals to make it equal to 6.57 dB.

- Because of the waveguide dimensions, some unwanted modes may also propagate through mode converter, so S2(unwanted mode),1(TE_{10}) result should be used as one of the optimization goals to make is as low as possible.

- At the end of optimization process, symmetrical structure is obtained, therefore in both ways it can be used as mode converter, however, this is not desired. Since unidirectional mode conversion is desired, input waveguide dimensions are reduced with tapered transition to allow propagation of only TE_{10} mode at the input port hence this makes mode conversion operation unidirectional.

3.3. Waveguide Corner Mode Converters

The final waveguide mode converter structure, that is investigated in this thesis, is waveguide corner mode converter. In literature, there are some examples for H-plane corner TE_{10} to TE_{n0} mode converter, e.g. [86], [87], [88]. In these examples, H-plane corner waveguide with a couple of inductive metal matching posts are used. There are extensive work done for finding the solutions of waveguide corner regions and metal matching pins and some of them can be found in [43], [89], [90], [91], [92] and [93].

3.3.1. TE_{10} to TE_{20} Waveguide Corner Mode Converter

For this type of H-plane corner TE_{10} to TE_{20} mode converter, the structure given in [86] is investigated and simulated using CST Microwave Studio® software. Figure 3.43 shows the mode converter suggested in [86] and its dimensions. H-plane corner is used to convert TE_{10} mode to TE_{20} mode, 4 inductive metallic posts are used for matching and good mode conversion.

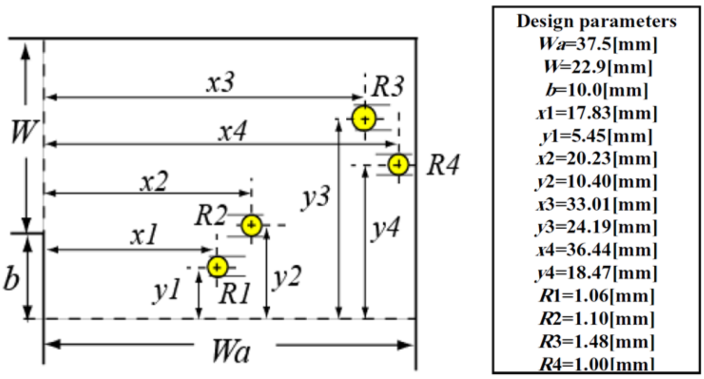

Figure 3.43: H-plane corner TE_{10}-TE_{20} mode converter with metallic posts (top view) [86]

This structure is investigated with and without 4 metallic post to see their matching and good mode conversion effects. The S parameter results for both cases are shown in Figure 3.44.

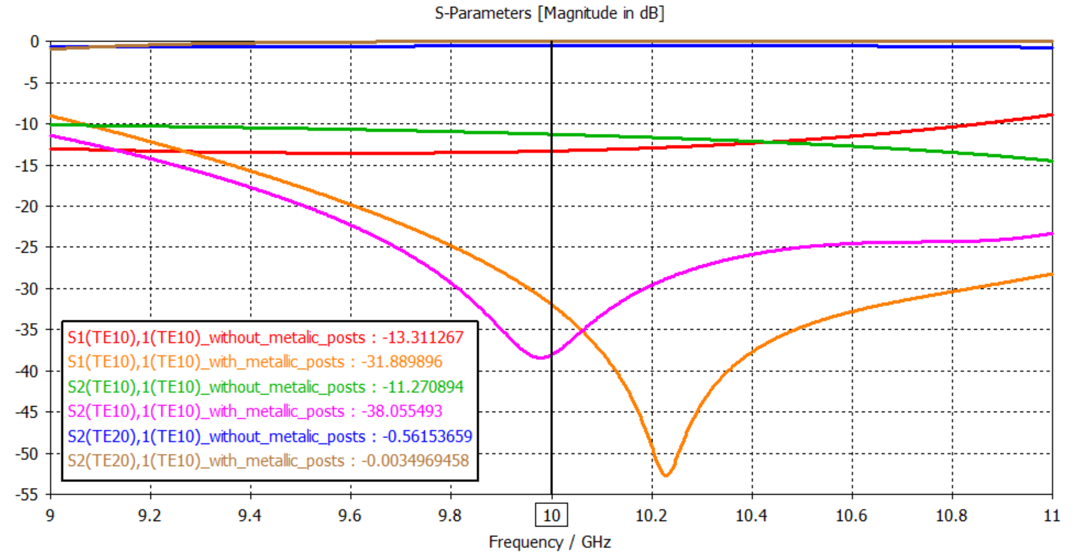

Figure 3.44: S parameters of H-plane corner TE_{10}-TE_{20} mode converter with and without metallic posts

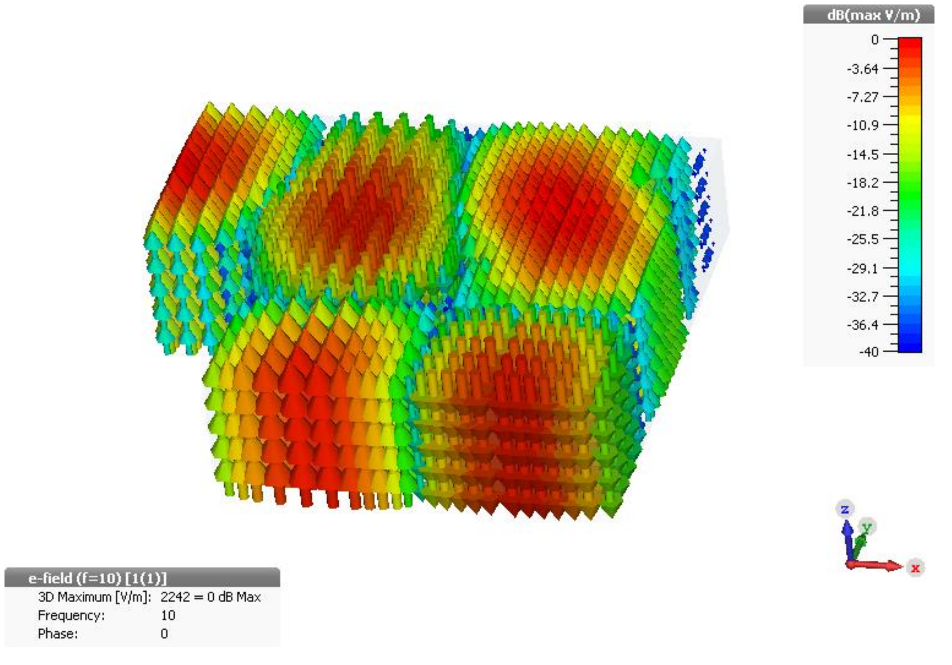

Figure 3.45: Electric field vectors inside investigated TE_{10} to TE_{20} converter at 10 GHz

As it can be seen from Figure 3.44, using 4 metallic posts in the corner region decreased the input reflection coefficient of TE_{10} mode from -13.31 dB to -31.89 dB at 10 GHz and it decreased the TE_{10} mode content at the output from -11.27 dB to -38.06 dB at 10 GHz. As a result, mode conversion loss is decreased from -0.56 dB to -0.0035 dB at 10 GHz.

Figure 3.45 shows the electric field vectors inside this mode converter when TE_{10} mode enters from input port (port 1) at 10 GHz. As it can be seen from Figure 3.45, at the output port (port 2), TE_{20} mode is obtained.

Using H-plane corner to generate TE_{20} mode makes sense because H-plane bend for oversized waveguide is used to generate TE_{20} mode in section 3.2.1. Therefore, it seems like E-plane corner with metallic posts can be used to convert TE_{10} mode to TE_{11}+TM_{11} mode combination with same analogy. In this thesis, this idea is tried in section 3.3.3 and good mode conversion results are obtained. This will be explained in detail in the section 3.3.3.

3.3.2. TE_{10} to TE_{30} Waveguide Corner Mode Converter

This type of corner mode converter is designed in [87]. This mode converter also uses H-plane corner (H plane corners can be used to convert TE_{10} mode to TE_{n0} modes in general, as in [88] and [90]). Again, metallic posts are used for input matching and good mode conversion. This time 5 metallic posts are used. Figure 3.46 shows the structure of this mode converter with its parameters.

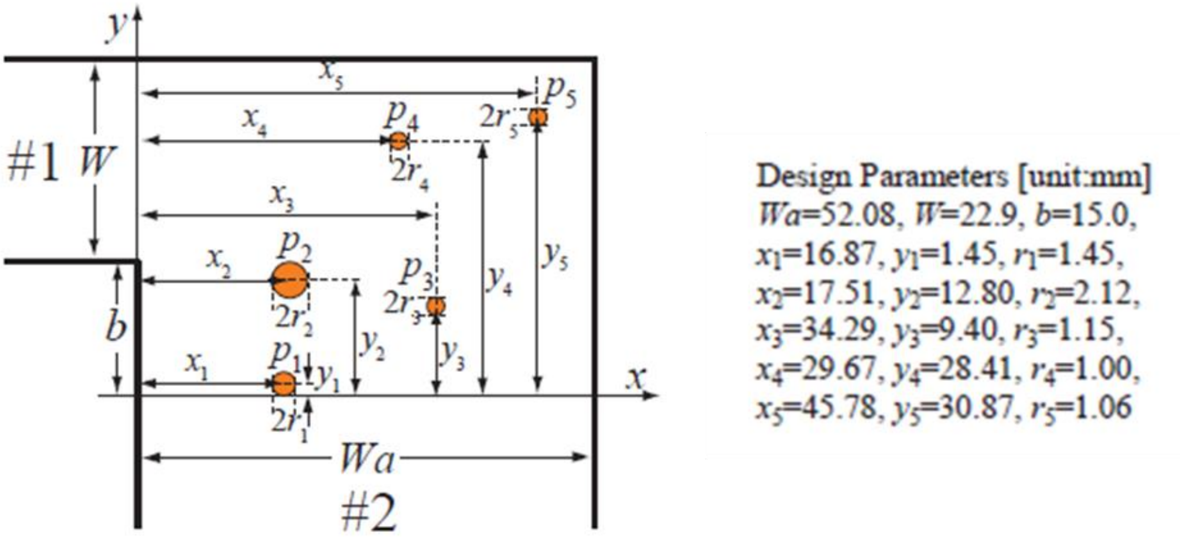

Figure 3.46: H-plane corner TE_{10}-TE_{30} mode converter with metallic posts (top view) [87]

In CST Microwave Studio®, this offered mode converter is investigated and simulated. Figure 3.47 shows its S parameter results and Figure 3.48 shows the electric field vectors inside this mode converter when TE_{10} mode enters from the input port (port 1) at 10 GHz. As it can be seen from S parameter results and the electric field distribution at the output port (port 2), TE_{10} mode is successfully converted into TE_{30} mode.

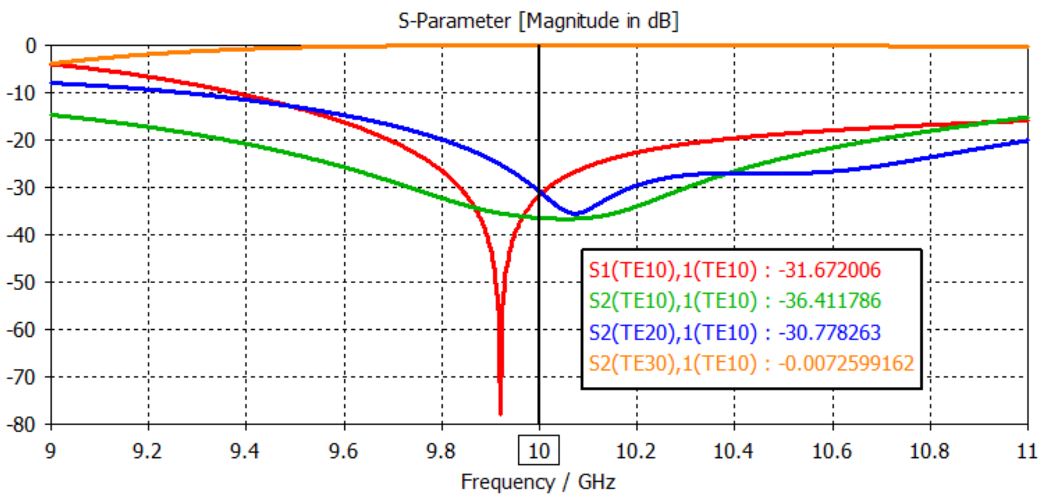

Figure 3.47: S parameters of H-plane corner TE_{10}-TE_{30} mode converter with metallic posts

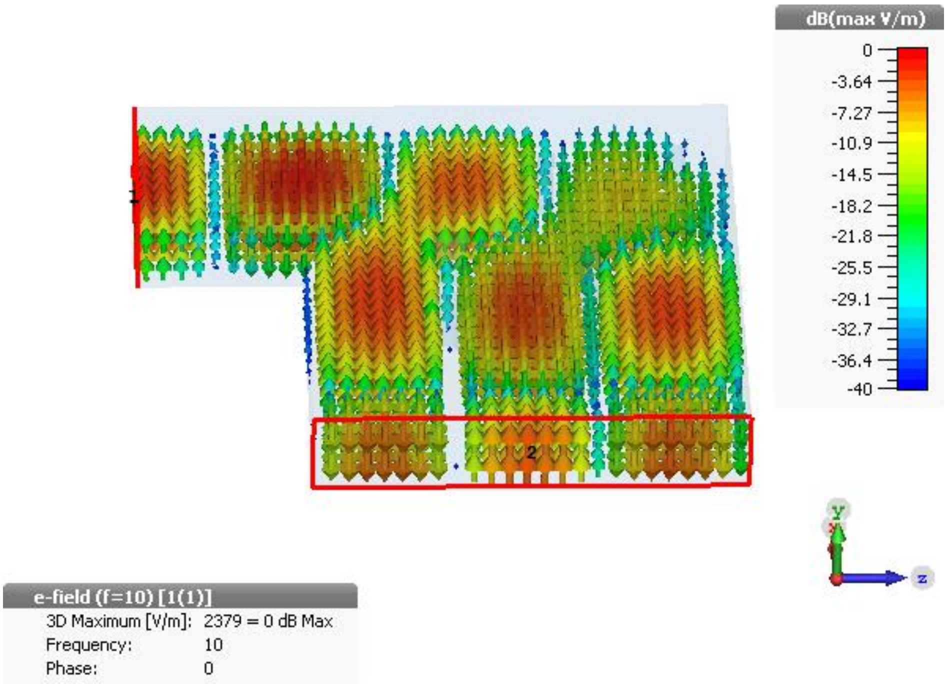

Figure 3.48: Electric field vectors inside investigated TE_{10} to TE_{30} converter at 10 GHz

3.3.3. TE_{10} to TE_{11}+TM_{11} Waveguide Corner Mode Converter

When investigating the mode converters which uses H-plane corners and inductive metallic posts, it is seen that this type of mode converter generates similar modes with H-plane bend mode converters. Therefore, the idea of using E-plane corner with capacitive metallic posts to convert TE_{10} mode to TE_{11}+TM_{11} mode combination emerged because if E-plane bend can generate this mode combination as in the section 3.2.2, with same analogy E-plane corner with capacitive metallic posts can be used to convert TE_{10} mode to TE_{11}+TM_{11} mode combination. In the literature, no rectangular waveguide corner mode converter example which uses this idea is found, so this idea is tried here to accomplish this mode conversion operation.

Figure 3.49 shows the starting E-plane corner structure. Input waveguide is connected to port 1 as before and its dimensions are set to a = 24 mm & b = 12 mm to allow propagation of only TE_{10} mode between 9-11 GHz. Output waveguide, which is a square waveguide, is connected to port 2 and its dimensions are set to a = 24 mm & b = 24 mm to allow propagation of only TE_{10}, TE_{01}, TE_{11} and TM_{11} modes between 9-11 GHz. This initial structure is simulated in CST Microwave Studio® software to see if our suggestion is valid. Figure 3.50 shows the S parameter results of this initial structure.

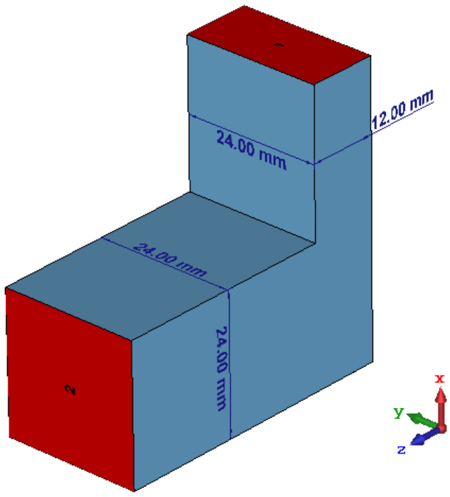

Figure 3.49: Initial E-Plane corner structure with its waveguide dimensions

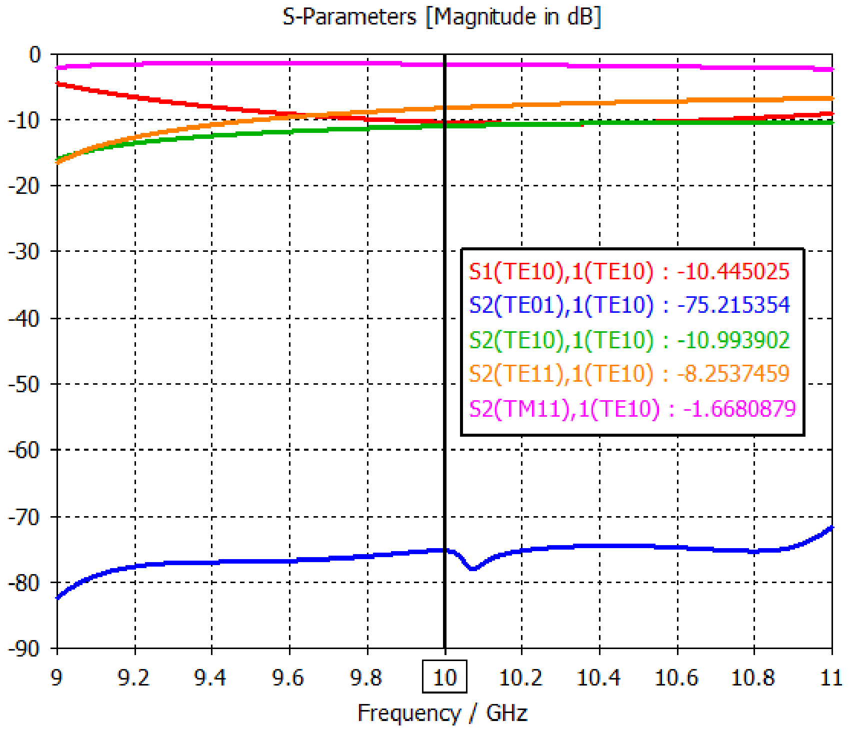

Figure 3.50: S parameter results of initial E-Plane corner structure

As it can be seen from Figure 3.50, S parameter results of this initial E-plane corner structure are promising. The input reflection coefficient of TE_{10} mode is not as good as desired but it is good enough for an initial point, which is -10.44 dB at 10 GHz. TE_{10} mode suppression within this structure is not as good as desired but it is encouraging enough for an initial point, its value is -10.99 dB at 10 GHz. Within this structure, TE_{01} mode is not generated because $S2(TE_{01}),1(TE_{10})$ is equal to -75.21 dB at 10 GHz. Finally, the mode conversion losses are not as low as desired but as an initial point $S2(TM_{11}),1(TE_{10})$ and $S2(TE_{11}),1(TE_{10})$ values are -1.67 dB and –8.25 dB at 10 GHz respectively. The TM_{11}+TE_{11} modes combination ratio is very close to desired value, $S2(TM_{11}),1(TE_{10})$ - $S2(TE_{11}),1(TE_{10})$ = 6.58 dB at 10 GHz.

First capacitive metallic post is introduced in corner region for input matching of TE_{10} mode, output suppression of TE_{10} mode and decreasing mode conversion losses of TE_{11} and TM_{11} modes. The position and radius of this first metallic post are optimization parameters. Optimization goals and their weights are set as follows:

- $S1(TE_{10}),1(TE_{10})$ = -20 dB at fc = 10 GHz, weight = 1
- $S2(TE_{10}),1(TE_{10})$ = -20 dB at fc = 10 GHz, weight = 1
- $S2(TM_{11}),1(TE_{10})$ - $S2(TE_{11}),1(TE_{10})$ = 6.57 dB at fc = 10 GHz, weight = 1

After this first optimization process, structure shown in Figure 3.51 is obtained. The S parameter results of the structure shown in Figure 3.51 are given in Figure 3.52. As it can be seen from Figure 3.52, $S1(TE_{10}),1(TE_{10})$ design criteria goal is not reached after first post and its optimization process.

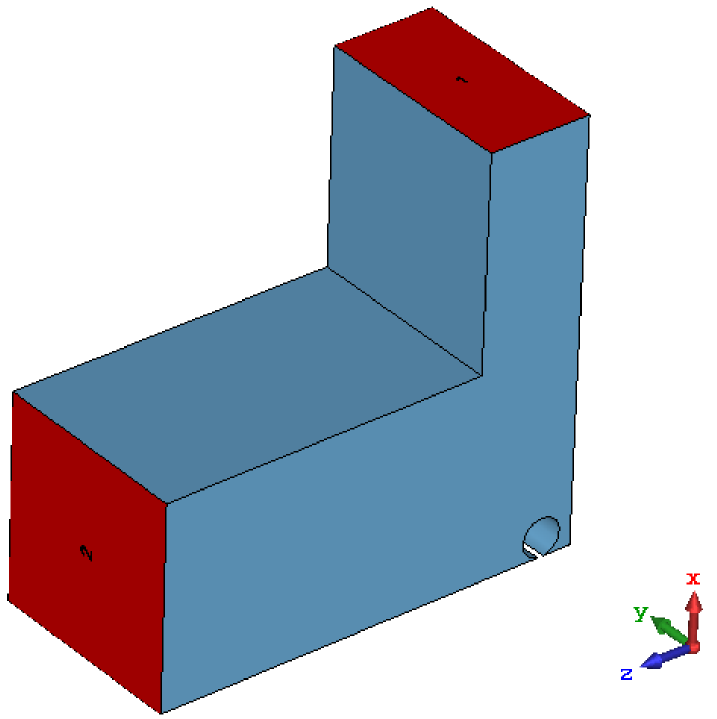

Figure 3.51: Obtained structure after first metallic post and its optimization process

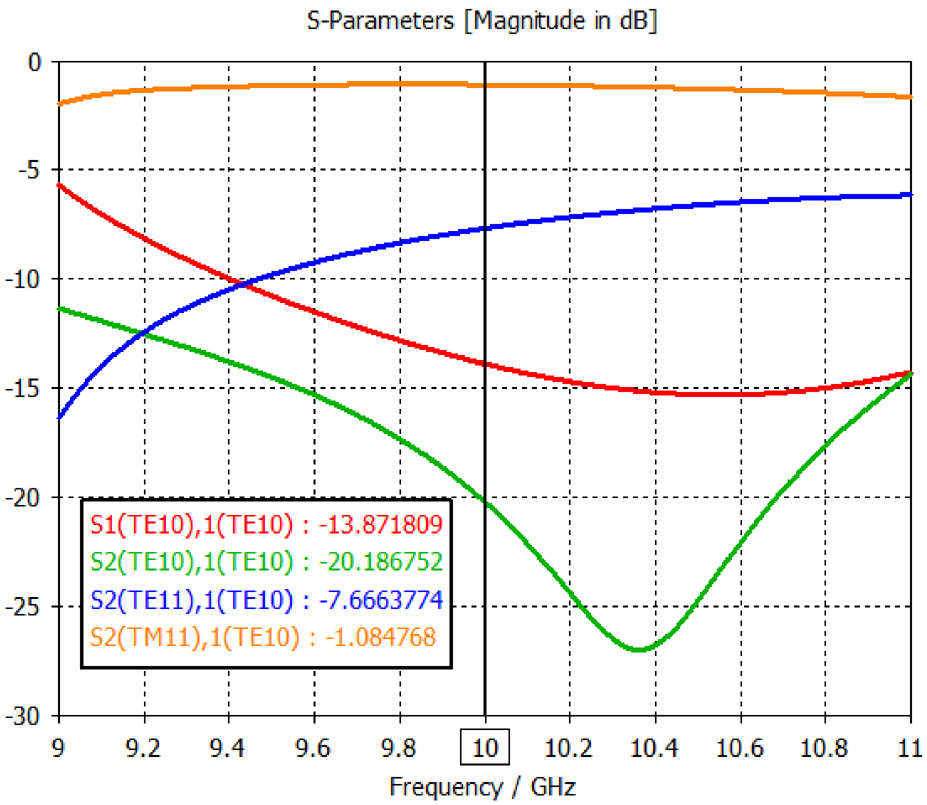

Figure 3.52: S parameter results of obtained structure after first metallic post and its optimization process

Second capacitive metallic post introduced, since input reflection goal is not reached after first capacitive metallic post and its optimization design process. The position of this second post and its radius are the design parameters of second design process. In this second optimization process, the position and radius of first post is kept same as obtained values after first optimization process. Again, the optimization goals and their weight are same as in the previous optimization process. Figure 3.53 shows the obtained TE_{10} to TE_{11}+TM_{11} mode converter after this second optimization process. Table 3.3 shows the post parameter values with respect to local coordinate system (U-V-W). Figure 3.54 shows the obtained S parameter results after this second and final optimization process. As it can be seen from Figure 3.54, all design criteria are reached.

Table 3.3: Obtained parameters of two metallic posts

Parameter name	Description of Parameter	Value (~mm)
w1	w position of the 1st post center	2.25
w2	w position of the 2nd post center	8.18
u1	u position of the 1st post center	3.67
u2	u position of the 2nd post center	6.62
r1	radius of 1st post	2.27
r2	radius of 2nd post	1.93

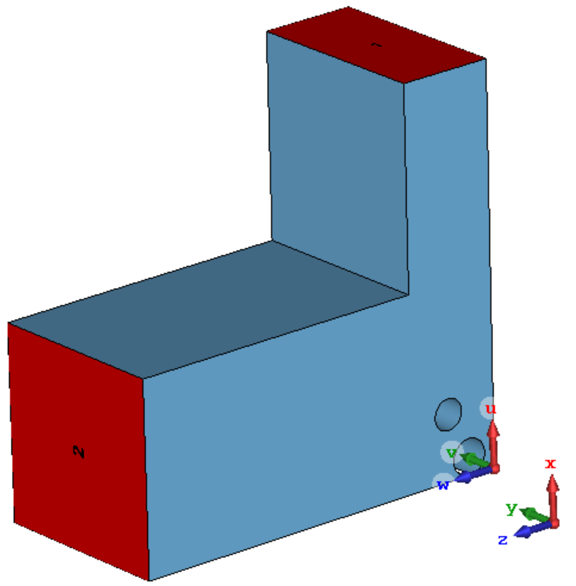

Figure 3.53: Obtained E-plane corner TE_{10} to TE_{11}+TM_{11} mode converter with two metallic posts

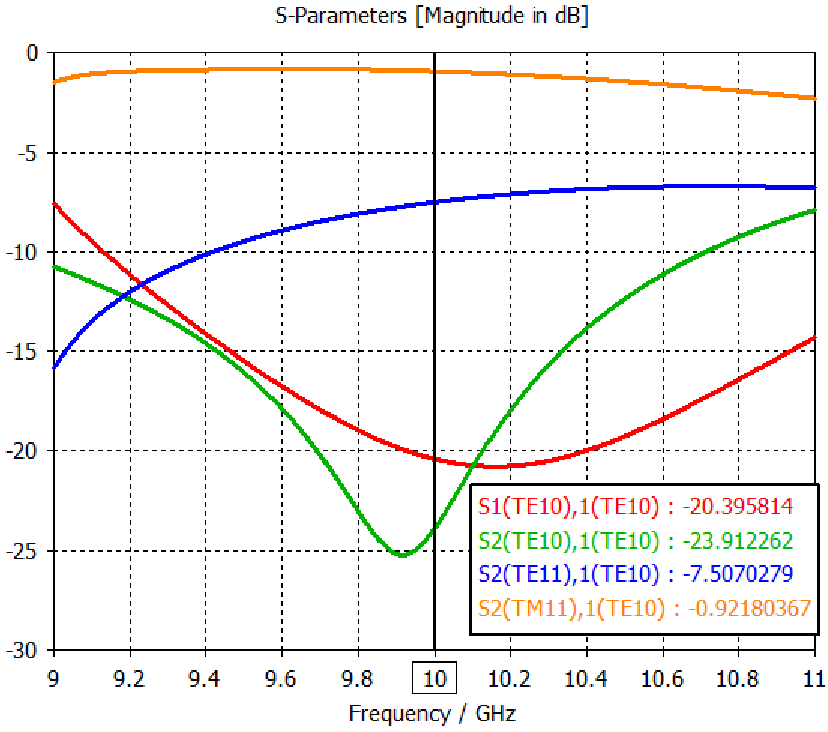

Figure 3.54: S parameter results of obtained E-plane corner TE_{10} to TE_{11}+TM_{11} mode converter with two metallic posts

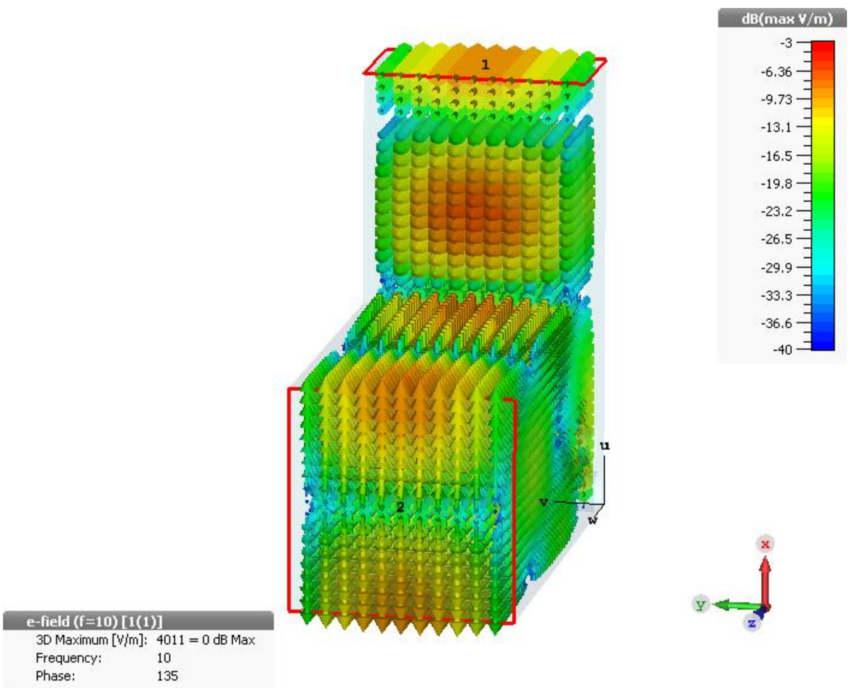

Figure 3.55: Electric field vectors inside designed TE_{10} to TE_{11}+TM_{11} converter at 10 GHz

As it can be seen from Figure 3.54, by introducing two capacitive metallic posts, desired S parameter results are obtained. Figure 3.55 shows the electric field vectors within designed mode converter when TE_{10} mode enters from input port (port 1) at 10 GHz. Electric field distribution at the output port (port 2) is the desired TE_{11}+TM_{11} mode combination electric field distribution.

Again, to compare dispersion effect of this type of waveguide structure with the dispersion effect of normal (regular) waveguide section, group delays of TE_{11} and TM_{11} modes in both cases are plotted in Figure 3.56. Although this comparison is done for only TE_{10} to TE_{11}+TM_{11} mode converter type (to save space), similar type of behavior is also valid for other corner mode converters given in this thesis. As it can be seen by comparing Figure 3.30 and Figure 3.56, in terms of dispersion, waveguide corner mode converter shows better results than irregular stepped mode converter.

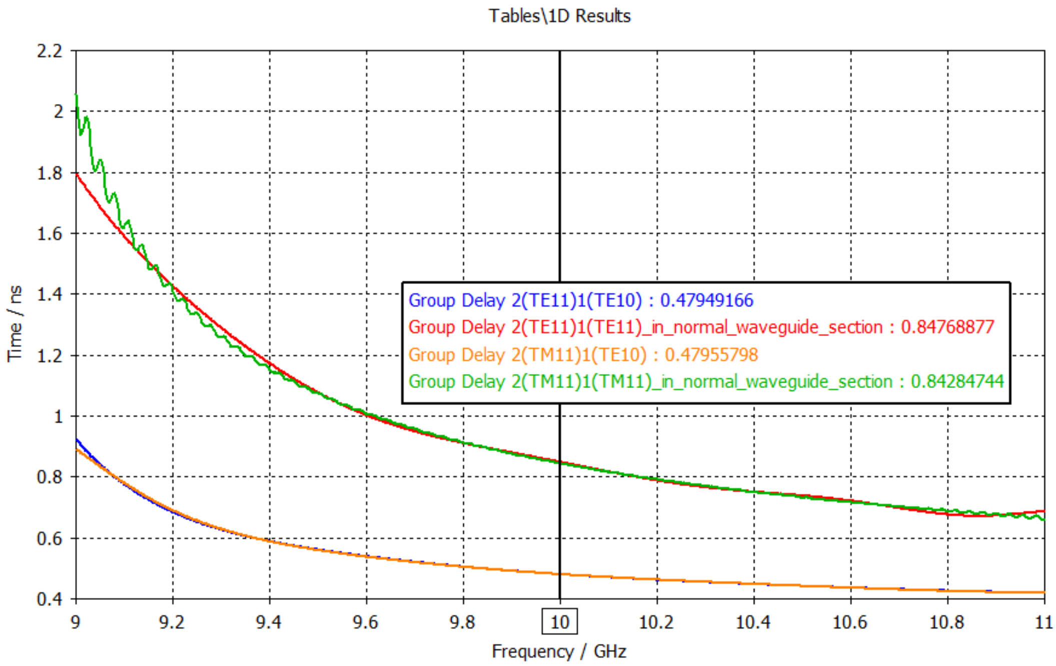

Figure 3.56: Comparison of group delays of TE_{11} and TM_{11} modes in TE_{10} to TE_{11}+TM_{11} waveguide corner mode converter and in normal waveguide section (a=b=24 mm, l= 118.5 mm)

3.3.4. General Design Guidelines for Waveguide Corner Mode Converter

Here, general design guidelines for designing waveguide corner mode converters are summarized:

- Dimensions of input waveguide should be chosen such that only TE_{10} mode propagates into input port (port 1).
- Dimensions of output waveguide should be chosen such that only desired mode/mode combinations propagate with minimum number of unwanted other modes through output port.
- If TE_{10} to TE_{n0} (n =2 or 3) mode converter is wanted to be designed, H-plane corner should be used.
- If TE_{10} to TE_{11}+TM_{11} mode converter is wanted to be designed, E-plane corner should be used.
- To increase matching and to improve mode conversion, inductive metallic posts should be used for TE_{10} to TE_{n0} mode converter, capacitive metallic posts should be used for TE_{10} to TE_{11}+TM_{11} mode converter.
- Design process should start with one metallic post. The position and radius of this post are optimization parameters.
- After this first optimization process, if the results are not good enough, the second metallic post should be added. In this second optimization process, only the position and radius of the second post are optimization parameters.
- If the results after this second optimization process are still not good enough, one more metallic post is again added, and the optimization cycle continues until desired performance is achieved.
- S1(TE_{10}),1(TE_{10}) result shows input reflection coefficient of TE_{10} mode. This parameter must be as low as possible and it is used as one of the design criteria.

- $S2(TE_{10}),1(TE_{10})$ result shows proportionally how much of TE_{10} mode entered from input port is not converted to desired mode and exits from output port. TE_{10} mode content at the output port is not a desired feature, so this result is used as one of the design criteria to make it as low as possible.

- $S2(TE_{n0}),1(TE_{10})$ result shows how successfully TE_{10} mode at the input port is converted to TE_{20} mode at the output. If TE_{10} to TE_{n0} (n= 2 or 3) mode converter is wanted to be designed, this should be used as one of the design criteria to make it as high as possible.

- $S2(TM_{11}),1(TE_{10})$ – $S2(TE_{11}),1(TE_{10})$ difference shows the combination ratio of TE_{11} and TM_{11} modes and if TE_{10} to TE_{11}+TM_{11} mode converter is wanted to be designed, this should be used as one of the design criteria to make it equal to 6.57 dB.

- Because of the waveguide dimensions, some unwanted modes may also propagate through mode converter, so S2(unwanted mode),1(TE_{10}) result should be used as one of the design criteria to make is as low as possible.

CHAPTER 4

FABRICATION OF RECTANGULAR WAVEGUIDE MODE CONVERTER USING 3D PRINTER AND MEASUREMENT RESULTS

Waveguides are usually fabricated by CNC machining or metal casting. In this thesis, initially selected mode converter design is thought to be fabricated using CNC machining. However, the fabrication bidding of CNC machining or metal casting is found to be expensive. Therefore, the idea of 3D printing (popular fast prototyping method of recent years) of this mode converter come into mind. Since the waveguide structures are suitable for this type of fabrication process, this idea makes sense. In addition, there are some advantages of 3D printing over general fabrication techniques: light weight product, time and cost-effective production, fabrication of more challenging models. The main disadvantage of using 3D printing in the fabrication of waveguide structures is that the printing material is plastic, therefore is not conductive material and the fabricated waveguide structure will not work directly after the fabrication process. The surfaces of fabricated structure should be turned into conductive surfaces. The thicknesses of these conductive surfaces are dependent on skin depth in the operating frequency.

Two ideas came into mind when method for making these plastic surfaces conductive was search. The first idea is converting these surfaces into metals (copper to be exact) by electroforming process. There are a lot of tutorials and examples on the Internet about this process. There are also some companies in Turkey which can electroform plastic objects with metals. Although this method gives the best result of making surfaces of 3D printed waveguide conductive, it was not preferred because it is not time and/or cost effective. The electroforming companies are not eager to do this task when the production quantity is small, or they charge a lot of money for this task. Therefore, it not appropriate for prototyping purpose. One can also do this task by himself/herself, but the process is hard and exhausting, and he/she may not be able to find all required tools or chemicals.

The second idea is using conductive paints or inks. There are some conductive paints/inks sold on market and they are usually used for repairing damaged printed circuit boards or electronic components. These products consist of silver or other metal particles and glue. The application of these products is very easy. They can be applied to the surface by paint brush. After the application, they usually need time and/or heat to dry. Their sheet resistances are dependent on their paint content and most of them have low sheet resistance value. They are also very inexpensive. Because of these advantages, these products are used to convert plastic surfaces of 3D printed waveguide structure into conductive surfaces.

After 1 mode converter is selected, 3D printed, painted and tested, the literature search was done to see if anyone else had the same waveguide fabrication idea. The work done in January 2017 and described in [94] is found. The authors of [94] had the same idea, they fabricated a waveguide component using 3D printer and then they painted it with conductive ink (different than the one used in this thesis) to make it work in higher frequency. The reader is also encouraged to look at their work.

4.1. Selection of Mode Converter to Be Fabricated

5 discrete stepped TE_{10} to TE_{11}+TM_{11} mode converter mentioned in section 3.1.6 is selected to fabricated. There are two main reasons for this choice.

First reason is that this mode converter converts TE_{10} mode into combinations of two modes, instead of one mode, so this design was more challenging. These two modes should be combined in specific ratios to radiate required radiation pattern and therefore it was more sensitive towards errors.

Secondly, selected mode converter should be discrete stepped mode converter because their S parameter responses behave more wildly (fast changing and resonantly) and they have the narrowest bandwidth among 3 types of mode converters describe in Chapter 3.

Because of these properties of S parameters of discrete stepped mode converters, they are more vulnerable to calculation errors and production errors, so if this type of mode converter is fabricated, tested and verified by S parameter and radiation pattern measurement, the performance estimation of CST Microwave Studio® software and the fabrication method described in this section are verified for all types of mode converters in Chapter 3. In other words, if the most problematic type of mode converter is fabricated by the method described here and it shows the same results with CST Microwave Studio® software simulation, both simulation software and 3D printing fabrication process are verified, and they can be used for all other mode converter designs in Chapter 3.

4.2. Preparation of Fabrication Model of TE_{10} to TE_{11}+TM_{11} Mode Converter

CNC machining was initially thought to be used for fabrication of this mode converter as mentioned before. Therefore, the fabrication model of this converter is prepared by keeping this in mind. Although, 3D printing method and painting with conductive paint is used as fabrication process, model which is prepared for CNC machining was fabricated and it made painting process easier (the surfaces were easier to reach and to be painted). Here, how the final fabrication model of this mode converter is obtained from the one described in section 3.1.6 is explained.

Firstly, the mode converter model given in section 3.1.6 is taken and blends (with radius 3 mm, due to CNC machine drill bits) are introduced on some of the mode converter edges in order to make this mode converter ready for CNC machining. These blends created performance and mode conversion deteriorations, so again local optimization is done to obtain best performance in the presences of these blends. Figure 4.1 shows the obtained model from this local optimization. Figure 4.2 shows the S parameter result of this model.

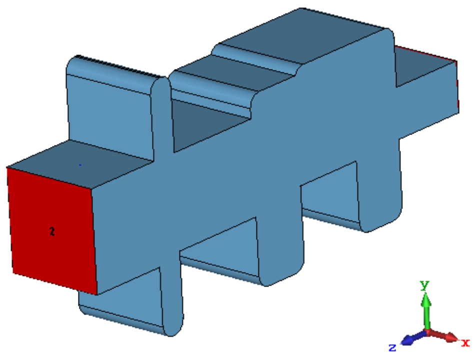

Figure 4.1: Obtained mode converter model with blends

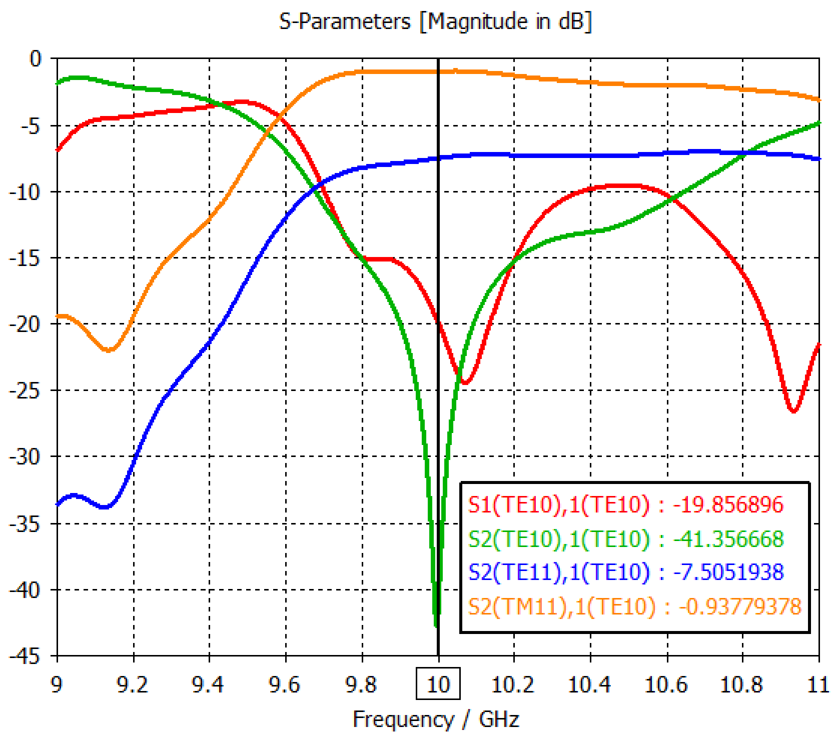

Figure 4.2: S parameter result of obtained mode converter model with blends

Since the dimensions of input waveguide is not a standard WR90 waveguide dimensions, the transition region (from custom dimensions a = 24 mm & b = 12 mm to standard WR90 dimensions a = 22.86 mm & b = 10.16 mm) is added. Figure 4.3 shows the transition region connected to mode converter.

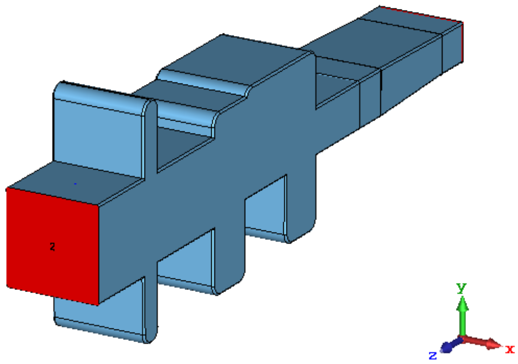

Figure 4.3: Addition of transition region

Finally, horn antenna is connected output port of mode converter and then whole structure is cut in the middle of H-plane and divided into 4 components. In order to assemble all these parts, screw holes are opened, and the final fabrication model shown in Figure 4.4 is obtained. S parameter result of this final mode is shown in Figure 4.5 and its 3D radiation pattern is shown in Figure 4.6. As it can be seen from Figure 4.6, radiating this TE_{11}+TM_{11} modes combination generates elevation difference channel radiation pattern.

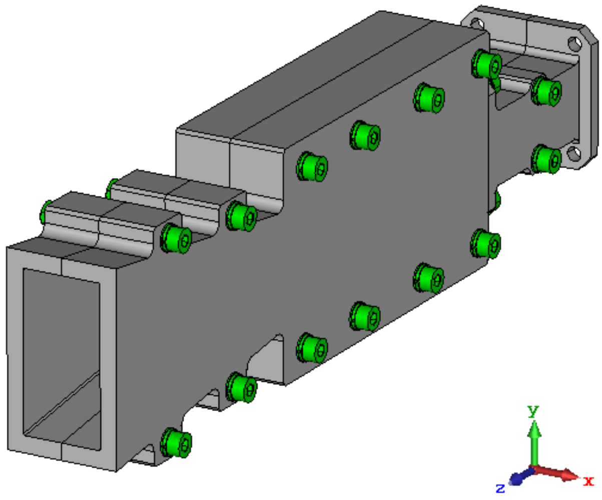

Figure 4.4: Fabrication model

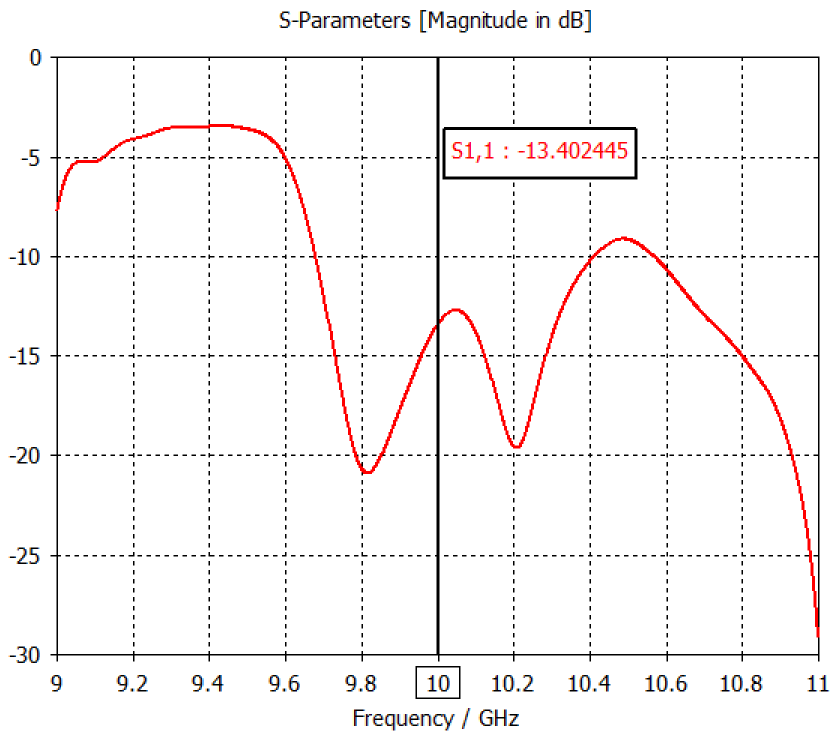

Figure 4.5: S11 of fabrication model

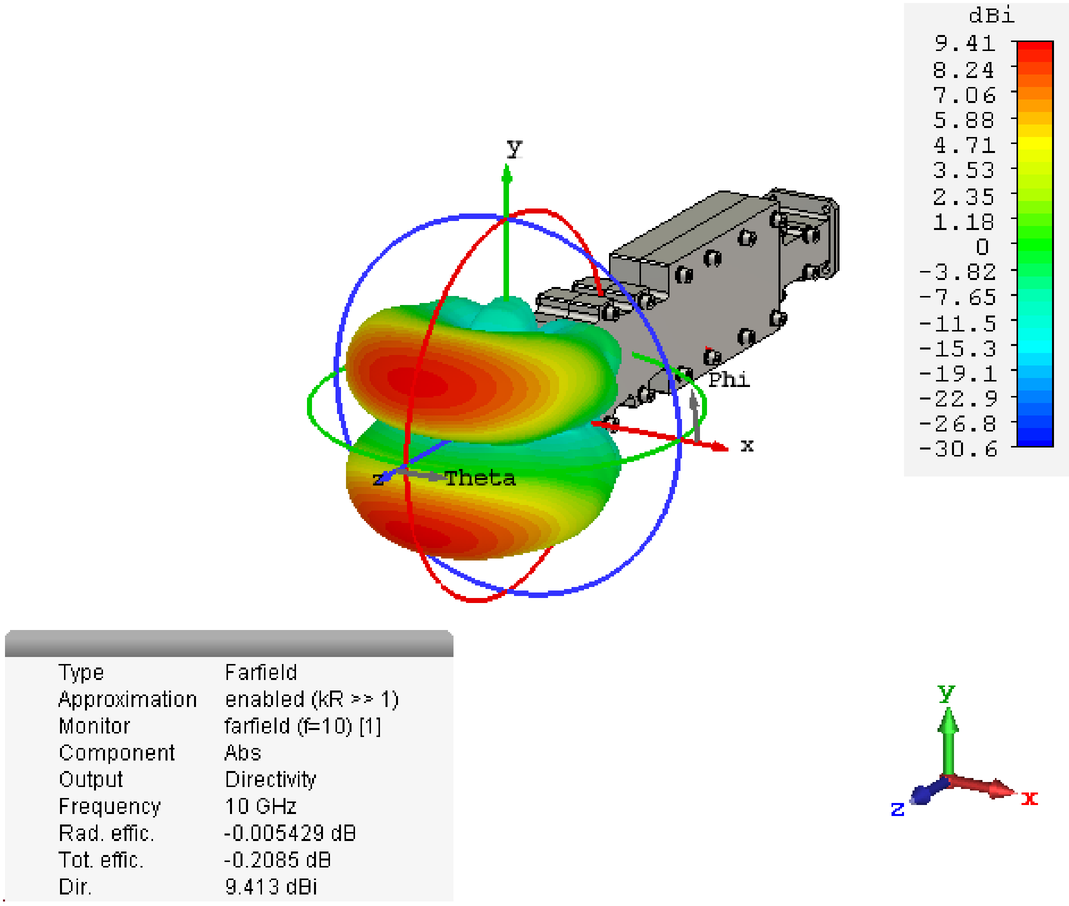

Figure 4.6: 3D radiation pattern of fabrication model

4.3. 3D Printer and Printing Material Choice

Zortrax M200 (Figure 4.7) was employed as 3D printer for the fabrication of mode converter. There were several reasons why this choice was made. The main reason was this 3D printer was readily available. Second reason was that it was easy to use, and the software interface of this printer was very easy for beginners. Thirdly, its printing resolution (between 90-400 microns) and speed was very good. Fourth reason was that the printing materials (types of plastics) that is used by this 3D printer is high quality. Fifth reason was that its build volume was 200 x 200 x 180 mm and this volume was sufficient for the fabrication of mode converter. Finally, its model input file types were compatible with the model export/import file types of CST Microwave Studio® software. Table 4.1 shows the properties of this 3D printer, [95].

Table 4.1: Properties of Zortrax M200 3D Printer

printing

technology	LPD
build volume	200 x 200 x 180 mm
resolution	90-400 microns
material container	spool
wall thickness	optimal: 800 microns
resolution of single printable point	400 microns
material diameter	1.75 mm (0.069 in)
nozzle diameter	0.4 mm (0.015 in)
minimum single positioning	1.5 microns
positioning precision (X/Y)	1.5 microns
z-axis single step	1.25 microns
dimensional accuracy	+/- 0.2% *
angle accuracy	+/- 0.5˚ **
additional information	each delivered printer may have worked up to 50 hours during the quality control test prints

temperature

extruder maximum temperature	380°C (716°F)
heated platform	yes
platform maximum temperature	110°C (230°F)
ambient operation temperature	20°-35°C (68°-95°F)
storage temperature	0°-35°C (32°-95°F)

electrical

AC input	110/240 V ~ 2 A 50/60 Hz
power requirements	24 V DC @ 11 A
power consumption	190 W

3D printer

support	Mechanically removed - printed from the same material as the model
extruder	Single
connectivity	SD card (included)
dedicated materials	Z-PLA Pro Z-ASA Pro Z-ABS Z-ULTRAT Z-HIPS Z-GLASS Z-PCABS Z-PETG Z-ESD
external materials	Applicable

software

software bundle	Z-SUITE
file types	stl, obj, dxf, 3mf.
supports	Mac OS X / Windows 7 and newer versions

Figure 4.7: Zortrax M200 3D printer

ABS (Acrylonitrile butadiene styrene, also known as Lego plastic) is chosen as 3D printing material. It is one of the most popular plastics for 3D printing and injection molding. Its density is almost equal to density of water and it is very light weight, but it has high impact resistance and toughness. It also has mat color, so it can be easily painted with conductive paint. Since it is one of very popular plastic types in manufacturing, there are some companies in Turkey which have area of expertise in electroforming ABS plastics. By the time of choosing printing material, ABS filament was also readily available, so by keeping in mind above properties, it was chosen as 3D printing material.

4.4. Fabrication Process

The fabrication model (shown in Figure 4.4) is export from CST Microwave Studio® simulation software and imported into 3D modelling and printing software (Z-SUITE) of Zortrax M200. In here, 4 components of fabrication model are checked once again.

By setting the printing resolution to 200 microns, these 4 components are printed. In order to print these components, Z-SUITE software automatically places building supports. Figure 4.8 shows one of the components of fabrication model together with its building supports in Z-SUITE software. If this support positioning is appropriate for the user, user confirms the operation and printing process begins. Figure 4.9 shows the fabricated component shown in Figure 4.8. After the fabrication process of components, building supports are mechanically removed and desired components are obtained. Figure 4.10 shows 3D printed 4 components.

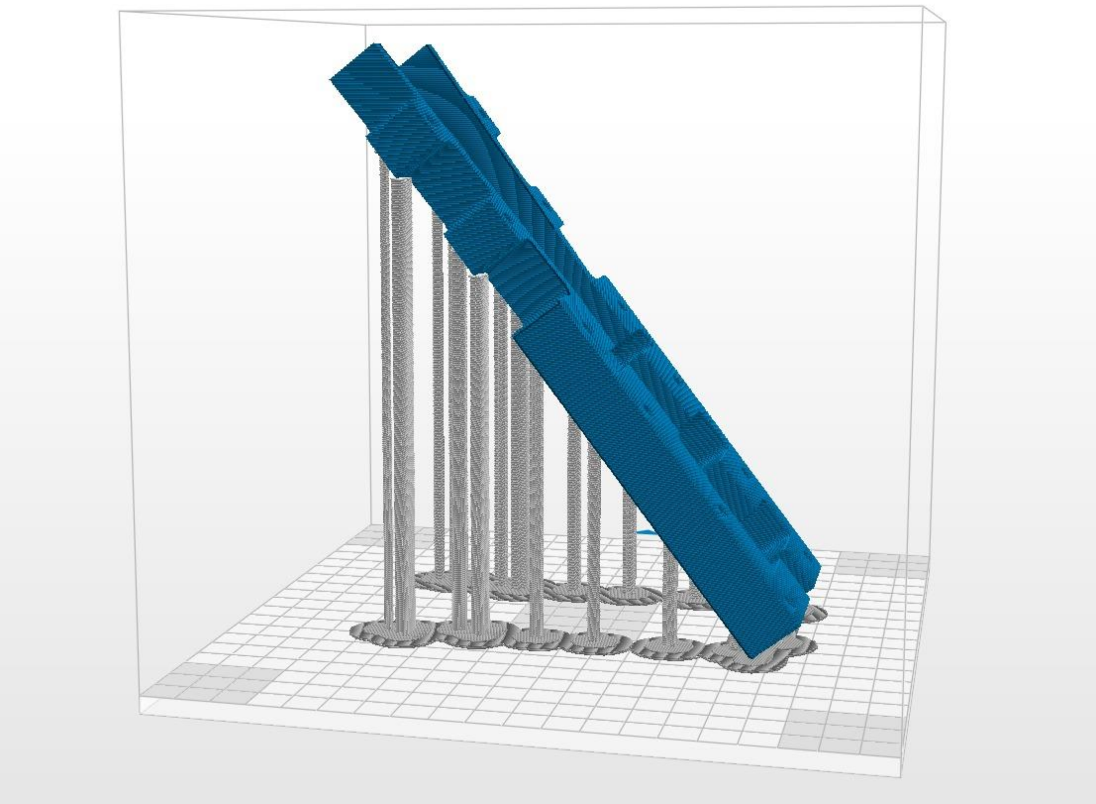

Figure 4.8: One of the components of fabrication model together with its building supports in Z-SUITE software

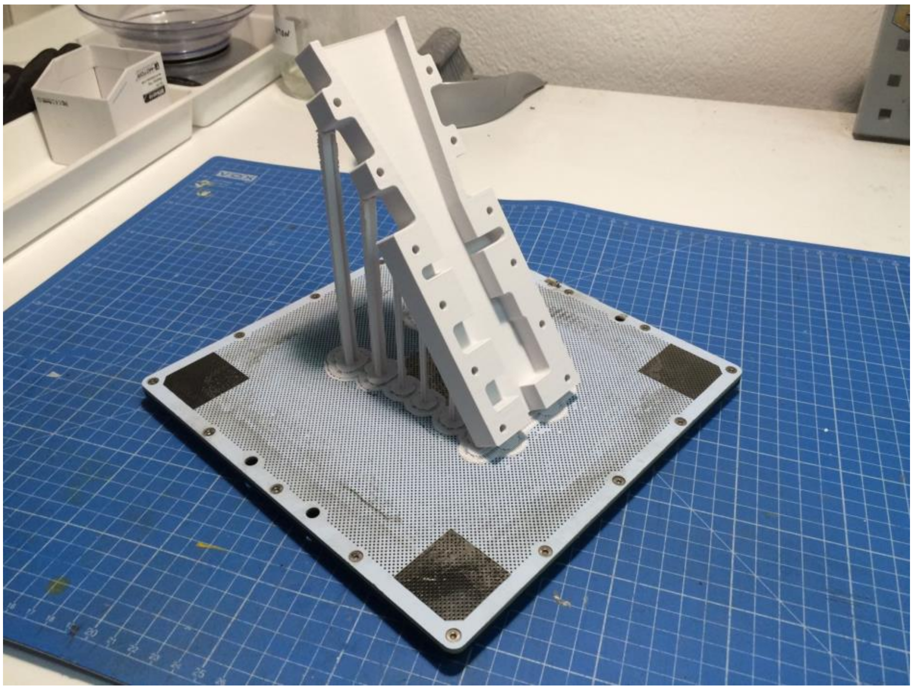

Figure 4.9: 3D printed component shown in Figure 4.8

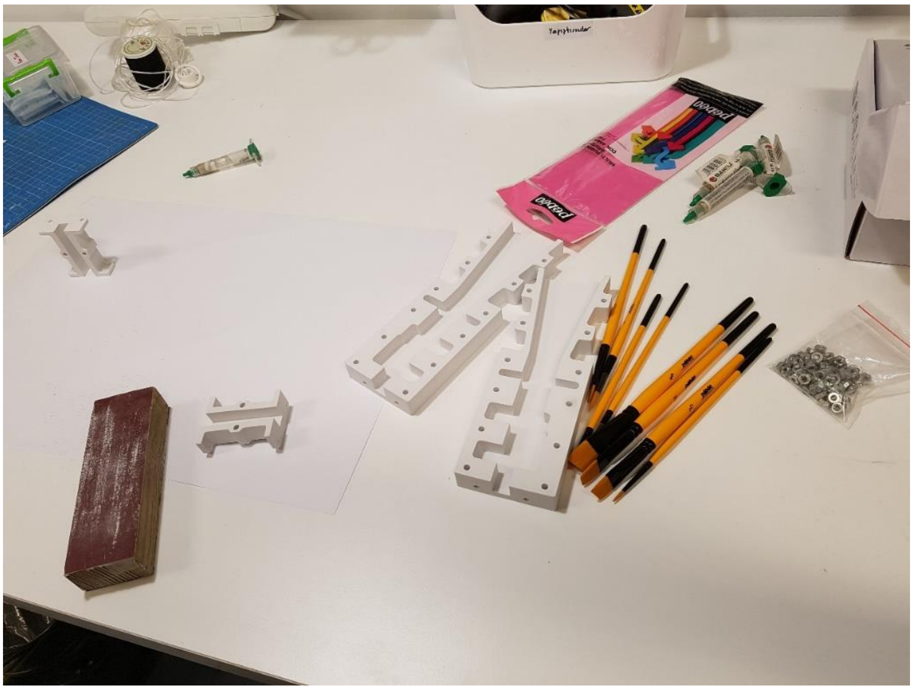

Figure 4.10: All 3D printed components of fabricated mode converter

Baku BK-426 (Figure 4.11) silver conductive paint is chosen as conductive paint solution because it was inexpensive, and its sheet resistance was low enough (less than 0.1 ohm/square @ 1 mil). It has minimum thickness 12.5 µm so one-layer paint is sufficient for our purpose (skin depth of pure silver at 10 GHz is 0.6338 µm). Its curing time is 5 minutes at 120 °C.

Figure 4.11: Baku BK-426 conductive paint

To test the performance of this conductive paint at 10 GHz, the rectangular waveguide test piece shown in Figure 4.12 are 3D printed and painted with this conductive paint. Figure 4.13 shows the painting process of this component with a brush. After painting process, paint is curing with heat for 5 minutes at 120 °C, and Figure 4.14 shows this curing process with heat gun. After curing process, initial conductivity and short circuit tests are done with multimeter and Figure 4.15 shows the conductivity testing process. Figure 4.16 shows the final form of this waveguide testing piece.

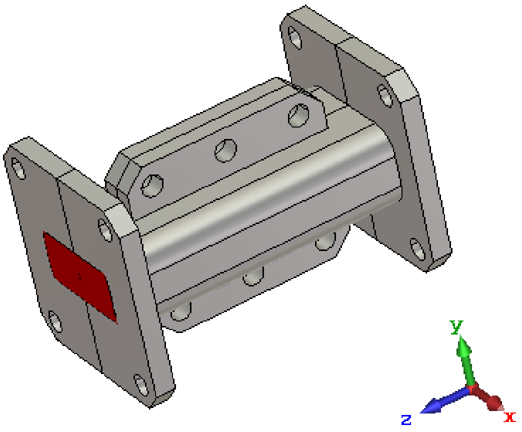

Figure 4.12: Rectangular waveguide test piece

Figure 4.13: Painting process of test piece

Figure 4.14: Curing the paint with heat gun

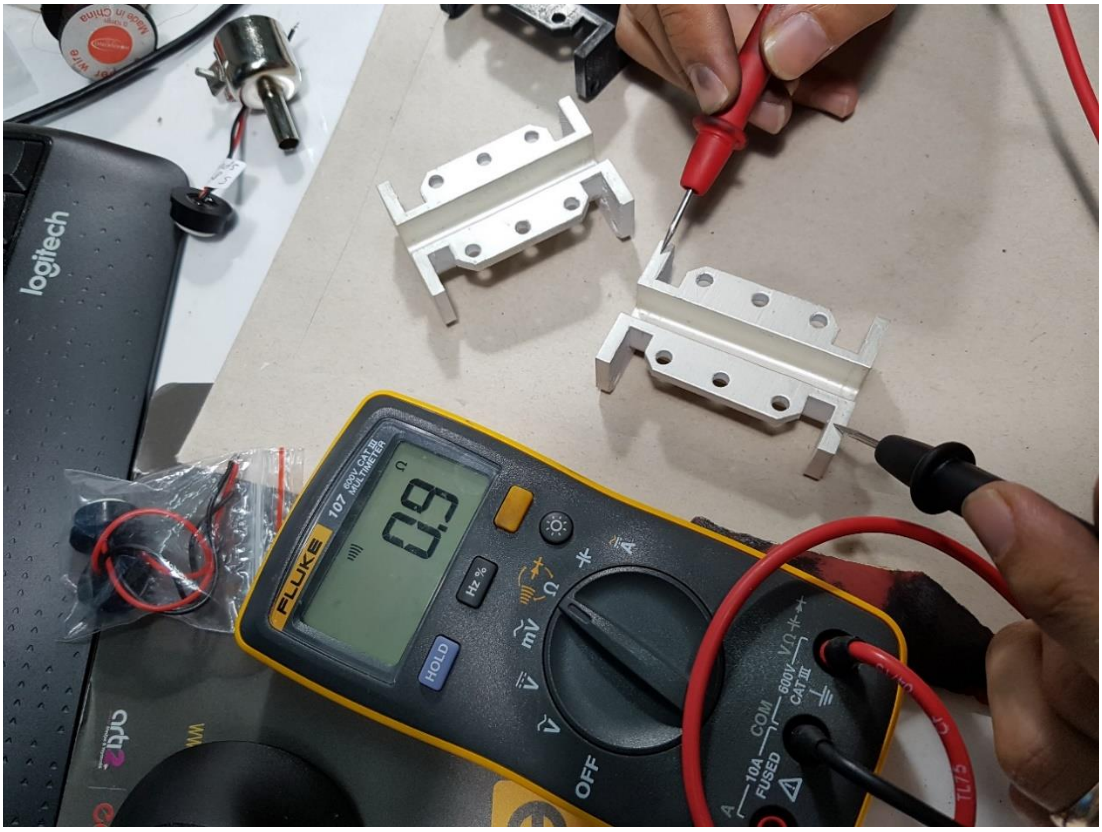

Figure 4.15: The conductivity test using multimeter

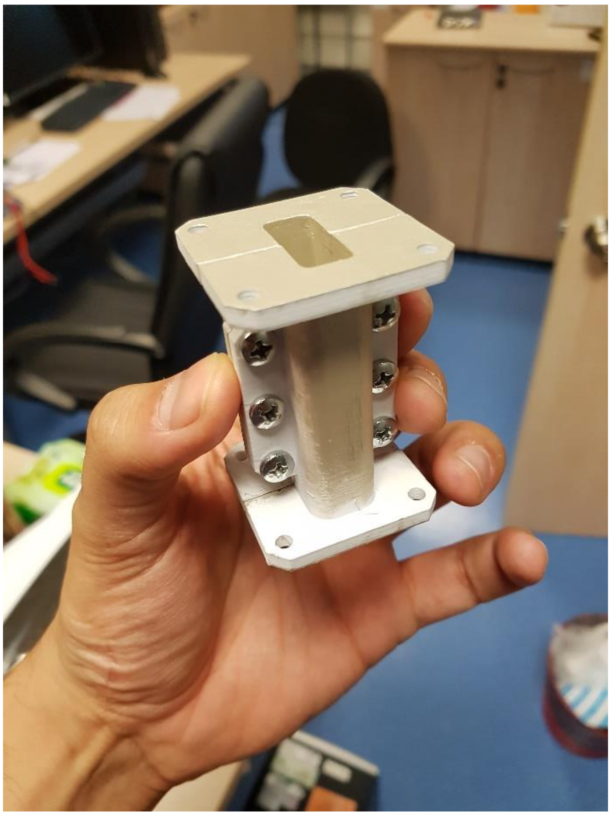

Figure 4.16: Final form of waveguide test piece

The insertion loss and return loss of this waveguide test piece (Figure 4.16) is measured by using Network Analyzer between 8-12 GHz to test the performance of conductive paint and this waveguide manufacturing technique. Figure 4.17 shows the S parameter results measured by Network Analyzer and Figure 4.18 shows the measurement setup. There is only -0.11 dB insertion loss in this test piece. This is due to both 3D printing fabrication technique and loss of conductive paint. As it can be seen, this fabrication technique and conductive paint introduces negligible loss, so this paint can be used to paint 4 components of fabrication model of selected 5 step TE_{10} to TE_{11}+TM_{11} mode converter.

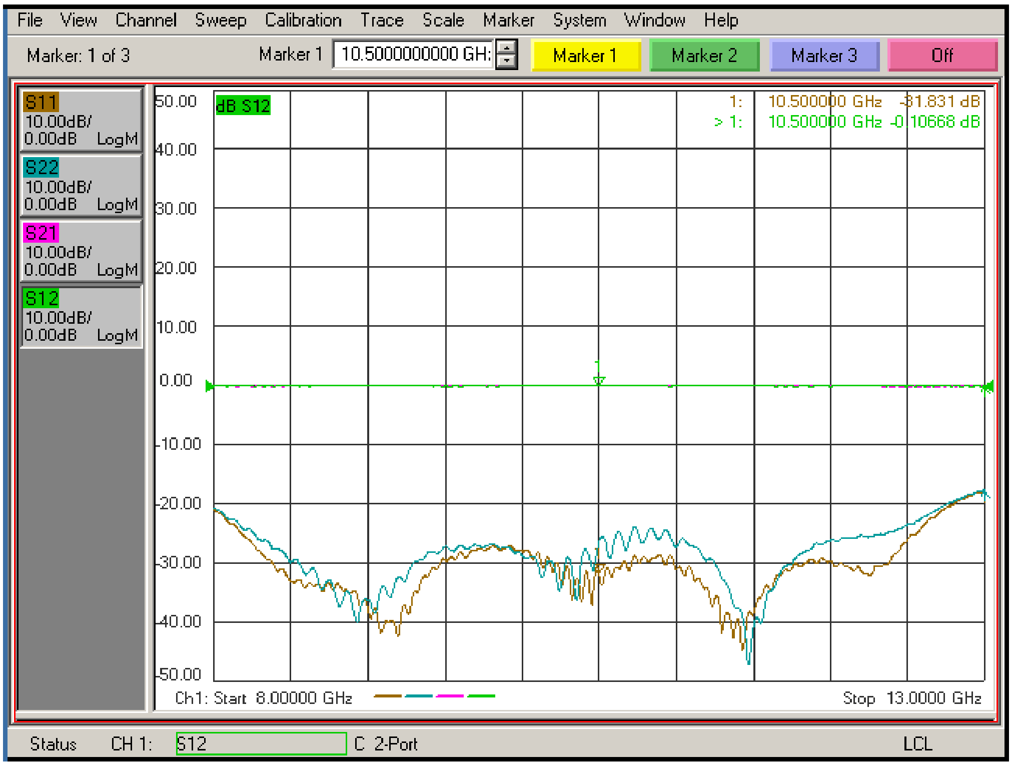

Figure 4.17: S parameter results of waveguide test piece

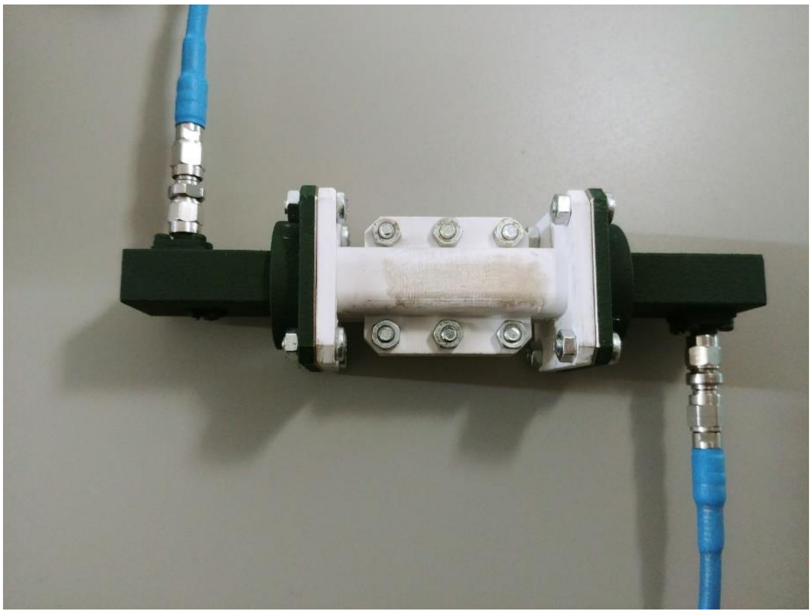

Figure 4.18: Measurement setup

After the good performance of conductive paint is proven, the 3D printed components of fabrication model (Figure 4.10) is painted with brush and then they are cured with heat gun. Figure 4.19 shows two of these components after curing process. Figure 4.20 shows the final assembled version of this mode converter.

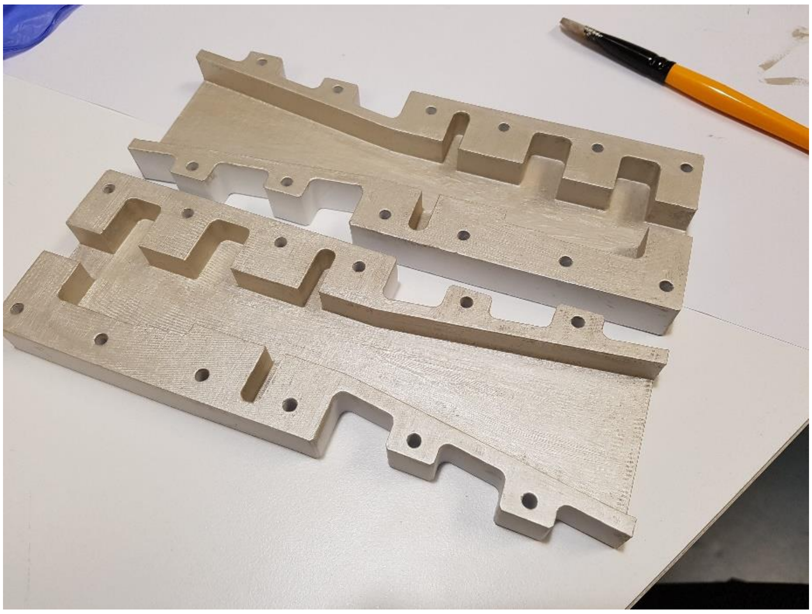

Figure 4.19: Two of the components of fabricated model after curing process

Figure 4.20: Final assembled form of fabricated mode converter (with horn antenna)

This final assembled form of mode converter is firstly connected to Network Analyzer to measure S parameter result. Then it is connected to AUT tower of spherical nearfield system to measure its radiation pattern. Figure 4.21 shows the spherical nearfield (SNF) measurement configuration when this fabricated model is connected to AUT tower of SNF system.

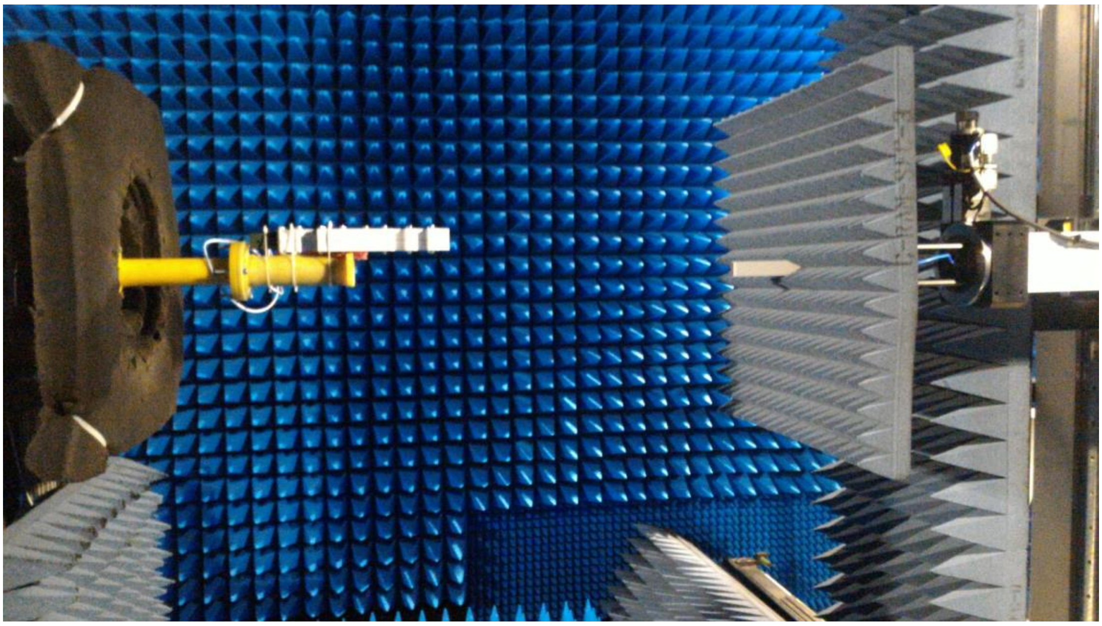

Figure 4.21: SNF measurement configuration when the fabricated model is connected to AUT tower of SNF system

The S parameter measurement result and radiation pattern measurement results of this fabricated model is given in section 4.5. In addition, comparison of measurement and simulation results of this fabricated model is also given in section 4.5.

4.5. Comparison of Measurement and Simulation Results

After fabricated mode converter is connected to Network Analyzer and its S parameter is measured, measurement result is saved as a touchstone file. S parameter simulation result of this converter is also taken from CST Microwave Studio® software. Then by using MATLAB®, these two results are drawn on top of each other and they are shown in Figure 4.22. As it can be seen from this figure, simulation and measurement S parameter results are very close to each other. There are two almost equal notches in simulation S parameter result at 9.8 GHz and 10.2 GHz. These two notches can also be seen in measurement S parameter result at 9.8 and 10.2 GHz, but notch depth at 9.8 GHz is a little bit deeper than simulation result and notch depth at 10.2 GHz is a little bit lesser than simulation result.

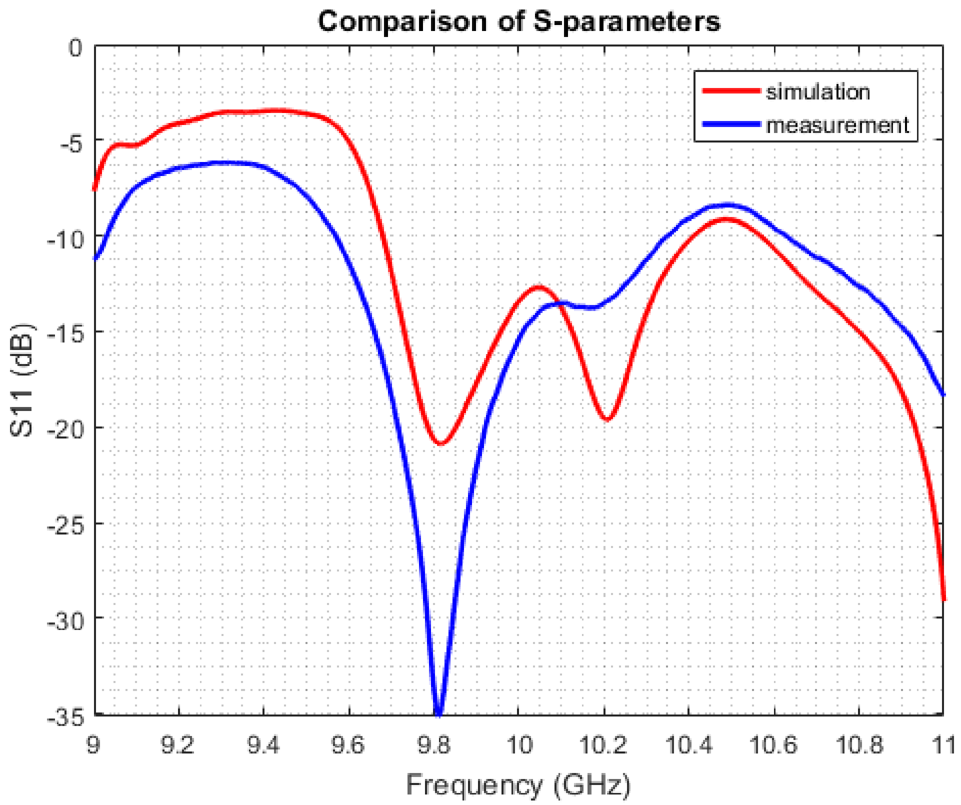

Figure 4.22: Comparison of simulated and measurement S parameter result of fabricated TE_{10} to TE_{11}+TM_{11} mode converter

The radiation patterns of fabricated TE_{10} to TE_{11}+TM_{11} mode converter are measured in the nearfield chamber between 10-10.2 GHz with 0.05 GHz steps. The measured elevation radiation patterns and their respective simulation elevation radiation patterns are drawn on top of each other by using MATLAB software and they are given in Figure 4.23, Figure 4.24, Figure 4.25, Figure 4.26 and Figure 4.27.

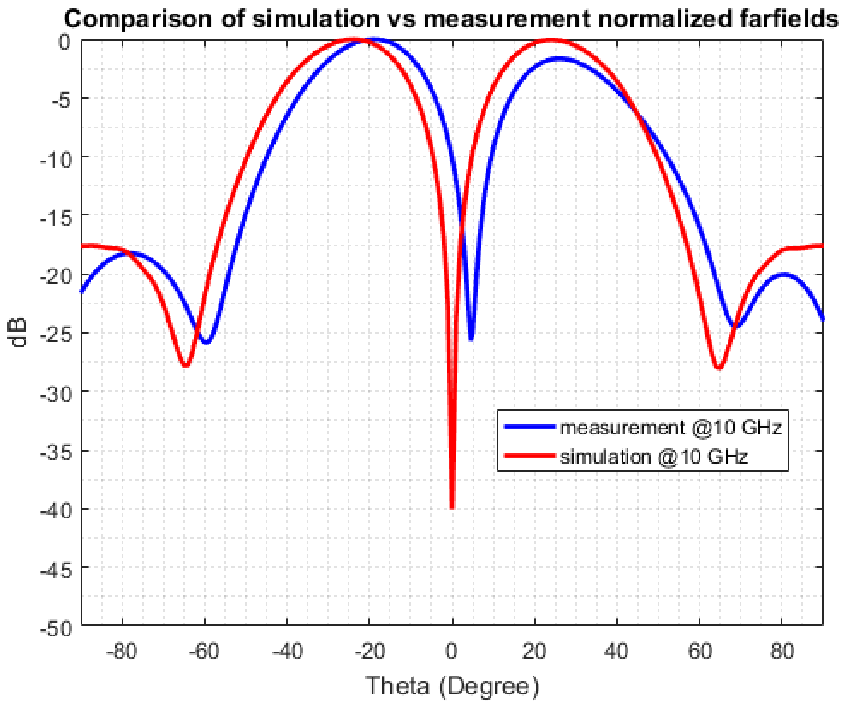

Figure 4.23: Comparison of elevation radiation patterns at 10 GHz

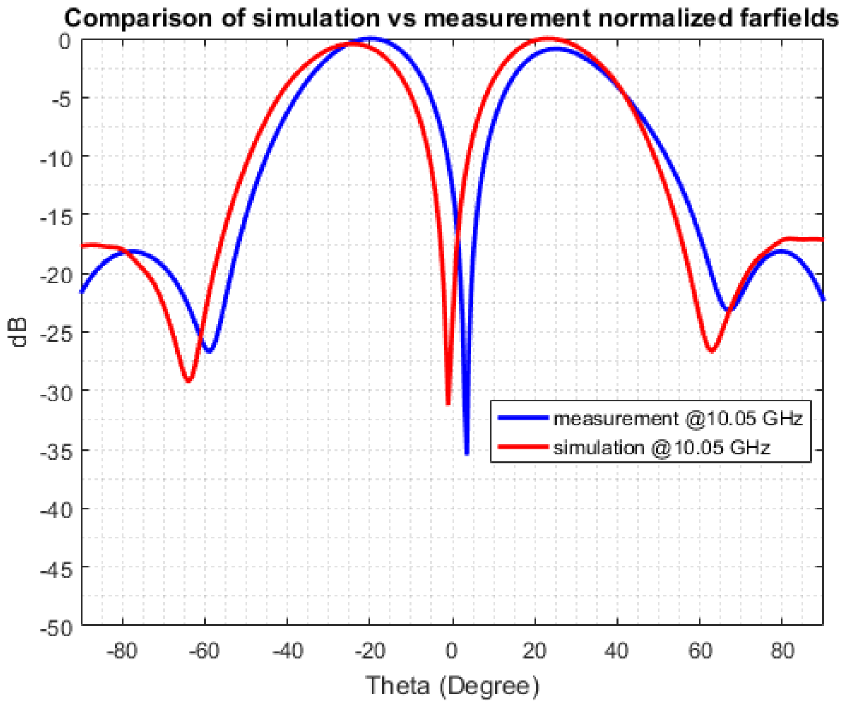

Figure 4.24: Comparison of elevation radiation patterns at 10.05 GHz

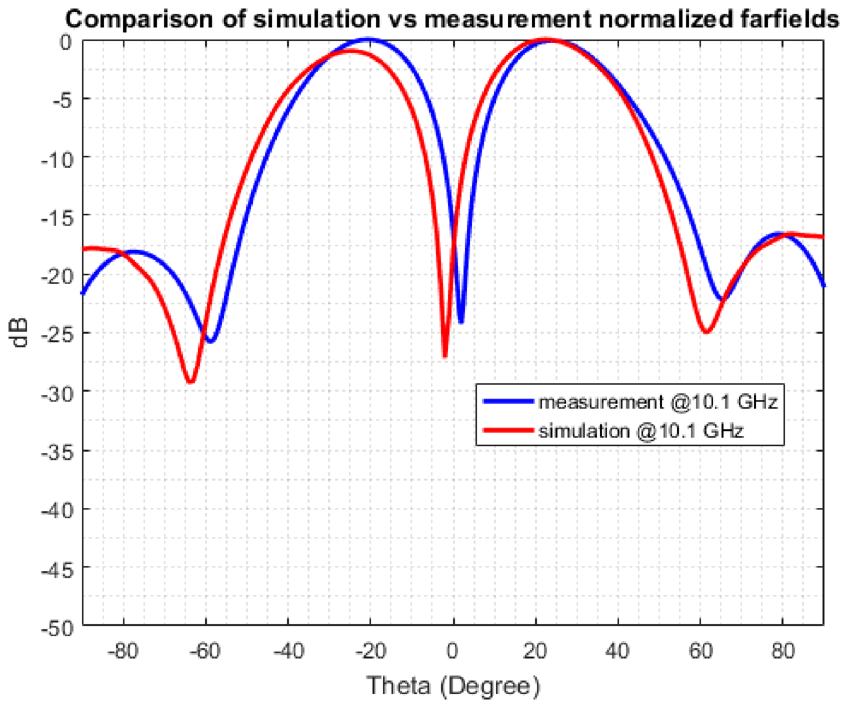

Figure 4.25: Comparison of elevation radiation patterns at 10.1 GHz

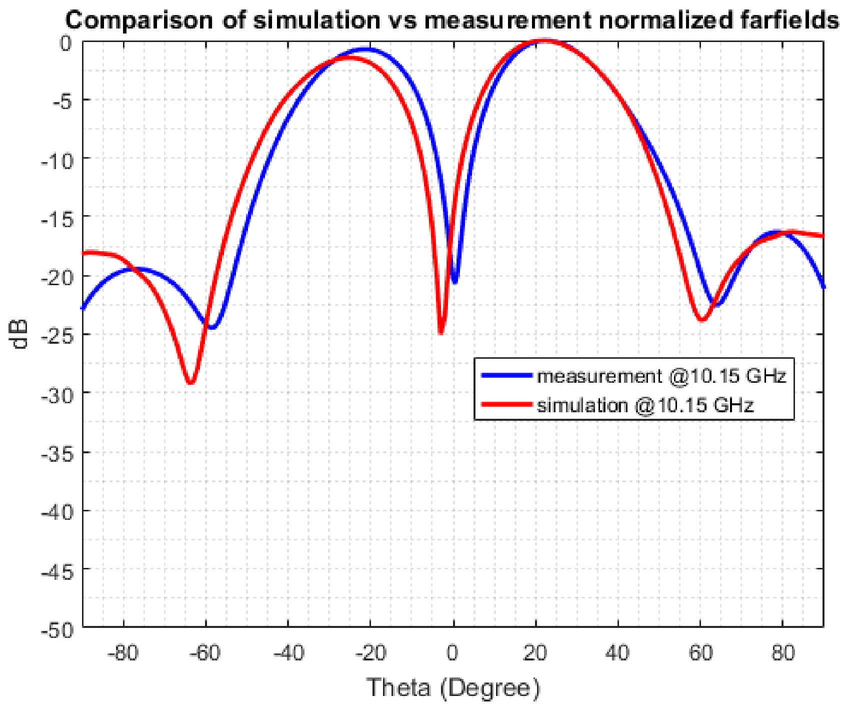

Figure 4.26: Comparison of elevation radiation patterns at 10.15 GHz

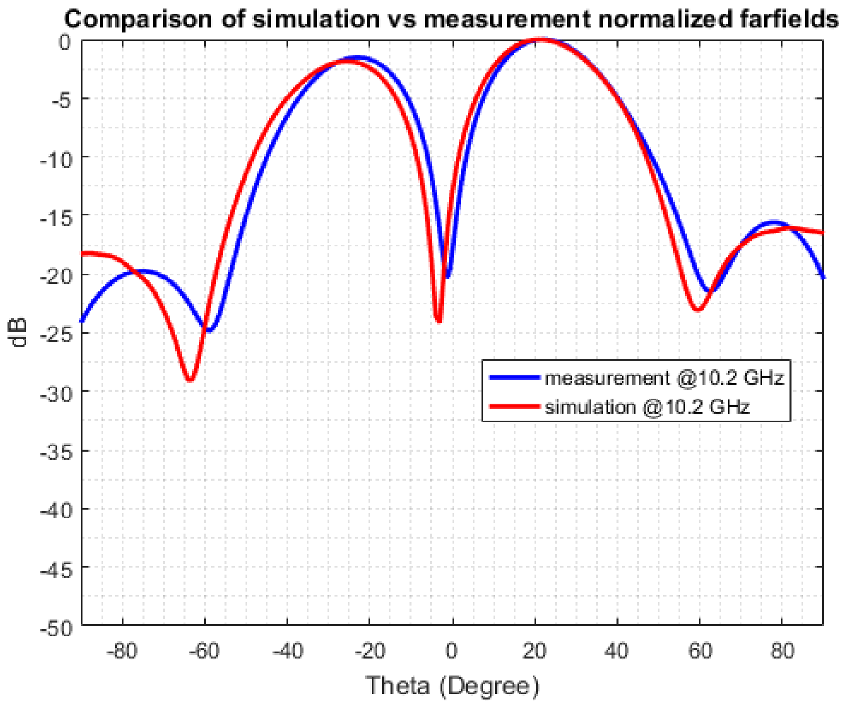

Figure 4.27: Comparison of elevation radiation patterns at 10.2 GHz

As it can be seen from Figure 4.23, the simulation elevation radiation pattern has two equal main lobes as expected. However, there are 1.65 dB difference between main lobes of measurement elevation radiation patterns. The reason for this as follows: when designing this mode converter, the difference $S2(TM_{11}),1(TE_{10})$- $S2(TE_{11}),1(TE_{10})$ is set to 6.57 dB at fc = 10 GHz as optimization goal in order to create ideal elevation difference radiation pattern at 10 GHz (it can be seen in Figure 4.2). However, due to fabrication process, the frequency when this ideal mode combination ratio is obtained is shifted towards higher frequency (towards 10.1 GHz). Since the mode combination ratio is slightly different than ideal combination ratio at 10 GHz, there is 1.65 dB difference between the maximum main lobe gains of measured elevation difference radiation pattern. At 10.05 GHz, this gain difference becomes smaller (0.89 dB), and finally at 10.1 GHz two equal main lobes are obtained in measurement elevation radiation pattern (when $S2(TM_{11}),1(TE_{10})$- $S2(TE_{11}),1(TE_{10})$ = 6.57 dB). As a result, one can say that pattern-wise ideal operating frequency (center frequency, fc) is shifted 100 MHz towards upper frequencies. Simulation elevation radiation pattern at 10 GHz and measurement elevation radiation pattern at 10.1 GHz are drawn on top of each other in Figure 4.28.

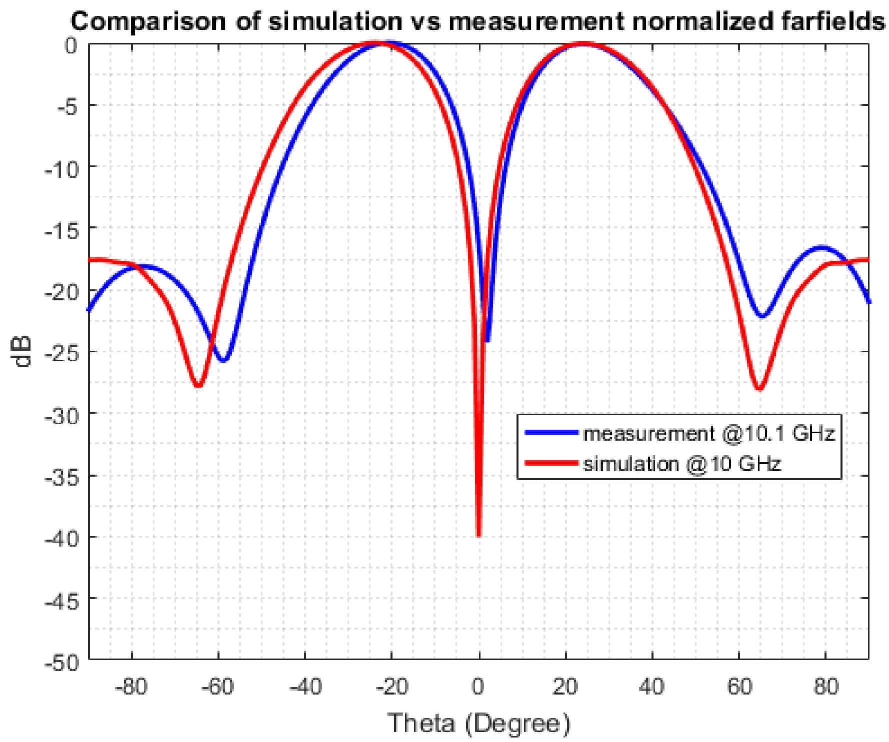

Figure 4.28: Comparison of elevation radiation patterns where ideal elevation difference radiation patterns are obtained

In conclusion, as it can be seen from simulation and measurement results, the performance of CST Microwave Studio® and the fabrication process is verified because simulation and measurement results are very close to each other. Since we obtained these very close performance results for one of the problematic mode converters designed in this thesis (in terms of converter complexity and bandwidth as explained before), the other mode converter designs would also work as intended if they were fabricated by the same fabrication process.

CHAPTER 5

CONCLUSION

5.1. Summary

Monopulse radars are widely used due to their ability to find target's location with only single pulse. Conventional waveguide monopulse antenna consists of antenna array and comparator (feeding) network to create required monopulse radiation patterns and it radiates fundamental TE_{10} mode with different array factors to create monopulse radiation patterns. Alternative way for generating these patterns is to use only one radiator and radiating different waveguide modes to generate different monopulse radiation patterns by the help of mode converters. In this thesis, 3 structures for mode generation (discrete stepped, bend, corner) are investigated to see if they are capable of convert fundamental TE_{10} mode to required waveguide modes.

The first structure is discrete stepped mode converter. This structure has the most number of parameters to be optimized, therefore their design takes the most time. Their S parameter changes rapidly if the number of steps is few. When the number of steps is increased, operating bandwidth increases, and S parameter response becomes smoother. The only satisfactory result to convert TE_{10} mode to TE_{10}+TE_{30} mode combination is obtained with this structure. In addition, as in section 3.1.5, mode converter can be designed to radiate one mode at one frequency and the other mode at other frequency.

The second structure is bend mode converter. This structure has the least number of parameters to be optimized (only two), so mode converter design of this kind takes the least time. Its operating bandwidth is wide, and the structure is symmetrical.

The last structure is corner mode converter. The number of parameters to be optimized is more than bend converter and less than discrete stepped mode converter. This converter is the most compact waveguide mode converter that is investigated in this thesis. It also has wide operating bandwidth.

One of the designs given in this thesis is fabricated. The selection of which design to be fabricated is done by considering their S parameter and the difficult of conversion operation. The structure which is thought to be one of the most problematic is selected and fabricated by using Zortrax M200 3D printer. 3D printer fabrication makes manufacturing process inexpensive and it makes the fabricated mode converter lightweight. The fabricated mode converter is painted with Baku BK-426 conductive silver paint to make its surface conductive. Both the design and fabrication processes are validated by S parameter and radiation pattern measurements.

5.2. Future Work

In this thesis, it is focused on designing rectangular mode converter for generating monopulse radiation patterns. In order to use these converters with one radiating element, the output of these mode converters can be tried to couple to common single horn antenna to obtain whole multimode monopulse fed as a future work.

The mode converter designs in this thesis can also be tried to combine with feeding network and antenna array to hybrid solution for overcoming beam width optimization problem as a future work.

APPENDIX A

INFORMATION ABOUT CST MICROWAVE STUDIO® SOFTWARE

CST Microwave Studio® is used for 3D simulations of designed mode converters and illustrations of some of the concepts in other chapters. In this chapter some of the properties of this 3D simulation software are mentioned.

A.1. General Features of CST Microwave Studio®

CST Microwave Studio® is one of the most preferred electromagnetics simulation software in electromagnetics engineering. The several reasons for why this software is chosen as a main design software can be listed as follows:

- It has a user-friendly interface and it is easy to use and learn for new users.
- Its 3D drawing tools are almost as capable as 3D CAD tools.
- It allows importing and exporting different types of physical models (from EDA models to CAD models).
- It has a very large material library.
- It has different types of solvers for different purposes (to be explained later in this section). These solvers use different accurate and efficient numerical methods and different meshing types for these methods. Thanks to this property, the software can efficiently and accurately simulate broadband and narrowband, electrically large or small, simple or complex problems.
- It provides HPC (high performance computing) and GPU (graphics processing unit) accelerated computing options for simulating complex and/or electrically large problems. These options also provide speed increase for regular problems.

- Measured data of interested problem can be imported into software and realistic simulation results can be obtained. This imported data can be s parameter of a device, dielectric properties of a material, nearfield measurement data of antenna etc.
- It has different local and global optimizers. More information about its optimizers will be discussed in detail later in this chapter.
- It can show active and regular S parameter of the interested device.

The software has different types of monitor for visualizing and informing user about different aspects of the interested problem. Some of the its frequently used monitors and their uses are:

- E-Field: The electric field vectors within the interested problem volume can be stored and visualized.
- H-Field and Surface current: The magnetic field vectors and the surface currents can be visualized using this monitor.
- Power flow: The Poynting vector of the electromagnetic field can be stored using this monitor.
- Current density: In the presence of electric losses, the currents inside of these lossy materials are showed by this type of monitor.
- Far field/RCS: For simulating far field of the antenna or simulating RCS of a platform.
- Field source: Near field data of the interested problem can be stored and it can be used in different project.

From above monitor types, E-field and Far field monitors will be used frequently in this thesis. The E-field monitor will be used for setting optimization goal for designed stepped mode converters and checking if the outcomes of these optimization processes are triumphant or not. Far field monitor will be used for checking if the waveguide modes, that are arising from the output port of the mode converters, is really radiates desired monopulse far field patterns

A.2. Solvers and Their Properties

CST Microwave Studio® software embodies different solver for different types of problems. The solvers and their main purposes of usage are as follows [96, p. 9]:

- Transient Solver – general purpose (for obtaining S parameter of interested problem)
- Frequency Domain Solver – general purpose (for obtaining S parameter of interested problem)
- Integral Equation Solver – electrically large structures (e.g. electrically large dish antenna), RCS (Radar Cross Section) calculations of different problems
- Asymptotic Solver – platform simulations of antennas, RCS calculations of different platforms
- Eigenmode Solver – resonant structures (e.g. cavities)
- Multilayer Solver – planar structures

Properties of above solvers are given briefly below:

Transient Solver [97]:

Transient solver uses hexahedral meshes as the mesh type. It is usually used for low resonant high frequency applications. The main objective to get S parameter results of the considered problem and to design components using optimization and parameter sweep tools of the CST Microwave Studio® software. The interested problem should have electrically small or medium size for this solver to be efficient. This solver is very good choice if the interested problem is one of the following type of problem: connectors, transmission lines, filters, antennas, waveguide structures etc. By using this solver, user can obtain whole broadband frequency response of the simulated device in a single simulation run. Transient solver uses the Finite Integration Technique (FIT) together with the Perfect Boundary Approximation (PBA, allowing accurate modeling of curved structures) and the Thin Sheet Technique (TST, improves the modeling of thin perfectly electric conducting sheets), owing to these, it can generate very accurate simulation results. Detailed information about these techniques is out of scope of this thesis, but it can be found in [98], [99], [100] & [101].

Frequency Domain Solver [102]- [103]:

Just as transient solver, main purpose of using frequency domain solver to obtain S parameter of the simulated device and design components by using optimization and parameter sweep tools. It uses tetrahedral mesh type. Fields are transformed into frequency domain and they are described by phasors. Due to this process, for each frequency sample in the simulation settings, software needs to set up and solve new equation sets. As a result, as the number of frequency samples increases, the simulation time increases linearly. This solver is the best choice and the fastest when there are only few interested frequency samples in the simulation. When there are only few frequency samples in which the simulation results are required and when the simulated problem is not electrically very large (when the mesh number is moderate), frequency solver may be good and faster alternative to transient solver of CST Microwave Studio® software.

Eigenmode Solver [104]- [105]:

Eigenmode Solver is used when the simulated problem is very resonant and lossless. It is used to obtain electromagnetic field patterns (eigenmodes) and their frequencies of such structures. Poles of strongly resonant components can be determined very efficiently using this solver. The first several frequencies in which the electromagnetic fields may be present in the simulated device and their field patterns in these frequencies are obtained using this type of solver. Since this solver requires different license than the writer of this thesis had, this solver left out of consideration when choosing solvers for designing rectangular waveguide mode converters mentioned in previous chapter.

Integral Equation Solver [106]- [107]:

Integral equation solver is used to simulate electrically large problems (e.g. reflector antennas) and to obtain their performances. It can also be used for RCS (Radar cross section) calculations. This solver uses surface meshes, as a result only the objects boundaries (not all the volume, only the surfaces) in the interested problem is meshed.

This leads to fewer number of unknowns to found than volume meshing techniques. This solver uses Multi Level Fast Multipole Method (MLFMM) [108].

Multilayer Solver [109]:

This solver exists for 3D simulations of planar structures. It uses Method of Moments (MoM). By using this solver, multilayer planar problems can be analyzed correctly and quickly.

Asymptotic Solver [110]:

This solver is used instead of Integral solver when the problem size is very large and using Integral solver becomes inefficient. This solver uses rat tracing methods (shooting and bouncing rays, SBR). Main application areas of this solver are RCS calculation and antenna platform placement and performance analysis.

A.3. Chosen Solvers for This Thesis, Reasons, Chosen Solver Usage Methodology

The problem types dealt with in this thesis are the rectangular waveguide mode converters which are based on rectangular waveguide structures. Their largest dimensions are only a few wavelengths (less than 10 lambda), therefore they are electrically small. In addition, there are only a few frequencies in which these mode conversion operations are wanted to be obtained. As a result, both frequency domain solver and transient solver seem to be suitable for the solver choice. Indeed, both frequency domain solver and transient solver used together to design desired rectangular waveguide mode converters that will be presented in next chapters.

The general solver usage methodology was as follows: Initially, all parts of waveguide mode converters modelled as vacuum in CST Microwave Studio® and the background material chose as PEC (Perfect Electric Conductor). Since only a few frequencies in which these mode conversion operations were wanted to be obtained, frequency domain solver was chosen as a starting solver. By using this solver, the mode converter design came to maturity level. Then metallic model (which has PEC walls with some thickness and background material is vacuum this time) is simulated with transient solver to see broadband response of the designed mode converters. This method was the fastest way of reaching final designs. In addition, to see if the mode components at the output of the mode converters radiates desired radiation patterns, horn is connected after some of the mode converter designs and whole system is simulated using transient solver and far field radiation monitor. This solver usage methodology will be clearer in the next chapters.

A.4. Optimization Algorithms of CST Microwave Studio® Software

There are two main types of optimization algorithms in CST Microwave Studio® software: Local optimizers and global optimizers.

Local optimizer used when the initial parameter set is close to optimum values. If the case is so, by using local optimizers optimum parameters values are obtained with less number of trials than global optimizers, so they are faster than global optimizer algorithms in that case. They are usually used when fine tuning of parameters of the design problem. Local optimization algorithms become inefficient when initial set of values of parameters of design problem is far away from optimum values and/or there are large number of parameters to be optimized.

The global optimizers look for the optimum set of parameter values in whole parameter space. Global optimization algorithms are used when there are large number of parameters to be optimized and/or initial set of parameter values are far away from the optimum values. If that is the case, they are faster and more efficient than local optimization algorithms.

There are seven optimization algorithms that can be used in CST Microwave Studio® [96]. Four of them are local optimizers and the rest of them is global optimizers. These seven optimization algorithms are given below:

Local optimization algorithms:

- Trust Region Framework
- Nelder-Mead Simplex Algorithm
- Interpolated Quasi-Newton

- Classic Powell

Global optimization algorithms:

- Genetic Algorithm
- Particle Swarm
- Covariance Matrix Adaptation Evolutionary Strategy (CMA-ES)

The choice of the required optimization algorithm can be decided using the Figure A.1 [111]:

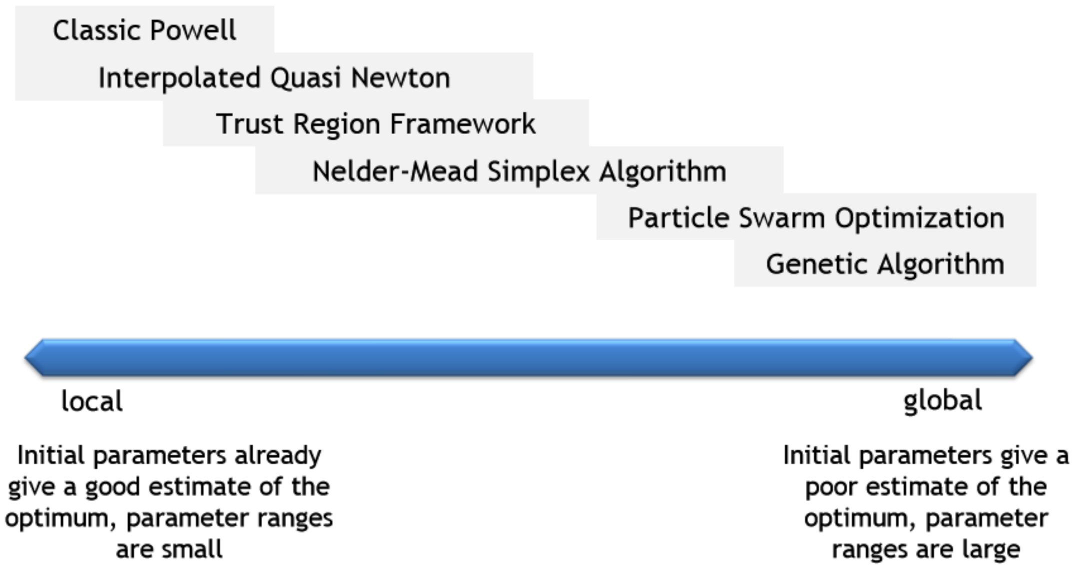

Figure A.1: Choice of optimization algorithm depending on initial parameters

Brief information about these optimization algorithms can be given as follows [111]-[112]- [113]- [114]- [115]:

<u>Classic Powell:</u> It uses line search for each parameter. Therefore, when there is only one variable in the optimization problem, Classic Powell algorithm should be chosen to have fast and accurate optimization result. Figure A.2 illustrates this algorithm process.

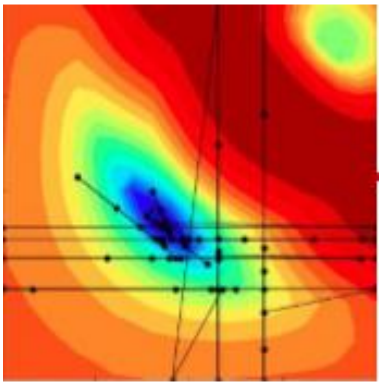

Figure A.2: Visualization of Classic Powell algorithm process

Interpolated Quasi Newton: When there is need for local optimizer for a computationally demanding problem, this algorithm should be preferred. For each parameter, the search direction is determined by discretely sampling the parameter ranges. Then 3D electromagnetic simulations are performed for each of these sample points. In other words, numerical calculations of the problem are only done in these discrete samples. For all other combinations and intermediate values of parameters, the solutions are found by interpolating primary data (not by numerical calculations). After each optimization pass, the optimizer verifies interpolated (predicted) performance by applying numerical solver. This optimization process is faster than Classic Powell but less accurate. Figure A.3 illustrates this algorithm process.

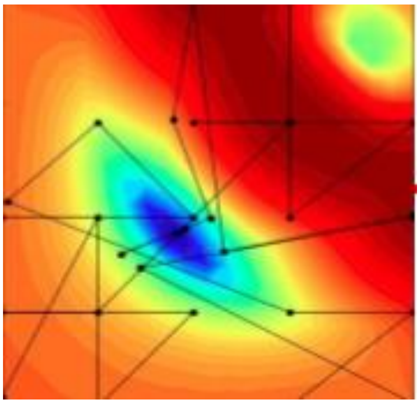

Figure A.3: Visualization of Interpolated Quasi Newton algorithm process

Trust Region Framework: Trust Region Framework is the most powerful and capable local optimization algorithm that CST Microwave Studio® offers. This optimizer creates a "trust" region around initial set of parameters. Then inside this region, optimizer predicts the optimum point and goes to that point. If the error value (depending on optimization goals) is smaller in this predicted point, optimizer moves this point further in that direction until error increases and take last minimum error point as new center of a new trust region with reduced trust region radius. If the predicted point does not yield less error value, optimizer reduces its trust region radius and predicts new optimum point. The optimization process continuous like this until the trust region radius or distance to the next predicted optimum point becomes less than the specified optimizer accuracy (it can be change in the setting of this optimizer).

Figure A.4 illustrates this algorithm process.

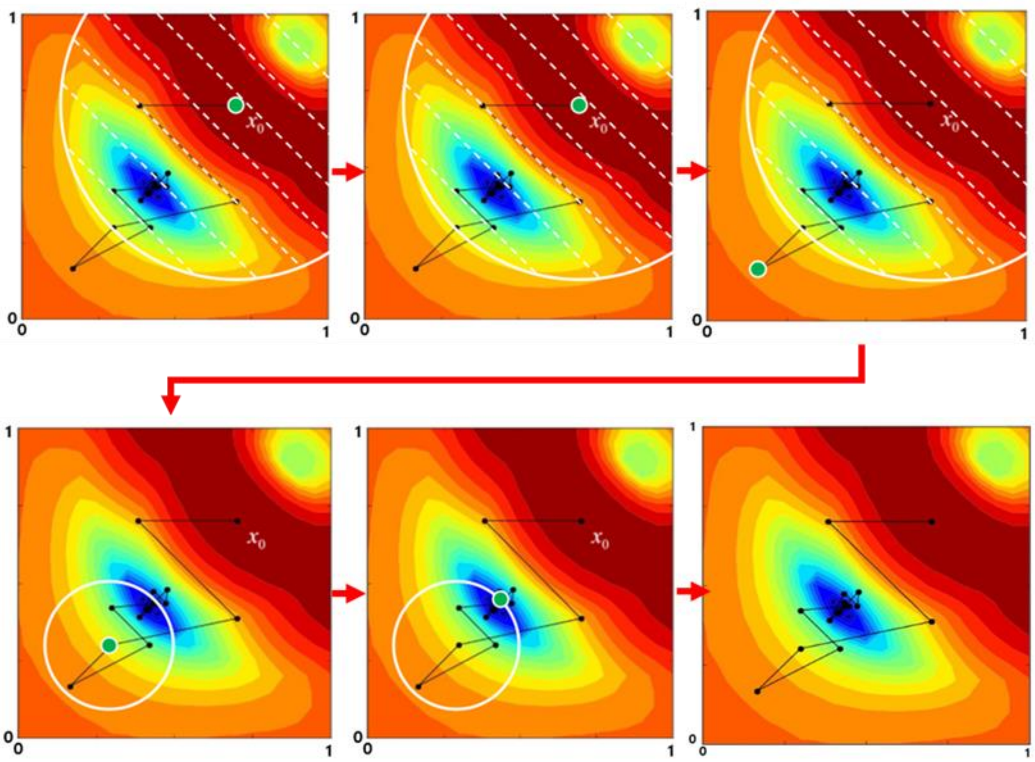

Figure A.4: Visualization of Trust Region Framework algorithm process

Nelder-Mead Simplex Algorithm: This optimizer is based on Simplex optimization method offered by Nelder and Mead ("a simplex method for function minimization").

This optimization algorithm can be good choice if there are a few number of parameters (i.e. less than 5) and initial set of parameters is not very good because Nelder-Mead Simplex Algorithm is less dependent on initial points.

Figure A.5 illustrates this algorithm process.

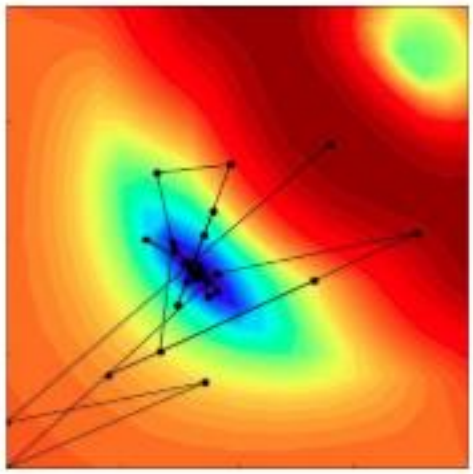

Figure A.5: Visualization of Nelder-Mead Simplex algorithm process

Particle Swarm: This global optimization algorithm is recommended for optimization problems with many parameters. The points in parameter space considered as shifting particles. The particles change their positions in parameter space at each iteration of the optimizer in accordance with both best-known position of each particle which gives minimum error due to that parameter and best position of the whole swarm.

Figure A.6 illustrates this algorithm process.

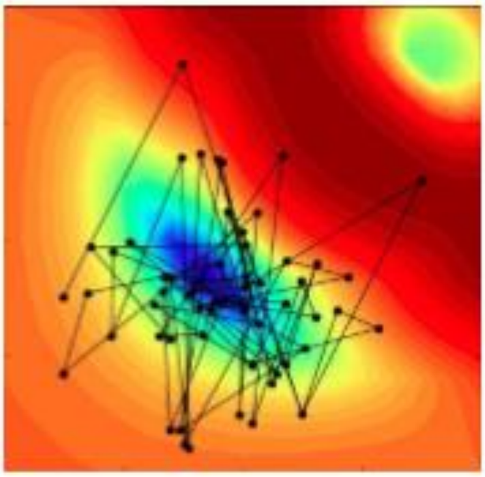

Figure A.6: Visualization of Particle Swarm algorithm process

Genetic Algorithm: This global optimizer is recommended when the number of parameters is very large. Algorithm produces points in parameter space, after that it purifies them through various generations, at each generation random parameter mutation is introduced. After this, at each generation, most appropriate sets of parameters (which give minimum error) are chosen. By doing so, optimizer reaches optimum global parameter set at the end of optimization process.

Figure A.7 illustrates this algorithm process.

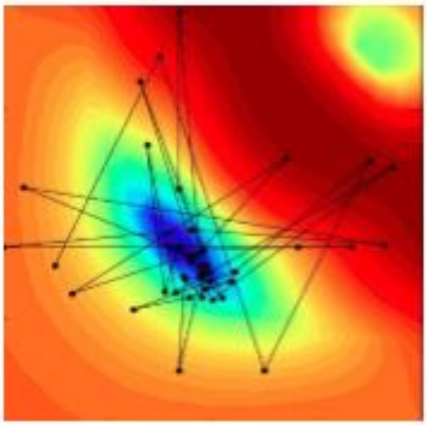

Figure A.7: Visualization of Genetic Algorithm process

Covariance Matrix Adaptation Evolutionary Strategy (CMA-ES): This algorithm can be considered as a fast-convergent global optimizer. This property of the optimizer is result of its ability to recall previous trials, this ability can be used to improve convergence speed of this optimizer. This recalling ability can also be used to bypass local minima optimum points that may be unintentionally found by this optimizer.

A.5. Chosen Optimization Algorithms for Designing Mode Converters

Design process of discrete stepped rectangular waveguide converters requires usage of optimization algorithms (since there are no design formulas). To design these discrete stepped waveguide mode converters, optimization tools and algorithms of CST Microwave Studio® software were used.

Initially Particle Swarm or Genetic Algorithm global optimizers used to bring stepped mode converter designs to some maturity level. Then, when set of parameter values which are very close to optimum values, Trust Region Framework local optimizer was used for fine tuning of parameters. As a result, discrete stepped rectangular waveguide mode converters, which exhibit desired performances, are designed.

REFERENCES

[1] A. I. Leonov, "History of monopulse radar in the USSR," *IEEE Aerospace and Electronic Systems Magazine,* vol. 13, no. 5, pp. 7-13, 1998.

[2] D. K. Barton, "History of monopulse radar in the US," *IEEE Aerospace and Electronic Systems Magazine,* vol. 25, no. 3, pp. 1-16, 2010.

[3] J. Litva, "Theory of conaical-scan radars for low-angle tracking," Communication Research Center, Department of Communications, Canada, 1980.

[4] A. I. Leonov and K. I. Fomichev, "Monopulse Radar," Foreign Technology Division, Ohio, 1970.

[5] D. Barton and S. A. Leonov, Radar Technology Encyclopedia, Norwood: Artech House Inc., 1998.

[6] M. Zhen-qui and C. Wei, "Angle measurement performance analysis and simulation of sum and difference phase-comparison monopulse radar," in *Radar Conference, 2009 IET International*, Guilin, China, 2009.

[7] Microwaves101, "Monopulse Comparator Networks," Microwaves101, 2005. [Online]. Available: https://www.microwaves101.com/encyclopedias/406-monopulse-comparator-networks-microwave-encyclopedia-microwaves101-com. [Accessed 12 November 2017].

[8] C. Wolff, "Monopulse Antenna," Radar Tutorial, [Online]. Available: http://www.radartutorial.eu/06.antennas/Monopulse%20Antenna.en.html. [Accessed 12 November 2017].

[9] Microwaves101, "Monopulse antennas," Microwaves101, [Online]. Available: https://www.microwaves101.com/encyclopedias/monopulse-antennas. [Accessed 12 November 2017].

[10] G. Guinta, L. Lucci, R. Nesti, G. Pelosi, S. Selleri and F. Serrano, "A Comparison between Standard and Crossfeed Monopulse Radars in Presence of Rough Sea Scattering and Ship Movements," *International Journal of Antennas and Propagation,* vol. 2010, no. Article ID 126757, 2010.

[11] H. Guan-Long and Z. Shi-Gang, "Application of 3-D Printing to Fabrication of Highly-Efficient Waveguide-Based Antenna Array with Integrated monopulse Comparator," in *2017 IEEE International Symposium on Antennas and Propagation & USNC/URSI National Radio Science Meeting (AP-S URSI 2017),* San Diego, USA, 2017.

[12] Y. Zhong-Wu, W. Guang-Ming and Z. Chen-Xin, "A Broadband Planar Monopulse Antenna Array of C-band," *IEEE ANTENNAS AND WIRELESS PROPAGATION LETTERS,* vol. 8, pp. 1325-1328, 2009.

[13] Z. Xiong, T. Chuang-Ming, B. jun-Song and P. Wei-Jian, "SIW-Fed Yagi Antenna and Its Application on Monopulse Antenna," *IEEE Antennas and Wireless Propagation Letters,* vol. 13, pp. 1035-1038, 2014.

[14] H. Han-Yai, W. Bing-Zhong, L. Feng and Z. Lu, "A Ka-Band Monopulse Microstrip Antenna Array," in *2008 IEEE MTT-S International Microwave Workshop Series on Art of Miniaturizing RF and Microwave Passive Components,* Chengdu, China, 2008.

[15] N. S. Wong, R. Tang and E. E. Barber, "A Multielement High Power Monopulse Feed with Low Sidelobe and High Aperture Efficieny," *IEEE Transactions on Antennas and Propagation,* Vols. AP-22, no. 3, pp. 402-407, 1974.

[16] Y. Fengwei, X. Xiaobo and L. Yuanyun, "A Novel Monopulse Edge-fed Microstrip Array," in *IEEE 5th International Symposium on Microwave, Antenna, Propagation and EMC Technologies for Wireless Communications (MAPE)*, Chengdu, China, 2013.

[17] Y. Fengwei, Z. Rujiang, L. Yuanyun, S. Yuanbo, X. Xiaobo and S. Zhiwei, "Design of a Side-fed Monopulse Microstrip Radiator Array," in *5th Global Symposium on Millimeter Waves*, Harbin, China, 2012.

[18] E. Bayanmunkh, B. Jae-Hoon, C. Eun-Jong and A. Bierng-Chearl, "Design of a W-Band Monopulse Comparator Based on E- and H-Plane Waveguide Couplers," in *IEEE 11th AnnualWireless and Microwave Technology Conference (WAMICON)*, Melbourne, FL, USA, 2010.

[19] H. Miyashita and T. Katagi, "Four-point fed radial line planar antenna array for monopulse tracking operation," in *Antennas and Propagation Society International Symposium, 1993. AP-S. Digest*, Ann Arbor, MI, USA, USA, 1993.

[20] Q. Song-song, L. Xing-guo and W. Ben-qing, "Ka band Cassegrain monopulse antenna fed by tapered rod antennas," in *8th International Symposium onAntennas, Propagation and EM Theory (ISAPE 2008)*, Kunming, China, 2008.

[21] N. Yang, C. Caloz and K. Wu, "Monopulse comparator with frequency-independent delta-channel nulls for high-resolution tracking radar," *Electronics Letters*, pp. 339-340, 3 March 2011.

[22] L. Zhen-Guo and G. Yong-Xin, "Monopulse Fabry-Perot resonator antenna," in *2013 Proceedings of the International Symposium on Antennas & Propagation (ISAP)*, Nanjing, China, 2013.

[23] Y. Cheng, W. Hong and K. Wu, "Multimode substrate integrated waveguide H-plane monopulse feed," *Electronics Letters,* vol. 44, no. 2, pp. 78-79, 17 January 2008.

[24] K. S. Ang, Y. C. Leong and C. H. Lee, "A Wide-Band Monopulse ComparatorWith Complete Nulling in All Delta Channels Throught Sum Channel Bandwidth," *IEEE TRANSACTIONS ON MICROWAVE THEORY AND TECHNIQUES,* vol. 51, no. 2, pp. 371-373, 2003.

[25] P. W. Hannan, "Optimum Feeds for All Three Modes of a Monopulse Antenna I: Theory," *IRE Transactions on Antennas and Propagation,* vol. 9, no. 5, pp. 444-454, 1961.

[26] P. Wade, "Parabolic Dish Antennas," [Online]. Available: http://www.qsl.net/n1bwt/chap4.pdf. [Accessed 13 November 2017].

[27] L. Ricardi and L. Niro, "Design of a twelve-horn monopulse feed," in *1958 IRE International Convention Record*, New York, USA, 1958.

[28] P. Hannan and P. Loth, "A monopulse antenna having independent optimization of the sum and difference modes," in *1958 IRE International Convention Record*, New York, USA, 1958.

[29] K. M. Lee and R. -S. Chu, "Design and analysis of a multimode feed horn for a monopulse feed," *IEEE Transactions on Antennas and Propagation,* vol. 36, no. 2, pp. 171-181, 1988.

[30] P. J. B. Clarricoats and R. D. Elliot, "Multimode corrugated waveguide feed for monopulse radar," *Microwaves, Optics and Antennas, IEE Proceedings H,* vol. 128, no. 2, pp. 102-110, 1981.

[31] S. Ghosh and C. Lee-Yow, "A multimode monopulse feed with equalized gain in sum and difference patterns," in *Antennas and Propagation Society Symposium 1991 Digest*, London, Ontario, Canada, 1991.

[32] S. Ghosh, "A New Monopulse Feed System for Increased Tracking Accuracy of Radars," in *21st European Microwave Conference*, Stuttgart, Germany, 1991.

[33] T. Vu and N. Hien, "A New Type of High-Performance Monopulse Feed," *IEEE Transactions on Antennas and Propagation,* vol. 21, no. 6, pp. 855-857, 1973.

[34] U. Lidvall, M. Persson and G. Larsson, "Broadband Multimode Feed for Monopulse Tracking Antenna," in *18th European Microwave Conference*, Stockholm, Sweden, 1988.

[35] R. J. Liu and W. B. Don, "Design and Anasysis of 3mm Multimode Monopulse Feed," in *International Conference on Microwave and Millimeter Wave Technology*, Builin, China, 2007.

[36] A. Tribak, A. Mediavilla, K. Cepero and J. L. Cano, "Highly efficient monopulse tracking feed subsystem for unmanned aerial vehicle," in *41st European Microwave Conference*, Manchester, UK, 2011.

[37] A. M. El-Tager, H. N. Ahmad and M. Magdi Darwish, "Multimode Antenna Feed System for an X-Band," in *2009 IEEE Radar Conference*, Pasadena, CA, USA, 2009.

[38] H. Bayer, A. Krauss, R. Stephan and M. A. Hein, "Multimode monopulse tracking feed with dual-band potential for land-mobile satellite communications in Ka-band," in *European Conference on Antennas and Propagation (EUCAP)*, Rome, Italy, 2011.

[39] T. Vu, "On high-performance monopulse feed using corrugated waveguide," in *Antennas and Propagation Society International Symposium*, Boulder, CO, USA, 1973.

[40] P. A. Jensen, "A low-noise multimode Cassegrain monopulse with polarization diversity," in *Northeast Electron. Res. Mtg.*, 1963.

[41] C. A. Balanis, Advanced Engineering Electromagnetics, 2nd Edition, United States of America: WILEY, 2012.

[42] P. Jarry and J. Beneat, "Appendix 3: Modal Analysis of Waveguide Step Discontinuities," in *Advanced Design Techniques and Realizations of Microwave and RF Filters*, New Jersey, USA, John Wiley & Sons, Inc., 2008, pp. 328-337.

[43] N. Marcuvitz, Waveguide Handbook, London: Peter Peregrinus Ltd., 1986.

[44] C. W. Chew, *Lectures on Theory of Microwave and Optical Waveguides*, Urbana-Champaign: University of Illinois, 2012.

[45] A. Wexler, "Solution of Waveguide Discontinuities by Modal Analysis," *IEEE Transactions on Microwave Theory and Techniques*, vol. 15, no. 9, pp. 508-517, 1967.

[46] R. Safavi-Naini and R. H. Macphie, "Scattering at Rectangular-to-Rectangular Waveguide Junctions," *Scattering at Rectangular-to-Rectangular Waveguide Junctions*, vol. 30, no. 11, pp. 2060-2063, 1982.

[47] V. Krichevsky and D. F. DiFonzo, "Diffraction of the TE10 Mode by a Symmetrical H-Step Discontinuity in a Rectangular Waveguide," in *12th European Microwave Conference*, Helsinki, Finland, 1982.

[48] A. Alvarez Melcon and M. Guglielmi, "Multimode Network Representation of Two Dimensional Steps in Rectangular Waveguides," in *24th European Microwave Conference*, Cannes, France, 1994.

[49] M. Guglielmi and C. Newport, "Rigorous, multimode equivalent network representation of inductive discontinuities," *IEEE Transactions on Microwave Theory and Techniques,* vol. 38, no. 11, pp. 1651-1659, 1990.

[50] M. Guglielmi and G. Gheri, "Rigorous multimode network representation of capacitive steps," *IEEE Transactions on Microwave Theory and Techniques,* vol. 42, no. 4, pp. 622-628, 1994.

[51] M. Guglielmi, G. Gheri, M. Calamia and G. Pelosi, "Rigorous multimode network numerical representation of inductive step," *IEEE Transactions on Microwave Theory and Techniques,* vol. 42, no. 2, pp. 317-326, 1994.

[52] H. E. Rowe and W. D. Warters, "Transmission in multimode waveguide with random imperfections," *The Bell System Technical Journal,* vol. 41, no. 3, pp. 1031-1170, 1962.

[53] T. E. Rozzi, "Network Modelling of Interacting Capacitive Irises and Steps in Waveguide," in *1975,* Palo Alton, CA, USA, IEEE-MTT-S International Microwave Symposium.

[54] Y. C. Shih and K. G. Gray, "Convergence of Numerical Solutions of Step-Type Waveguide Discontinuity Problems by Modal Analysis," in *IEEE MTT-S International Microwave Symposium Digest,* Boston, MA, USA, 1983.

[55] J. Kulinski, J. Gorzkowski and D. Bednarczyk, "Comparison of designing methods concerning E-plane rectangular waveguide step transformers," in *12th International Conference on Microwaves and Radar. MIKON-98. Conference Proceedings (IEEE Cat. No.98EX195),* Krakow, Poland, 1998.

[56] M. Mongiardo, P. Russer, M. Dionigi and L. B. Felsen, "Waveguide step discontinuities revisited by the generalized network formulation," in *1998 IEEE MTT-S International Microwave Symposium Digest*, Baltimore, MD, USA, 1998.

[57] F. C. de Ronde, M. Mongiardo and T. Rozzi, "Full band matching of E-plane steps in rectangular waveguide," in *21st European Microwave Conference,* Stuttgart, Germany, 1991.

[58] H. Jui-Pang, T. Hiraoka and H. Honma, "Equivalent network for rectangular-waveguide H-plane step discontinuity-multi-transmission line and multi-port ideal transformer," in *IEEE MTT-S International Microwave Symposium Digest*, Boston, MA, USA, 2000.

[59] H. Patzelt and F. Arndt, "Double-Plane Steps in Rectangular Waveguides and Their Application for Transformers, Irises, and Filters," *IEEE Transactions on Microwave Theory and Techniques,* vol. 30, no. 5, pp. 771-776, 1982.

[60] W. Williams, "Step discontinuities in waveguides," *IRE Transactions on Antennas and Propagation,* vol. 5, no. 2, pp. 191-198, 1957.

[61] A. Weisshaar, M. Mongiardo, A. Tripathi and V. K. Tripathi, "CAD-oriented equivalent circuit models for rigorous full-wave analysis and design of waveguide components and circuits," in *IEEE MTT-S International Microwave Symposium Digest*, San Francisco, CA, USA, 1996.

[62] T. Rozzi and M. Mongiardo, "E-plane steps in rectangular waveguide," *IEEE Transactions on Microwave Theory and Techniques,* vol. 39, no. 8, pp. 1279-1288, 1991.

[63] P. J. B. Clarricoats and K. R. Slinn, "Numerical solution of waveguide-discontinuity problems," *Proceedings of the Institution of Electrical Engineers,* vol. 114, no. 7, pp. 878-886, 1967.

[64] C. Changyul, C. Kyung, J. Hyun-Kyo and H. Song-Yop, "Analysis of waveguide discontinuities in H-plane using finite element-boundary element technique," *IEEE Transactions on Magnetics,* vol. 30, no. 5, pp. 3168-3171, 1994.

[65] M. Mongiardo and T. Rozzi, "Efficient CAD of E-plane steps in rectangular waveguide," in *IEEE International Digest on Microwave Symposium*, Dallas, TX, USA, 1990.

[66] A. Weisshaar, M. Mongiardo and V. K. Tripathi, "CAD-oriented equivalent circuit modeling of step discontinuities in rectangular waveguides," *IEEE Microwave and Guided Wave Letters,* vol. 6, no. 4, pp. 171-173, 1996.

[67] T. Ul Haq, K. J. Webb and N. C. Gallagher, "Compact Circular Wavewguide Mode Converters," *Microwave and Optical Technology Letters,* vol. 13, no. 5, pp. 251-255, 1996.

[68] T. Ul Haq, K. J. Webb and N. C. Gallagher, "Optimized Irregular Structures for Spatial- and Temporal-Field Transformation," *IEEE TRANSACTIONS ON MICROWAVE THEORY AND TECHNIQUES,* vol. 46, no. 11, pp. 1856-1866, 1998.

[69] Y. Ming-Chuan, L. Jia-Han and K. J. Webb, "Functional waveguide mode transformers," *IEEE Transactions on Microwave Theory and Techniques,* vol. 52, no. 1, pp. 161-169, 2004.

[70] M. Yang and K. J. Webb, "Synthesis of irregular waveguide field transformation elements using a multi-resolution algorithm," in *IEEE Antennas and Propagation Society International Symposium*, San Antonio, TX, USA, 2002.

[71] J. P. Quine, "E- and H-Plane Bends for High-Power Oversized Rectangular Waveguide," *IEEE Transactions on Microwave Theory and Techniques,* vol. 13, no. 1, pp. 54-63, 1965.

[72] J. P. Quine, "E and H-Plane Bends for High-Power Oversized Rectangular Waveguide," in *PTGMTT International Symposium Digest*, Long Island, NY, USA, 1964.

[73] B. Gimeno and M. Guglielmi, "Multimode network representation for H- and E-plane uniform bends in rectangular waveguide," in *IEEE MTT-S International Microwave Symposium*, Orlando, FL, USA, 1995.

[74] B. Gimeno and M. Guglielmi, "Multimode equivalent network representation for H- and E-plane uniform bends in rectangular waveguide," *IEEE Transactions on Microwave Theory and Techniques,* vol. 44, no. 10, pp. 1679-1687, 1996.

[75] E. Bahar, "Fields in Waveguide Bends Expressed in Terms of Coupled Local Annular Waveguide Modes," *IEEE Transactions on Microwave Theory and Techniques,* vol. 17, no. 4, pp. 210-217, 1969.

[76] E. Bahar and G. Govindarajan, "Rectangular and Annular Modal Analyses of Multimode Waveguide Bends," *IEEE Transactions on Microwave Theory and Techniques,* Vols. MTT-21, no. 12, pp. 819-824, 1973.

[77] S. O. Rice, "Reflections from circular bends in rectangular wave guides — Matrix theory," *The Bell System Technical Journal,* vol. 27, no. 2, pp. 305-349, 1948.

[78] P. L. Carle, "New accurate and simple equivalent circuit for circular E-plane bends in rectangular waveguide," *Electronics Letters,* vol. 23, no. 10, pp. 531-532, 1987.

[79] J. A. P. R. G. Cochran, "Mode propagation in continuously curved waveguides," *Radio Science,* vol. 1, no. 6, pp. 679-696, 1966.

[80] C. P. Bates, "Intermodal Coupling at the Junction Between a Straight and a Continuously Curved Waveguide of Rectangular Cross Section," in *1969 G-MTT International Microwave Symposium*, Dallas TX, USA, 1969.

[81] L. Accatino and G. Bertin, "Modal Analysis of Curved Waveguides," in *20th European Microwave Conference*, Budapest, Hungary, 1990.

[82] A. Weisshaar, S. M. Goodnick and V. K. Tripathi, "A rigorous and efficient method of moments solution for curved waveguide bends," *IEEE Transactions on Microwave Theory and Techniques,* vol. 40, no. 12, pp. 2200-2206, 1992.

[83] A. A. S. Blas, B. Gimeno, V. E. Boria, H. Esteban, S. Cogollos and A. Coves, "A rigorous and efficient full-wave analysis of uniform bends in rectangular waveguide under arbitrary incidence," *IEEE Transactions on Microwave Theory and Techniques,* vol. 51, no. 2, pp. 397-405, 2003.

[84] A. Weisshaar, S. M. Goodnick and V. K. Tripathi, "A rigorous method of moments solution for curved waveguide bends and its applications," in *IEEE MTT-S Microwave Symposium Digest,* Albuquerque, NM, USA, 1992.

[85] Z. Qiang, Y. Cheng-Wei and L. Lie, "Theoretical Design and Analysis for TE20-TE10 Rectangular Waveguide Mode Converters," *IEEE Transactions on Microwave Theory and Techniques,* vol. 60, no. 4, pp. 1018-1026, 2012.

[86] S. Matsumoto, I. Ohta, K. Fukada, T. Kawai, K. Iio and T. Kashiwa, "A TE10-TE20 mode transducer utilizing a right-angled corner and its application to a compact H-plane out-of-phase power divider," in *2009 Asia Pacific Microwave Conference*, Singapore, 2009.

[87] H. Ikeuchi, T. Kawai, M. Kishihara and I. Ohta, "Design of TE10-TE30 mode transducer using H-plane waveguide corner," in *Asia-Pacific Microwave Conference 2011*, Melbourne, VIC, USA, 2011.

[88] S. Matsumoto, M. Ohshima, K. Fukata, T. Kawai, I. Ohta, M. Kishihara, K. Iio and T. Kashiwa, "Compact H-plane waveguide corners with very wide bandwidth," in *2008 IEEE MTT-S International Microwave Symposium Digest*, Atlanta, GA, USA, 2008.

[89] K. C. Kao, "Approximate solution of the H plane right-angled corner in overmoded rectangular waveguide, operating in the H10 mode," *Proceedings of the Institution of Electrical Engineers,* vol. 111, no. 4, pp. 624-628, 1964.

[90] A. A. Kirilenko, L. A. Rud and V. I. Tkachenko, "Nonsymmetrical H-plane corners for TE10-TEq0 mode conversion in rectangular waveguides," *IEEE Transactions on Microwave Theory and Techniques,* vol. 54, no. 6, pp. 2471-2477, 2006.

[91] L. B. Felsen and C. L. Ren, "Scattering by obstacles in a multimode waveguide," *Proceedings of the Institution of Electrical Engineers,* vol. 113, no. 1, pp. 16-26, 1966.

[92] G. E. Crain, "Symmetries of the overmoded right-angle corner," *Proceedings of the Institution of Electrical Engineers,* vol. 117, no. 4, pp. 713-717, 1970.

[93] G. E. Crain and L. Lewin, "Theoretical performance of the overmoded right-angle corner," *Proceedings of the Institution of Electrical Engineers,* vol. 116, no. 5, pp. 667-678, 1969.

[94] S. Khan, N. Vahabisani and M. Daneshmand, "A Fully 3-D Printed Waveguide and Its Application as Microfluidically Controlled Waveguide Switch," *IEEE TRANSACTIONS ON COMPONENTS, PACKAGING AND MANUFACTURING TECHNOLOGY,* vol. 7, no. 1, pp. 70-80, 2017.

[95] "Zortrax M200," Zortrax, [Online]. Available: https://zortrax.com/printers/zortrax-m200/. [Accessed 27 11 2017].

[96] CST, "CST Studio Suite Brochure," 2017. [Online]. Available: https://www.cst.com/-/media/cst/solutions/articles/flyer/cst-studio-suite-brochure/attachments/cst-studio-suite-2017.ashx.

[97] CST, "CST Microwave Studio- Transient solver," CST, [Online]. Available: https://www.cst.com/products/cstmws/solvers/transientsolver. [Accessed 8 November 2017].

[98] T. Weiland, "A discretization method for the solution of Maxwell's erquations for six-component fields," *Electronics and Communication (AEÜ),* vol. 31, pp. 116-120, 1977.

[99] T. Weiland, "Time domain electromagnetic filed computation with finite difference methods," *International Journal of Numerical Modelling,* vol. 9, pp. 295-319, 1996.

[100] B. Krientenstein, R. Schuhmann, P. Thoma and P. Weiland, "The Perfect Boundary Approximation technique facing the challenge of high precision field computation," in *19th International Linear Accelerator Conference*, Chicago, 1998.

[101] T. Weiland, "RF & microwave simulators - from component to system design," in *33rd European Microwave Conference*, Munich, Germany, 2003.

[102] CST, "Frequency Domain Solver Overview," CST, 2017.

[103] CST, "CST MICROWAVE STUDIO® - Frequency Domain Solver," CST, [Online]. Available: https://www.cst.com/products/cstmws/solvers/frequencydomainsolver. [Accessed 8 November 2017].

[104] CST, "Eigenmode Solver Overview," CST, 2017.

[105] CST, "CST MICROWAVE STUDIO® - Eigenmode Solver," CST, [Online]. Available: https://www.cst.com/products/cstmws/solvers/eigenmodesolver. [Accessed 8 November 2017].

[106] CST, "CST MICROWAVE STUDIO® - Integral Equation Solver (MLFMM)," CST, [Online]. Available:

https://www.cst.com/products/cstmws/solvers/integralequationsolver. [Accessed 8 November 2017].

[107] CST, "Integral Equation Solver Overview," CST, 2017.

[108] CST, "Multi Level Fast Multipole Method," CST, 2017.

[109] CST, "Multilayer Solver Overview," CST, 2017.

[110] CST, "Asymptotic Solver Overview," CST, 2017.

[111] V. Sokol, "Optimization Techniques in CST STUDIO SUITE," 2011. [Online]. Available: https://www.cst.com/Content/Events/Downloads/eugm2011/Talk_6-1-4_CST_UGM_2011.pdf. [Accessed 8 November 2017].

[112] CST, "Optimizer - Settings," CST, 2017.

[113] CST, "Optimizer - Algorithm Settings," CST, 2017.

[114] CST, "Local Optimizers," CST, [Online]. Available: https://www.cst.com/products/csts2/optimization/local-optimizer. [Accessed 8 November 2017].

[115] CST, "Global Optimizers," CST, [Online]. Available: https://www.cst.com/products/csts2/optimization/global-optimizer. [Accessed 8 November 2017].